Commissioning of the ATLAS pixel detector and search of the Higgs boson in the ttH, H -> bb channel with the ATLAS experiment at the LHC.

G. Aad

HAL Id: tel-00435525
https://theses.hal.science/tel-00435525

Submitted on 24 Nov 2009

UNIVERSITÉ DE LA MÉDITERRANÉE
AIX-MARSEILLE II

FACULTÉ DES SCIENCES DE LUMINY

163 avenue de Luminy

13288 MARSEILLE Cedex 09

THÈSE DE DOCTORAT

Spécialité : _Physique et Sciences de la Matière_

Mention : _Physique des Particules et Astroparticules_

présentée par

Georges AAD

en vue d'obtenir le grade de docteur de l'Université de la Méditerranée

Mise en service du détecteur à pixels de l'expérience ATLAS auprès du LHC et étude du canal $t\bar{t}H$, $H \to b\bar{b}$ pour la recherche du boson de Higgs

soutenue le 18 septembre 2009 devant le jury composé de

Dr.	K. Einsweiler	Rapporteur
Dr.	L. Fayard	Rapporteur
Dr.	E. Kajfasz	
Dr.	A. Rozanov	Directeur de thèse
Prof.	M. Talby	
Dr.	L. Vacavant	Co-Directeur de thèse
Prof.	N. Wermes	

Remerciements

Je tiens tout d'abord à remercier les membres du jury :
– Kevin et Louis pour avoir accepté d'être mes rapporteurs ainsi que pour leur soutien concernant les pixels et le ttH respectivement.
– Sasha qui m'a permis d'effectuer cette thèse sous sa direction et pour son aide pendant ces trois ans.
– Éric, le directeur du CPPM, et Mossadek, le directeur du groupe ATLAS CPPM, pour leur soutien tout au long de ces trois années de thèse ainsi que pendant l'année du master.
– Norbert pour avoir accepté d'être un membre du jury et pour sa grande gentillesse durant les quelques discussions que nous avons eues la chance d'avoir.
– Et finalement Laurent pour le suivi de la thèse de plus près, pour les millions de questions que je lui ai posées, pour le temps précieux qu'il m'a accordé et surtout pour avoir supporté mon tempérament un peu difficile tout au long de la thèse. Laurent je suis vraiment reconnaissant pour tout ce que tu as fait pour moi.

Je remercie Lorenzo pour m'avoir accompagné pour l'étude ttH et toute l'aide qu'il m'a apportée concernant ce travail.
Je remercie Rémi pour l'aide et les discussions utiles pendant la thèse et les nombreuses années d'étude que nous avons effectuées ensemble.
Je remercie Cécile pour les nombreux services au niveau professionnel mais surtout au niveau personnel.

Je remercie le groupe de thésards avec qui j'ai passé le plus de temps au CPPM, Garo et Stéphane, et les nouveaux membres Sahar, Nancy, et Nicolas ainsi que tous les autres thésards du CPPM. C'était vraiment un plaisir de passer trois ans avec vous.
Je remercie Fares, Fabrice, Steve, Pierre-Simon, Marine, Huaqiao, Jérôme et tous les membres du groupe ATLAS CPPM ainsi que les visiteurs (Gordon et Joe).
Je remercie les physiciens du CPPM en général ainsi que les membres du support

Contents

Introduction

Le Modèle Standard de la physique des particules, fondé pendant la seconde moitié du vingtième siècle, décrit avec une très grande précision toutes les particules connues et leurs interactions. Ce modèle a permis de prédire un large nombre de particules qui ont été découvertes grâce à différentes expériences durant les 40 dernières années. Le boson de Higgs est la seule particule prédite par le Modèle Standard qui n'a jamais été observée.

Malgré son grand succès, le Modèle Standard ne peut pas répondre à de nombreuses questions à la fois théoriques et expérimentales. On suppose qu'une nouvelle physique, avec de nouveaux phénomènes et de nouvelles particules, doit exister. On ne sait pas exactement à quelle echelle d'énergie elle doit apparaître mais plusieurs arguments privilégient l'échelle du TeV.

Un nouvelle ère de physique s'approche avec les données du LHC. Le LHC doit pouvoir éclaircir un grand nombre de questions actuellement sans réponses. Le LHC va chercher la nouvelle physique dans un domaine d'énergie allant jusqu'au TeV. L'un des buts principaux du LHC est de comprendre l'origine de la brisure de symétrie électrofaible et l'origine des masses des particules. Le LHC doit permettre de déterminer si le mécanisme de Higgs est le mécanisme responsable des origines des masses et si le boson de Higgs existe. Plusieurs expériences cherchent, ou ont cherché, le boson de Higgs sans succès jusqu'à présent. En revanche plusieurs limites, à la fois des limites directe ou indirecte, sur la masse du boson de Higgs ont été extraites. Les limites indirectes, ainsi que différents arguments théoriques, privilégient un boson de Higgs de faible masse proche de la limite inférieure de 114.4 GeV établie par le LEP.

ATLAS est l'une des expériences qui va analyser les données produites au LHC et en particulier rechercher le boson de Higgs. Les différents canaux de production et de désintégration du boson de Higgs ont guidé la conception du détecteur ATLAS. ATLAS doit permettre de découvrir le boson de Higgs du Modèle Standard après quelques années de fonctionnement du LHC. Cependant une découverte du boson de Higgs de faible masse ($m_H <$ 135 GeV) est difficile au LHC. La combinaison de plusieurs canaux est nécessaire pour accélérer la découverte. L'un des canaux considérés est le canal $t\bar{t}H(H \to b\bar{b})$ où le boson de

Higgs est produit en association avec une paire de quarks top et se désintègre en une paire de quarks b.

L'un des plus importants ingrédients pour le canal $t\bar{t}H(H \to b\bar{b})$ est l'identification des jets qui proviennent de l'hadronisation des quarks b. Cette identification nécessite une bonne reconstruction des traces et des vertex dans le détecteur interne d'ATLAS. Ainsi des mesures de grande précision sont indispensables dans la région proche du point de collision au LHC. Les détecteurs à pixels présentent la seule technologie capable d'assurer des mesures aussi précises dans l'environnement dense en radiation du LHC.

Les deux sujets principaux traités dans cette thèse sont la mise en service du détecteur à pixels d'ATLAS et l'étude du canal $t\bar{t}H(H \to b\bar{b})$ avec l'expérience ATLAS. Le chapitre 1 présente brièvement le Modèle Standard de la physique des particules ainsi que nos connaissances actuelles du boson de Higgs. Le LHC et le détecteur ATLAS sont présentés dans le chapitre 2. Le chapitre 3 décrit le détecteur à pixels d'ATLAS. Deux des propriétés du détecteur à pixels, à savoir le faible bruit et la grande efficacité, sont étudiés en details. Le chapitre 4 présente une analyse détaillée du canal $t\bar{t}H(H \to b\bar{b})$. Cette analyse comporte une mise à jour de celle déjà presentée dans le "CSC book" d'ATLAS[1].

Introduction

The Standard Model of particle physics, established in the second half of the twentieth century, is very successful in describing known particles and their interactions with an astonishing precision. This model predicted successfully a large number of new particles that were all discovered throughout different experiments in the last 40 years. Only one particle, predicted by this model, is still undiscovered: the Higgs boson.

Despite its great successes, the Standard Model does not provide answers for several questions that arise both from theoretical arguments and experimental observations. It is thought that new physics should exist leading to new particles and phenomena. The scale at which this new physics should appear is not clear, though several arguments point to the TeV scale.

Now that the Large Hadron Collider (LHC) is close to deliver data, a new era of particle physics is approaching. The LHC is expected to shed some light on a large number of unresolved questions. The LHC will scan an energy domain up to the TeV scale, searching for new physics. Understanding the origin of the electroweak symmetry breaking, and the origin of particle masses, is one of the most important goals of the LHC. The LHC should provide an answer about the Higgs mechanism being the responsible of the electroweak symmetry breaking and the presence of the Higgs particle. Several experiments searched or are searching for the Higgs boson without any successful discovery. However several direct and indirect limits on the Higgs boson mass can be extracted. Both theoretical arguments and experimental indirect limits, from the electroweak data, point towards a light Higgs boson with a mass close to the lower limit at 114.4 GeV set at the LEP experiments.

ATLAS is one of the experiments that will collect and analyse the LHC data and search for the Higgs boson. Different production and decay modes of the Higgs boson were taken as a benchmark channels driving the general design and specifications of the ATLAS detector. ATLAS will be able to discover a Standard Model Higgs boson in the first few years after the LHC startup, though discovering a light Higgs boson ($m_H < 135$ GeV) is difficult at the LHC. Several production and decay modes will have to be combined to allow the earliest possible discovery.

3

One of these channels may be the $t\bar{t}H(H \to b\bar{b})$ channel where the Higgs boson is produced in association with a top quark pair and decays into two *b*-quarks.

One of the most important ingredients for the $t\bar{t}H(H \to b\bar{b})$ channel is the identification of jets coming from the hadronisation of *b*-quarks. This identification relies on the tracking and vertexing capabilities of the ATLAS inner tracker. High-precision measurements are needed next to the proton-proton collision point to be able to efficiently tag jets. Pixel detectors are the only technology that is capable of providing such a measurements in the very harsh environment at the LHC.

The main topics of this thesis are the commissioning of the ATLAS pixel detector and the study of the $t\bar{t}H(H \to b\bar{b})$ channel with the ATLAS experiment. We begin with a general overview of the Standard Model in Chapter 1. The current knowledge about the Higgs boson is also presented. Chapter 2 is devoted to a general overview of the LHC and the ATLAS detector. In chapter 3, the ATLAS pixel detector is described. Two of the most exciting properties of the pixel detector, the low noise occupancy and the high detection efficiency, are studied in details. In chapter 4, a detailed analysis concerning the observability of the $t\bar{t}H(H \to b\bar{b})$ channel is presented. This analysis is an update of the one presented in the ATLAS CSC book[1].

Chapter 1

The Standard Model of particle physics

At the beginning of the 20th century, a breakthrough was accomplished in fundamental physics. The General Relativity and the Quantum Mechanics suggested new visions of our physical world. After establishing the Quantum Mechanics, several developments, both theoretical and experimental, lead to the Standard Model (SM) of particle physics as it is known nowadays. This model gathers several pieces developed during the last 50 years: the Dirac [2] relativistic quantum equation and the prediction of anti-particles, the Fermi [3] theory of weak interactions, the Gross, Wilczek, Politzer [4, 5, 6] Quantum chromodynamics (QCD) with the asymptotic freedom, the Gell-Mann, Zweig and Nambu [7, 8, 9] coloured quark model and last but not least the Glashow, Weinberg and Salam [10, 11, 12] electroweak theory including the Higgs mechanism and the electroweak symmetry breaking.

The SM can explain, with very high precision, most of the experimental data collected using several experiments in the second half of the 20th century. This makes it a well established model. However one piece is still missing to complete the electroweak sector of the SM: the Higgs boson. The Higgs boson discovery will totally diminish any doubts about the Higgs mechanism being the origin of the electroweak symmetry breaking. Some other problems, mostly theoretical ones, make physicists think about the SM as an effective model of a more fundamental theory. These problems will be discussed briefly at the end of this chapter.

We will begin by an overview of the elementary particles and their interactions in section 1.1. Then we will discuss briefly the SM mathematical foundation focusing on the electroweak sector in section 1.2. In section 1.3 the electroweak symmetry breaking and the Higgs mechanism will be discussed. An overview of the theoretical knowledge along with the experimental limits on the Higgs boson mass is presented in section 1.5.

1.1 The elementary particles and their interactions

The SM describes all known elementary particles and three of the four fundamental interactions: the electromagnetic, strong and weak interactions. The gravitational interaction, described by the General Relativity which is not a quantum theory, is not included in the SM. The elementary particles can be divided into two categories according to their spin:

- half-integer spin particles, the fermions: they obey to the Fermi-Dirac statistics. Ordinary matter is formed of light fermions;

- integer spin particles, the bosons: these particles obey to the Bose-Einstein statistics. SM fundamental interactions are described in terms of boson exchanges between fermions.

Family	Particle	L	B	Charge	Mass
1st	e	1	0	-1	511 keV
	ν_e	1	0	0	< 2 eV
2nd	μ	1	0	-1	105.66 MeV
	ν_μ	1	0	0	< 0.19 MeV
3rd	τ	1	0	-1	1.78 GeV
	ν_τ	1	0	0	< 18.2 MeV

Table 1.1: Lepton classification showing the lepton (L) and baryon (B) numbers, the electric charge and the particle mass.

Family	Particle	L	B	Charge	Mass
1st	u	0	1/3	2/3	1.5 - 3.3 MeV
	d	0	1/3	-1/3	3.5 - 6 MeV
2nd	c	0	1/3	2/3	1.27 GeV
	s	0	1/3	-1/3	104 MeV
3rd	t	0	1/3	2/3	171.2 GeV
	b	0	1/3	-1/3	4.2 GeV

Table 1.2: Quark classification showing the lepton (L) and baryon (B) numbers, the electric charge and the particle mass.

1.1.1 The fermions

We can divide fermions into two categories and three families. The first category contains particles that do not interact strongly. These particles are called leptons.

They hold a leptonic number $L = 1$. The second category contains coloured particles that interact strongly. These particles are called quarks. The quarks hold a baryonic number $B = 1/3$. Within the SM, the number B-L should be conserved. The B and L numbers could eventually be not conserved in some cases, e.g. in chiral anomalies, but this has not been detected experimentally.

Both leptons and quarks are divided into three families. The first family contains the electron and its associated neutrino, and the up and down quarks. The two other families are replicas of the first family, their particles having different mass and flavor. For the leptons, the two other flavors are the muon and tau leptons and their corresponding neutrinos. The charm and top quarks are the equivalent of the up quark for the 2nd and 3rd generation, while the strange and the bottom quarks correspond to the down quark. To each of these particles corresponds an anti-particle with the same mass and spin but with opposite charges (electric charge, colour etc.). Table 1.1 and 1.2 summarise the SM fermions and some of their properties.

1.1.2   The bosons and the fundamental interactions

The bosons are responsible of the SM interactions. We can distinguish three kinds of bosons:

- the photon (γ): this is the well known light's particle. It is the mediator of the electromagnetic interaction. The photon is massless and stable therefore the electromagnetic interaction has an infinite range. The photon can interact with all the particles carrying an electric charge;

- the $W^{\pm}$ and Z bosons: these are the mediators of the weak interaction between particles of different flavors. The range of the weak force is finite since the W and Z bosons have a mass and a finite lifetime. They couple to all particles which carry a weak isospin charge;

- the gluons: there are 8 gluons differing by their colour charge. These particles are the mediators of the strong interaction. One of the most important properties of QCD is the confinement [13] which forbids the presence of free coloured particles. Therefore the gluons have a small lifetime as free states, although they are massless, and the range of the strong interaction is finite. The gluons can interact with all coloured particles.

Table 1.3 summarises the fundamental interactions along with the corresponding bosons and some of their properties. The gravitational interaction is 34 orders of magnitude weaker than the weak interaction and can be totally neglected in the range of energies relevant for particle physics.

Interaction →	Strong	Electromagnetic	Weak	Gravitational
Corresponding charge	colour	electric charge	weak isospin	energy
Mediators bosons	gluons	photon	$W^\pm$, Z	graviton?
Range [m]	10^{-15}	∞	10^{-18}	∞
Relative force	1	10^{-2}	10^{-6}	10^{-40}

Table 1.3: Fundamental interactions and some of their properties. The gravitational interaction is not described by the SM but it is added for completeness.

1.2 The Standard Model formalism

To build the SM, the Lagrangian formalism is the most convenient. We consider a general action of the form:

$$S = \int dV \, \mathscr{L}(\partial_\mu \Psi, \partial_\mu \overline{\Psi}, \Psi, \overline{\Psi})$$

where Ψ is the field describing fermions. The choice of the Lagrangian is constrained by the different symmetries that can be found in Nature. As a starting point, the Lagrangian is invariant under Poincaré transformations. This insures that the laws of the Universe are similar considering different space-time points. This also leads to the energy, momentum and angular momentum conservation laws.

Additional symmetry groups are derived by looking at the particle interactions. A rotation, involving particles (fields) with a similar behaviour regarding a given interaction, should not change the physics laws and thus should leave the Lagrangian invariant, e.g. a rotation of the colour charge corresponding to the $SU(3)_c$ symmetry group should not affect the Lagrangian of the strong interaction. Following Noether's theorem, the "interaction" symmetry leads to the conservation of the corresponding charge.

1.2.1 Chiral Yang-Mills theory

The SM is a chiral Yang-Mills theory based on the group of symmetry $SU(2)_L \times U(1)_Y \times SU(3)_c$. In a Yang-Mills theory, the Lagrangian is invariant under the symmetry group independently in each space-time point. This is the so-called local gauge symmetry. This symmetry provides an accurate description of the physical interactions.

The Dirac action for massless particles can be written as follows:

$$S_{Dirac}[\Psi, \overline{\Psi}] = \int dV \, \overline{\Psi} \slashed{\partial} \Psi \text{ where } \slashed{\partial} = i\gamma^\mu \partial_\mu \text{ and } \overline{\Psi} = \Psi^\dagger \gamma^0$$

To insure the gauge symmetry, one should replace the normal derivative,$\not{\partial}$, by the covariant derivative, $\not{D} = i\gamma^\mu(\partial_\mu + A_\mu)$. A_μ is a member of a base in the Lie algebra of the corresponding symmetry group and will represent the bosonic fields. The group $SU(2)_L \times U(1)_Y$, of dimension four, will generate the $W_{1,2,3}$ and the B bosons. With an appropriate change of base, these bosons will mix to give the physical $W^\pm$, Z bosons and the photon. The group $SU(3)_c$ is the generator of the 8 gluons.

A group is an abstract object following some mathematical rules. One needs to find a concrete mathematical object, describing the group, to be able to do useful calculation for physics. This is called the representation of the group. The choice of the representation is mandatory as it will dictates the interaction form, as explained in what follows. The actual representation of A_μ will be noted $\tilde\rho(A_\mu)$ and thus the Dirac action can be rewritten as:

$$S_{Dirac}[\Psi, A] = \int dV\, \overline\Psi(i\gamma^\mu(\partial_\mu + \tilde\rho(A_\mu)))\Psi$$

Ψ represents the fermionic fields that are elements of the following Hilbert space: $\mathcal{H}_P \otimes \mathcal{H}_I$. $\mathcal{H}_I$ is a space of representation of the interaction symmetry group. $\mathcal{H}_P$ is a space of representation of the Poincaré group, e.g. the spinorial representation. The spinorial representation was introduced by Dirac to represent the fermions. The spinor four components can be viewed as the two spins of each of the fermions and their corresponding anti-fermions. This representation can be divided into two irreducible representations of dimension two: $\mathcal{H}_P = \mathcal{H}_L \oplus \mathcal{H}_R$. In this representation, a particle has two components of respectively left and right chirality. This representation is introduced to account for the observed parity violation in the weak interactions.

The covariant derivative, $\not{D}$, introduces an interaction term ($\overline\Psi\tilde\rho(A_\mu)\Psi$) between bosons and fermions, to the Lagrangian. The choice of the representation dictates the action of the boson operator on the fermions and therefore dictates the interaction form. As an example the left-handed fermions are represented as doublets in the representation space of the SU(2) group. The defining representation is chosen and the weak bosons operators, in the corresponding Lie algebra, su(2)[1], will be 2×2 matrices. The right-handed fermions are SU(2) singlets, therefore only a representation of dimension one is needed. The trace of the matrix is chosen to represent the weak boson. Since the trace of su(2) matrices is zero the right-handed fermions do not interact weakly. The weak charge or the weak isospin is defined as the eigen value of the third generator I_3 of the su(2) algebra. For the

---

[1]We will use the notation SU(n), upper case, to refer to the symmetry group, and su(n), lower case to refer to the corresponding Lie algebra.

left-handed electron, $\tilde{\rho}(I_3)\Psi$ is proportional to:

$$\begin{pmatrix} \frac{1}{2} & 0 \\ 0 & -\frac{1}{2} \end{pmatrix} \begin{pmatrix} 0 \\ 1 \end{pmatrix} = -\frac{1}{2} \begin{pmatrix} 0 \\ 1 \end{pmatrix}$$

The same applies to the left-handed neutrino which has an isospin charge of $\frac{1}{2}$. For the right-handed electron the isospin is 0. In fact $\tilde{\rho}(I_3)\Psi \propto Tr(I_3) \times e_R = 0$.

1.2.2 The Standard Model case

After identifying the symmetry groups, one should choose the representations to build the SM. The choice of the representation is not dictated by first principles, but is constrained by experimental data. The representations used in the SM are listed in table 1.4. They are listed as (I,Y,C) triplets were "I" represents the dimension of the weak interaction space (doublet or singlet), "Y" represents the hypercharge, and "C" represents the space dimension of the strong interaction (singlet or triplet). The 3rd component of the su(2) algebra generator and the u(1) generator mix to give the photon and the Z boson. Therefore the electric charge is related to the weak isospin and the hypercharge by the Gell-Mann-Nishijima formula: $Q = I + \frac{Y}{2}$.

For lepton interactions with gluons, one can choose the singlet representation. The su(3) algebra generators are defined by the su(3) matrices traces. Since the trace of su(3) matrices are null, the leptons do not have a colour charge and do not interact strongly. The quarks are SU(3) triplets, they hold one of the three colour charges and thus can interact strongly. The left leptons are SU(2) doublets and interact weakly. The right leptons are SU(2) singlets and do not interact with the W bosons. The hypercharge dictates the electric charge and therefore the interaction with photons.

All three families have the same representation spaces: their particles all interact in the same way with bosons.

In addition to the "Dirac-like terms" that describe the fermions, the SM Lagrangian has additional terms describing the kinematics and the interactions of bosons. These terms are a generalisation of the Maxwell Lagrangian describing the photons:

$$\mathcal{L}_M = -\frac{1}{4} F^{\mu\nu} F_{\mu\nu}$$

$F_{\mu\nu}$ is the field strength given by $\partial_\mu A_\nu - \partial_\nu A_\mu - i[A_\mu, A_\nu]$. This implies the presence of terms of the form AAA and $AAAA$ respectively for the three and four boson interactions. As for fermions, the interaction of bosons among themselves is dictated by the choice of the representation of the corresponding group. For

Particles	Representation	Electric charge	Colour	Weak isospin
Fermions				
Left-handed leptons	$(2,-1,1)$	$0,-1$	no	$\pm\frac{1}{2}$
Right-handed leptons	$(1,-2,1)$	-1	no	0
Left-handed quarks	$(2,\frac{1}{3},3)$	$\frac{2}{3},-\frac{1}{3}$	yes	$\pm\frac{1}{2}$
Right-handed quarks (u)	$(1,\frac{4}{3},3)$	$\frac{2}{3}$	yes	0
Right-handed quarks (d)	$(1,-\frac{2}{3},3)$	$-\frac{1}{3}$	yes	0
Bosons				
B	$(1,0,1)$	0	no	0
W^i	$(3,0,1)$	$\pm 1,0$	no	$\pm 1,0$
gluons	$(1,0,8)$	0	yes	0

Table 1.4: Representations space for fermions and bosons in the SM. B is the generator of the U(1)$_Y$ group and W^i are the generators of the SU(2)$_L$ group.

all groups we choose the adjoint representation. Table 1.4 lists the representation space of the various bosons. The adjoint representation is equivalent to the commutator of the bosons that are members of the Lie algebra of the symmetry group. For Abelian groups, such as U(1), the commutator is always 0 and therefore the corresponding bosons, the photons, do not interact with each others. For non-Abelian group, such as $SU(2)_L$ and $SU(3)_c$, the commutator is not 0 and the bosons have a charge (respectively electric/weak and colour) and can interact with each other.

1.3   The Higgs boson

The Maxwell Lagrangian and its generalisation does not allow mass terms for bosons. In fact the gauge transformation of bosons fields A_μ can be written as:

$$A_\mu \to U A_\mu U^\dagger + i U \partial_\mu U^\dagger$$

where U is an element of the gauge symmetry group. Mass terms of the form $\frac{1}{2}A_\mu A^\nu$ are not invariant under this transformation. Furthermore, in a chiral Yang-Mills theory the left and right representation of the SU(2) group are not the same allowing the parity violation. Mass terms of the form:

$$m(\overline{\Psi}_L \Psi_R + \overline{\Psi}_R \Psi_L)$$

breaks the gauge symmetry as the left and right components does not transform the same way under SU(2), therefore they are not allowed in the Lagrangian.

P. Higgs, R. Brout, F. Englert [14, 15] and others [16] suggested in 1964 a spontaneous symmetry breaking mechanism which could lead to massive bosons in a non-Abelian Yang-Mills theory. This is the so-called Higgs mechanism, giving rise to a scalar particle, the Higgs boson. The fermionic masses are generated by adding ad-hoc interaction terms of the fermions with this Higgs field.

(a) $\mu^2 > 0$ (b) $\mu^2 < 0$
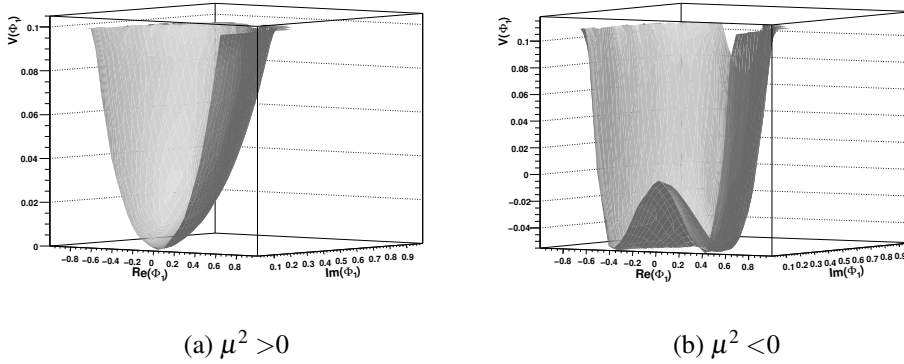
Figure 1.1: Higgs potential in case of $\mu^2 > 0$ (a) and $\mu^2 < 0$ (b). When choosing a negative value for μ^2 the minimum is defined in a circle. Nature chooses a point on that circle to define the vacuum which breaks the symmetry.

1.3.1 The Higgs mechanism

The Higgs mechanism was included in the electroweak theory by Weinberg and Salam to generate masses to the W and Z bosons. This can be done by adding a scalar complex field that is a SU(2) doublet:

$$\Phi = \begin{pmatrix} \phi_1 + i\phi_3 \\ \phi_2 + i\phi_4 \end{pmatrix}$$

were ϕ_i are real fields. This field is named the Higgs doublet. The Lagrangian of this field is given by:

$$\mathcal{L}_{Higgs} = (D^\mu \Phi)^\dagger D_\mu \Phi - \mu^2 \Phi^\dagger \Phi - \lambda (\Phi^\dagger \Phi)^2$$

where μ and λ are two free parameters and D_μ is the covariant derivative insuring the gauge symmetry of the group $SU(2) \times U(1)$ and given by:

$$D_\mu = \partial_\mu + ig_2 W_\mu^a \frac{\sigma^a}{2} + ig_1 \frac{Y}{2} B_\mu$$

12

The potential of the Higgs field is given by:

$$V_{Higgs} = \mu^2 \Phi^\dagger \Phi + \lambda (\Phi^\dagger \Phi)^2$$

λ must be positive to insure a finite value for the potential minimum and thus the vacuum stability. If one chooses a negative value for μ^2, the Higgs potential have a degenerated minimum as shown in figure 1.1. The fact that Nature chooses one value for the vacuum breaks the gauge symmetry. However the symmetry still applies to the system dynamics. This procedure is called the spontaneous symmetry breaking. In the case of the electroweak spontaneous symmetry breaking, the vacuum is given by:

$$\Phi_{min} = \begin{pmatrix} 0 \\ \frac{v}{\sqrt{2}} \end{pmatrix}$$

where v is the vacuum expectation value, the vev. It is given by:

$$v = \langle 0|\Phi|0 \rangle = \sqrt{-\frac{\mu^2}{\lambda}}$$

The Higgs field vacuum is not symmetric under the SU(2) gauge transformation but is still symmetric under the U(1) gauge group. This allows to generate masses to the W and Z boson but not to the photon. In fact we can rewrite the Higgs field as a fluctuation added to the vacuum expectation value as following:

$$\Phi = e^{i\frac{\Theta^a(x)\sigma^a}{2v}} \begin{pmatrix} 0 \\ \frac{v+H(x)}{\sqrt{2}} \end{pmatrix}$$

where the σ^a are the three Pauli matrices and the Θ^a are the Goldstone bosons [17]. The SM Lagrangian is invariant under the SU(2) gauge transformation: one can apply to it the SU(2) transformation $e^{-i\frac{\Theta^a(x)\sigma^a}{2v}}$. Therefore the three Goldstone fields Θ^a are absorbed and one is left with one real field H(x). This can be seen as the W and Z bosons absorbing an extra degree of freedom corresponding to a longitudinal polarisation, and thus acquiring a mass. This can be achieved by simply applying the covariant derivative D_μ on the resulting Higgs fields. A change of variable is then needed to be able to correctly write the kinematic terms. This will correspond to a rotation of an angle θ_W, which mixes the B_μ boson, generator of the U(1) group, and the W^3_μ boson, third generator of the SU(2) group, and gives rise to the photon and the Z boson. Mass terms and interaction terms with the Higgs boson, for the W and the Z bosons, appear naturally in the Lagrangian:

$$D^\mu \begin{pmatrix} 0 \\ \frac{v}{\sqrt{2}} \end{pmatrix}^\dagger D_\mu \begin{pmatrix} 0 \\ \frac{v}{\sqrt{2}} \end{pmatrix} \longrightarrow \text{Mass terms}$$

$$D^\mu \begin{pmatrix} 0 \\ \frac{H(x)}{\sqrt{2}} \end{pmatrix}^\dagger D_\mu \begin{pmatrix} 0 \\ \frac{H(x)}{\sqrt{2}} \end{pmatrix} \longrightarrow \text{Interaction terms}$$

The resulting bosons masses are given by:

$$M_W = g_2 \frac{v}{2} \quad \text{and} \quad M_Z = g_2 \frac{v}{2\cos\theta_W} \qquad (1.1)$$

The H(x) field defines a new particle, the Higgs boson. The terms of the Higgs potential defines the Higgs boson mass and its self-interaction. The Higgs mass is given by:

$$M_H = \sqrt{-2\mu^2} = v\sqrt{2\lambda}. \qquad (1.2)$$

1.3.2 The fermionic masses

The spontaneous symmetry breaking does not generate masses for the fermions. To do so, one should add an interaction of the fermions with the Higgs field. This is done by adding the following Yukawa term for fermions:

$$\mathscr{L}_{Yukawa} = -C_f \overline{\Psi}_L \Phi \Psi_R^* + H.C.$$

where C_f is the Yukawa coupling constant for the f fermion. This term is invariant under the $SU(2) \times U(1)$ transformations. As done before, we write the Higgs field as a function of the Goldstone fields, Θ^a, and the H(x) field. The Goldstone fields are absorbed by the gauge transformation. The resulting Lagrangian is formed of two terms:

$$-\frac{C_f}{\sqrt{2}} v \overline{\Psi}_f \Psi_f \quad \longrightarrow \quad \text{Mass term}$$

$$-\frac{C_f}{\sqrt{2}} v \overline{\Psi}_f \Psi_f H \quad \longrightarrow \quad \text{Interaction term}$$

We can conclude that all fermions interact with the Higgs boson in the same way with a coupling constant proportional to their mass:

$$C_f = \sqrt{2}\frac{m_f}{v}$$

In the SM, three fermion families are present and the Yukawa coupling constants are 3×3 matrices. There is no fundamental reason for these matrices to be diagonal and the general case of an arbitrary matrix is considered. However, physical particles are mass eigenstates. We should diagonalise these coupling constants to change from the interaction eigenstates to the physical eigenstates. This transformation naturally includes a unitary matrix that mixes the 3 families in the quark sector. This matrix is the Cabibbo, Kobayashi, Maskawa (CKM) matrix [18, 19]. For a SM without neutrino masses, this matrix can be absorbed by an arbitrary

transformation of the neutrinos eigenstates in the lepton sector . One should note that the presence of neutrino masses, as shown by the last experimental data, introduces an equivalent of the CKM matrix, the Pontecorvo, Maki, Nakagawa, Sakata (PMNS) matrix [20, 21], for the lepton sector.

1.4   Summary on the Standard Model

We can summarise the SM by the Lagrangian:

$$\mathscr{L}_{SM} = \mathscr{L}_{gauge} + \mathscr{L}_{fermion} + \mathscr{L}_{Higgs} + \mathscr{L}_{Yukawa}$$

$\mathscr{L}_{gauge}$ represents the gauge bosons and their self-interaction and is given by:

$$\mathscr{L}_{gauge} = -\frac{1}{4}B^{\mu\nu}B_{\mu\nu} - \frac{1}{4}W^{i\mu\nu}W_{i\mu\nu} - \frac{1}{4}G^{a\mu\nu}G_{a\mu\nu}$$

B, W^i and G^a represent the bosons corresponding respectively to the u(1), su(2) and su(3) algebra. A simple rotation of θ_W, dictated by the Higgs mechanism, allows us to write the interaction terms as function of physical bosons:

$$\frac{1}{4}B^{\mu\nu}B_{\mu\nu} + \frac{1}{4}W^{i\mu\nu}W_{i\mu\nu} = \frac{1}{4}F^{\mu\nu}F_{\mu\nu} + \frac{1}{2}W^{+\mu\nu}W_{\mu\nu}^- + \frac{1}{4}Z^{\mu\nu}Z_{\mu\nu}$$

where $F^{\mu\nu}F_{\mu\nu}$ correspond to the Maxwell field strength.

$\mathscr{L}_{fermion}$ represents the fermions and their interactions with bosons and is given by:

$$\mathscr{L}_{fermion} = \sum i\overline{\Psi}\slashed{D}\Psi$$

where $\slashed{D} = i\gamma^\mu \left[\partial_\mu + ig_1\tilde{\rho}(B_\mu) + ig_2\tilde{\rho}(W_\mu^a) + ig_3\tilde{\rho}(G_\mu^b)\right]$. This insures the gauge symmetry and introduces the interaction between bosons and fermions. $\tilde{\rho}(A_\mu)$ is the representation of the boson following the representation-space described in table 1.4.

$\mathscr{L}_{Higgs}$ and $\mathscr{L}_{Yukawa}$ are respectively the Higgs and the Yukawa mass Lagrangian described in sections 1.3.1 and 1.3.2.

The SM has 18 free parameters[2]. These can be described as the 9 masses and the 4 parameters of the CKM matrix in the fermion sector, the mass of the W boson, the mass of the Higgs bosons and the 3 coupling constants in the boson sector. One can also add one more parameter, θ QCD, that is naturally present in the QCD Lagrangian. This parameter is responsible for the CP violation in the strong interaction sector. However, all experimental data shows that this parameter is compatible with zero.

---

[2]For a Standard Model with massless neutrino. If one wants to include the neutrino masses, we need at least 7 new free parameters corresponding to the 3 neutrino masses and the 4 parameters of the PMNS matrix.

1.5 Our current knowledge of the Higgs boson

The Higgs boson mass is the only unknown parameter of the SM. The determination of the Higgs boson mass is very important to constrain the Higgs sector of the electroweak theory. Several indications on the Higgs boson mass can be derived from some theoretical assumptions as well as from electroweak experimental data and direct searches.

1.5.1 Theoretical limits on the Higgs boson mass

Even if the Higgs boson mass is not predicted by the SM, different theoretical limits can be derived using different assumptions and approximations. We will not list all these in detail here but we will just focus on the general approach to compute a lower and an upper limit on the Higgs mass. For further details the readers are referred to [22, 23, 24].

As seen in section 1.3.1, the Higgs mass is given by $v\sqrt{2\lambda}$. This is given at tree level and quantum corrections will appear at higher orders. These corrections lead to some divergences and a renormalisation procedure is needed. Using the renormalisation group equation, the running λ coupling is given by:

$$\frac{\partial \lambda(Q)}{\partial ln \frac{Q^2}{Q_0^2}} = \frac{1}{16\pi^2} \left(12\lambda^2 + 6\lambda C_{top}^2 - 3C_{top}^4 + \text{extra terms}\right)$$

where λ is the self coupling and C_{top} the top Yukawa coupling. If the Higgs self-coupling is larger than the top Yukawa coupling, we can neglect the terms with C_{top}. The Higgs self-coupling, $\lambda(Q)$, will diverge with energy as $\lambda^2 ln(Q^2)$. If we want the SM to stay valid at all scales ($Q \to \infty$) one should set λ to 0. This implies a trivial non-interacting theory. Even if we chose λ, at the electroweak scale, very small, $\lambda(Q)$ would eventually blow up at a certain scale given by the Landau pole extracted from:

$$\lambda(Q) = \frac{\lambda_{ew}}{1 - \frac{3\lambda_{ew}}{4\pi^2} ln \left(\frac{Q^2}{v^2}\right)}$$

The Higgs mass, and thus the λ parameter at electroweak scale, should be chosen in a way which ensures the perturbativity up to a certain scale where new physics would interfere and correct this divergence. This upper limit on the Higgs mass is called the triviality bound.

On the other hand, if the Yukawa top coupling is larger then the Higgs self coupling, $\lambda(Q)$ will be driven by the $-C_{top}^4$ term. The Higgs potential will develop a global minimum at large scale and therefore the vacuum will become unstable. One should choose λ high enough at the electroweak scale to ensure the positivity

of $\lambda(Q)$ at a certain scale where we want the theory to stay valid. This introduces a lower bound on the Higgs mass also called the vacuum stability bound. Figure 1.2 shows the Higgs mass upper and lower limit as function of the scale Λ at which we want the SM to remain valid. If the scale of new physics is the Planck scale, the Higgs boson mass bound is 130 GeV$< m_H <$180 GeV.
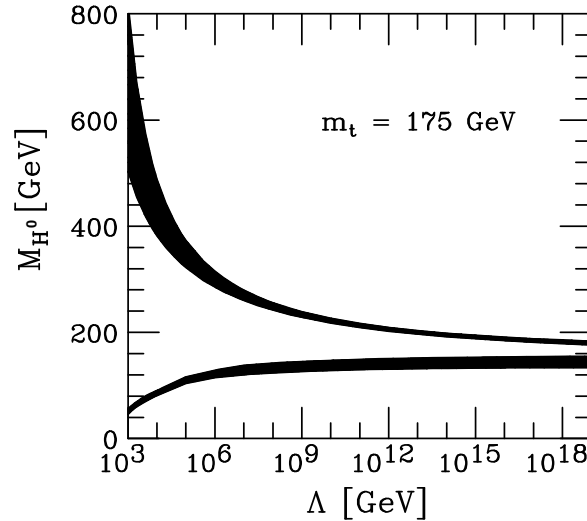
Figure 1.2: Theoretical upper and lower bounds on the Higgs boson mass as function of the the scale Λ at which one wants the SM to remain valid [24].

One should note that the previous calculation is made at one-loop level, assuming that this perturbative approach is accurate enough to describe the λ parameter at high scales. Further orders and even lattice calculation, where the theory become non-perturbative, are needed to have a clearer idea of the Higgs mass bounds. Some of these detailed calculation can be found in [25].

1.5.2   Direct limits on the Higgs boson mass

The best experimental lower limits on the Higgs mass come from the LEP experiments. In the last months of the LEP operation, several $ee \longrightarrow ZH$ candidates were registered by the ALEPH experiment. The candidates corresponded to a Higgs boson of a mass around 115 GeV[26]. The combination with the other LEP experiments didn't show any significant excess. The LEP experiment eventually put a lower limit of 114.4 GeV with 95% confidence level (CL) [27].

Both CDF and $D\emptyset$ experiments at the Tevatron are searching for the Higgs boson. Several Higgs production and decay modes were used to cover a wide range of possible Higgs mass (110-200 GeV). The combined results from both CDF and $D\emptyset$ are summarised in figure 1.3. This plot shows the limits at 95% C.L.

17

Tevatron Run II Preliminary, L=0.9-4.2 fb^{-1}
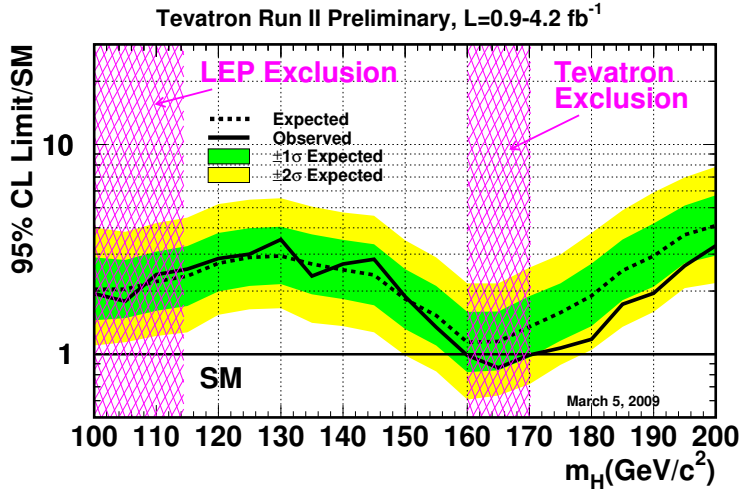
Figure 1.3: Limits at 95% C.L. on the ratio σ/σ_{SM} of the SM Higgs boson production cross-section measured at the Tevatron divided by the SM expected value, as a function of the Higgs boson mass [28].

on the ratio σ/σ_{SM} of the SM Higgs boson production cross-section measured at the Tevatron divided by the SM expected value, as a function of the Higgs boson mass [28]. Thanks to a good sensitivity at high mass with the $H \rightarrow WW$ channel, the Higgs boson is excluded in a mass range between 160 GeV and 170 GeV @ 95 C.L. At low mass, an exclusion (and a fortiori a discovery) is much more difficult: currently the excluded cross section is still three times higher than the SM cross section for $m_H = 120$ GeV.

1.5.3 Electroweak experimental constraints on the Higgs boson mass

In the SM, at tree level the Higgs boson mass is a free parameter. However it is related to several electroweak quantities at quantum level. This comes from higher order corrections where loops including the Higgs boson interfere with the calculation of physical observables. As an example, we consider the ρ parameter given by:

$$\rho = \frac{m_W^2}{m_Z^2 \cos^2(\theta_W)}$$

18

Form equation 1.1 one can see that $\rho=1$ at the tree level. The quantum corrections, at one loop, $\Delta\rho$ are given by:

$$\Delta\rho \simeq \frac{\alpha}{\pi}\frac{m_{top}^2}{m_Z^2} - \frac{\alpha}{\pi}log\frac{m_H^2}{m_Z^2}$$

Where α is the fine structure constant. This allows to constrain the Higgs mass using the top quark and W boson masses. We can see that the corrections depend logarithmically on the Higgs boson mass. A small error on the W and top quark mass can therefore induce a large error on the Higgs mass determination. The current status with the latest measurements is shown in figure 1.4.
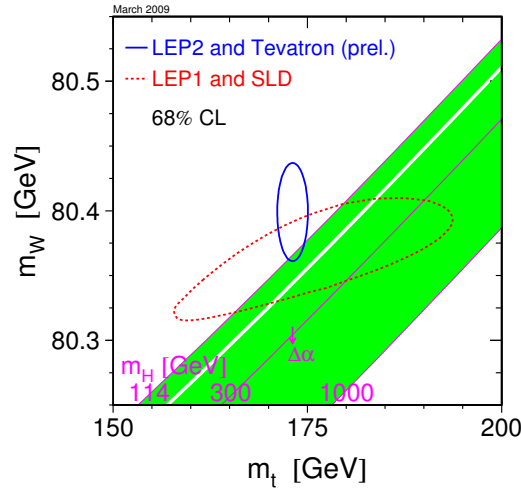
Figure 1.4: Allowed (at 68% C.L.) Higgs boson mass as function of the measurements of the W boson and the top quark masses [29].

A general fit with Higgs quantum corrections and including 17 electroweak observables measured at LEP/SLD, m_W (LEP/Tevatron) and m_t (Tevatron) was performed [30]. The χ^2 of this fit as function of the Higgs mass is represented in figure 1.5. The general fit result is $m_H = 90^{+36}_{-27}$ GeV (68% C.L.) [29], or equivalently, $m_H < 163$ GeV at 95% C.L.

1.6 Beyond the Standard Model

The SM can explain, with high precision, most of the experimental data available until now. However the SM presents some theoretical and conceptual problems:

19
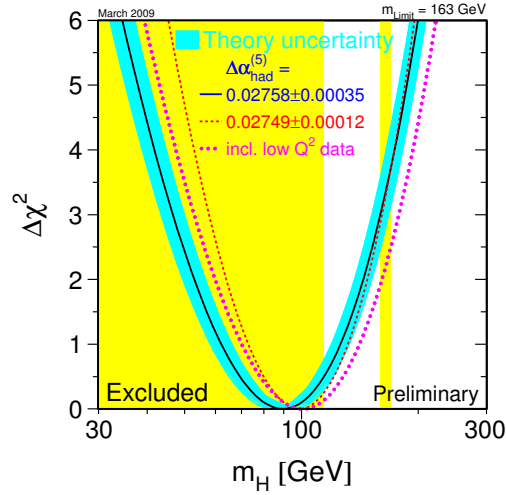
Figure 1.5: χ^2 variation as a function of the Higgs mass, from the global electroweak fit, assuming the SM is valid. The minimum corresponds to the most probable value for the Higgs mass given by the fit [29].

- the SM does not include the gravitational interaction described by the General Relativity;

- the CP violation in the electroweak sector is not sufficient to explain the matter anti-matter asymmetry seen in the universe;

- no candidate for the dark matter is provided by the SM;

- some fine tuning is needed to deal with some of the SM divergences especially in the Higgs sector;

- the SM does not explain the hierarchy problem, especially the 17 orders of magnitude between the weak and the Planck energy scales (in other words, why the gravity is so weak compared to the other interactions);

- it does not explain why the CP violation in the strong sector, represented by the θ QCD angle, is compatible with zero.

All of these reasons make physicists think of the SM as an effective theory, at low energy, of a more general theory. New physics will appear at a certain scale where the SM calculations become invalid. At this scale new physics can correct the eventual divergences or other problems that the SM presents. More precise knowledge of the SM free parameters, especially the Higgs mass, will provide a

better estimation of the scale at which corrections from new physics will become important.

Several models beyond the SM exist with predictions that match the SM predictions at low energy. One of them is the Supersymmetry, which suggests a new symmetry between the bosons and the fermions. This provides a elegant solution to the divergences in the Higgs sector. Most supersymmetric models also provide natural candidates for dark matter. Several other models are also introduced to solve one or more of the SM problems. None of these models has been experimentally proven, and the LHC will play a critical and unique role by discovering and characterising eventual new physics and/or by proving wrong some models.

Chapter 2

The ATLAS experiment

In this chapter, we will briefly describe the Large Hadron Collider (LHC) and one of the detectors installed upon it (ATLAS). A detailed description of the LHC and of ATLAS can be found respectively in [31] and [32]. We will begin with a short description of the LHC and its physics goals. Then we will list the main properties and expected performances of the ATLAS sub-detectors. An overview of the current status of each sub-detector is also briefly reported. The ATLAS trigger system is described in the last section.

2.1   The LHC

The LHC is the next major step in high energy colliders after the Tevatron at Fermilab. The LHC is located at CERN at the Swiss-French border near Geneva. It is constructed in the existing LEP tunnel of about 27 km long. The LHC is a proton-proton collider with a design instantaneous luminosity of 10^{34} cm^{-2}s^{-1} and a centre-of-mass energy of 14 TeV, allowing to explore the TeV energy range. Table 2.1 lists some of the properties of the LHC collider.

The high-luminosity and energy choices, at the LHC, were dictated by its physics goals (cf. 2.1.2). The proton-proton choice was made because there was no realistic alternative: firstly, a circular electron collider would consume too much electricity to reach this high-energy regime because of the large energy loss by synchrotron radiation. Secondly, a proton anti-proton collider at 10^{34} cm^{-2}s^{-1} instantaneous luminosity would not be feasible given the usually low yield of anti-proton production (one anti-proton produced from a million protons-on-target at the Tevatron).

The instantaneous luminosity at a collider is given by:

$$L = \frac{N_p^2 n_b f_{rev}}{4\pi\sigma^2} F$$

Parameter	Value
Circumference	26.7 km
SPS injection energy	450 GeV
Energy per beam	7 TeV
Synchrotron radiation loss per turn	7 keV
Main dipole nominal field	8.33 Tesla
Main dipole operation temperature	1.9K
Instantaneous nominal luminosity	10^{34} cm^{-2} s^{-1}
Number of bunches	2808
Number of protons per bunch	10^{11}
Time between two bunch crossing	25 ns

Table 2.1: Main LHC general parameters for nominal operations.

where N_p is the number of protons per bunch, n_b the number of bunches per beam, f_{rev} the beam revolution frequency, σ the transverse beam dispersion and F a geometric correction factor due to the crossing angle of the two beams. To increase the luminosity, one can increase the bunch crossing frequency ($n_b f_{rev}$) or increase the density of protons ($N_p^2/4\pi\sigma^2$) per bunch. Increasing the bunch crossing frequency is limited by the experiments electronics and trigger speed. Increasing the proton density will lead to an increase of multiple interactions per bunch crossing (pile-up). At nominal luminosity the LHC will operate at 40 MHz bunch crossing frequency. This configuration will lead to an average of 23 pile-up events.

There are four experiments at the LHC:

- ATLAS and CMS: the two general-purpose experiments. They use different technologies for their corresponding detectors especially for the magnet and calorimetry systems. The ATLAS detector will be discussed in more details in what follows;

- LHCb: a dedicated experiment to study B mesons. Its main physics purpose is to study flavor physics e.g. the CKM matrix parameters and CP violation;

- Alice: an experiment for heavy-ion collisions. The LHC can also collide heavy ions. Alice is designed to study these high-energy events where the quark-gluon plasma can be created.

The first successful beam injections in the LHC was done in September 2008 but an unfortunate serious accident delayed the startup. The LHC is currently under repair and is expected to deliver the first collision data at the end of 2009.

The LHC startup could be at a centre of mass energy of 10 TeV and it is not expected to reach the design energy of 14 TeV before the end of 2010. The LHC

is expected to start with an instantaneous luminosity of 10^{-31} to 10^{-32} cm^{-2}s^{-1}. With this luminosity, the LHC is expected to deliver about 200pb^{-1} during years 2009-2010. In the initial schedule, the LHC design luminosity of 10^{34} cm^{-2}s^{-1} was supposed to be reached after 3 years of operation at a lower luminosity of 10^{33} cm^{-2}s^{-1} during which 30fb^{-1} were to be collected. This amount of data should be sufficient to discover the Higgs boson and to discover, or constraint, a large number of models beyond the Standard Model.

2.1.1 Proton-proton phenomenology

Protons are composite particles and the real hard-collisions at the LHC will occur between partons, the constituents of the protons. At the LHC, 85% of the hard events will be initiated by a gluon-gluon collision. The partons will carry a fraction of the energy of the proton: not all collisions will happen at the same energy in the partonic centre-of-mass, $\sqrt{\hat{s}}$. This allows to scan a large range in $\sqrt{\hat{s}}$, which is an advantage for a discovery machine. However, this also presents some disadvantages especially for precision measurements: the fact that the partonic initial energy is unknown complicates the reconstruction of some events e.g.with missing energy. Moreover, the interactions between valence quarks, see quarks and gluons inside the proton are not perturbative and can not be calculated within the QCD. The fraction of energy carried by each of the partons is parametrised by the Parton Density Functions (PDF). These semi-empiric equations are fitted with different experimental data, e.g. Tevatron and Hera, and extrapolated to the LHC energy. This introduce a new theoretical uncertainty to the observable determinations. Another disadvantage of the proton-proton colliders is the presence of underlying events produced from secondary interaction of the proton remnants. Underlying events are not well described by currently available models. These interactions create low-p_T jets that can contaminate the hard-process final state.

The cross-sections for several physics processes at the LHC are presented in figure 2.1. We can clearly see the large inelastic cross-section: the experiments must reject this large QCD background. Standard Model benchmark processes such as W and Z boson production have a cross-section around 100 nb. The top quark pair production, with a cross-section of about 800 pb, is two order of magnitude higher than at the Tevatron collider. More interesting events such as some Supersymmetry processes and especially the Higgs production have lower cross-sections by several orders of magnitude.
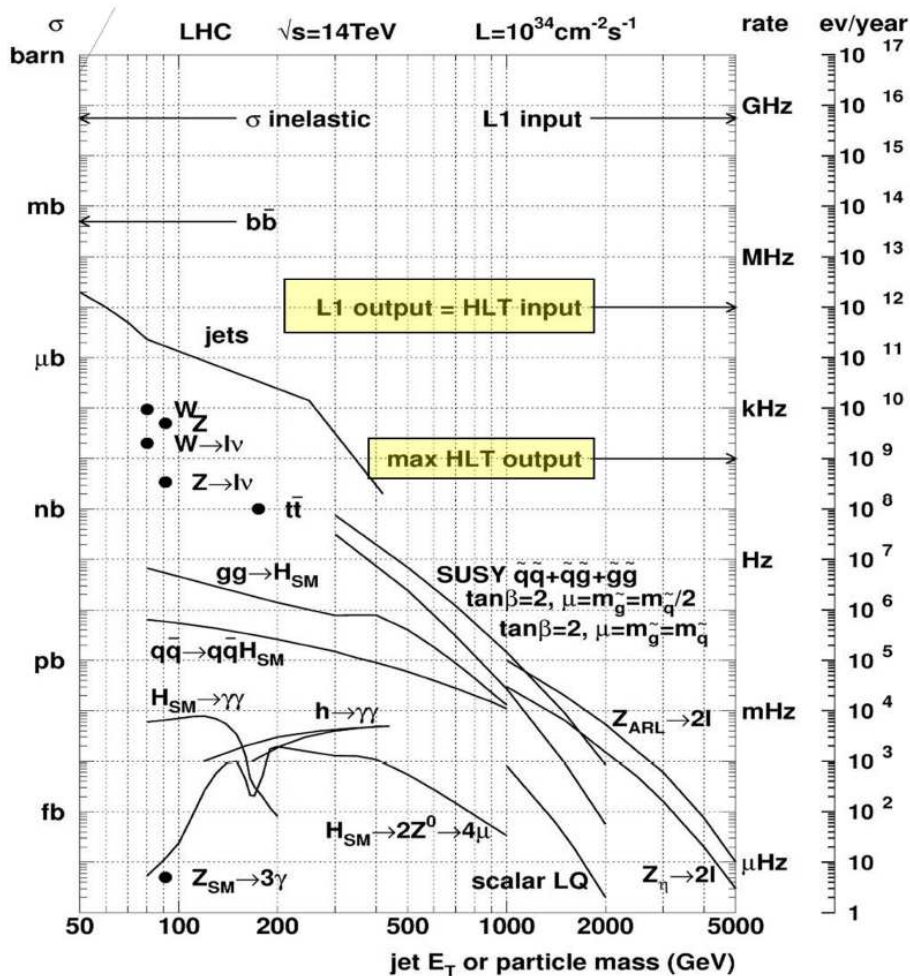
Figure 2.1: Cross-section of various physics processes at the LHC (with nominal parameters). The cross-section is given as a function of the E_T of jets or as a function of the particle mass for hypothetical particles [1].

2.1.2 Physics goals of the general-purpose experiments at the LHC

The ATLAS and CMS experiments are designed to precisely measure some of the Standard Model parameters as well as to detect new particles. The understanding of the origin of the symmetry breaking in the electroweak sector is of great importance. The Higgs mechanism is presumably responsible of this symmetry breaking: the Higgs boson search was used as a benchmark to guide and optimise the design of the detectors.

The LHC will also be a real top-quark factory. Many of the top-quark proper-

ties haven't been measured at the Tevatron or were measured with low precision. The LHC will allow a better understanding of the only quark that can be seen as a free state. The top will also be the main background for most of the physics channels: controlling this background is mandatory for Higgs searches and for many searches for new physics.

Several theoretical assumptions predicts new physics at the TeV scale. If new physics lies at the TeV scale, it should be detected at the LHC. Both ATLAS and CMS are expected to provide discoveries and/or tight limits for a large set of physics models beyond the Standard Model: for instance s-particles in supersymmetric models and heavy gauge bosons of masses up to a few TeV will be at the reach of the ATLAS and CMS experiments. Some of these particles can be detected with few pb^{-1} of data.

2.2 The ATLAS detector

Figure 2.2: General view of the ATLAS detector showing the different sub-detectors [32].
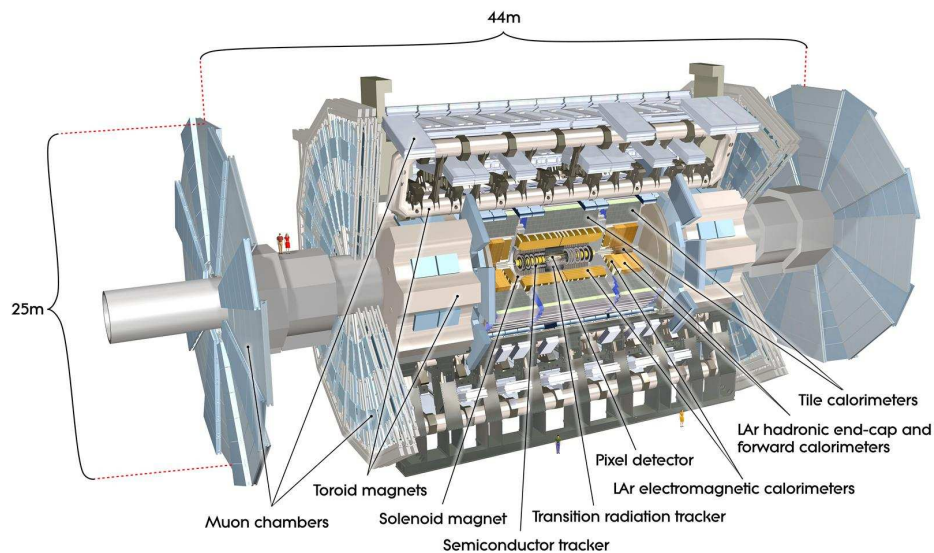
ATLAS, A Toroidal LHC ApparatuS, is one of the general-purpose experiments at the LHC. The ATLAS detector overall design is shown in figure 2.2. ATLAS is a classical cylindrical detector formed mainly of three sub-detectors:

- the inner detector or inner tracker which is surrounded by a solenoidal magnet;

- the electromagnetic and hadronic calorimeters;

- the muon spectrometer embedded in an air-core toroid magnet.

The ATLAS coordinate system is described briefly hereafter as it will be used throughout this report. The x-y transverse plane is defined as perpendicular to the beam direction. The positive x-axis points toward the centre of the LHC ring. The positive y-axis points upwards. The beam direction defines the z-axis, $\{x,y,z\}$ being a direct coordinate system. ϕ is the azimuthal angle with the x-axis in the transverse plane, θ is the polar angle with respect to the z-axis. The pseudo-rapidity η is given by $\eta = -ln\,tan\left(\frac{\theta}{2}\right)$. The distance ΔR in the η-ϕ plane is given by $\Delta R = \sqrt{\Delta\eta^2 + \Delta\phi^2}$.

Some of the ATLAS detector main features are listed in table 2.2. The detector should fulfil a wide set of requirements for physics:

- fast and radiation hard electronics to cope with the high LHC luminosity;

- high detector granularity for a good precision and a good separation of particles created with a large flux at the LHC;

- full azimuthal coverage and a large acceptance in pseudo-rapidity for full event reconstruction especially events with complex final state. This is also important for missing energy determination;

- good identification of tracks in the inner detector with both high efficiency and high resolution. As an example, this is needed for b-jet identification, which is mandatory for channels like the $t\bar{t}H(b\bar{b})$ channel;

- good electron/photon identification in the electromagnetic calorimeter and large coverage of the hadronic calorimeter to detect forward jets created in a hadronic collider. Both calorimeters must have a high resolution in energy and also a good resolution in position. For example, the Higgs search in the $H \rightarrow \gamma\gamma$ channel relies on excellent performance of the electromagnetic calorimeter;

- good muon identification and muon momentum resolution, with p_T selection at the first trigger level. Good reconstruction of high-p_T muons up to a TeV is needed for an eventual discovery of heavy gauge bosons;

- efficient and fast trigger to extract channels with low cross-section while rejecting the huge QCD background.

Parameters	ATLAS
Total weight (metric tons)	7000
Overall diameter (m)	25
Overall length (m)	44
Total cost (millions of Swiss francs)	550

Table 2.2: Main ATLAS general parameters.

Detector parts	Resolution	Coverage	
		Measurement	Trigger L1
Inner tracking	$\sigma_{p_T}/p_T = 0.05\% p_T \oplus 1\%$	$|\eta| < 2.5$	-
EM calorimeter	$\sigma_E/E = 10\%/\sqrt{E} \oplus 0.7\%$	$|\eta| < 3.2$	$|\eta| < 2.5$
Hadronic calorimeter	$\sigma_E/E = 50\%/\sqrt{E} \oplus 3\%$	$|\eta| < 3.2$	$|\eta| < 3.2$
Forward calorimeter	$\sigma_E/E = 100\%/\sqrt{E} \oplus 10\%$	$3.1 < |\eta| < 4.9$	$3.1 < |\eta| < 4.9$
Muon spectrometer	$\sigma_{p_T}/p_T = 10\%$ at $p_T = 1$ TeV	$|\eta| < 2.7$	$|\eta| < 2.4$

Table 2.3: Main requirements for the ATLAS detector performances. Energies and transverse momenta are quoted in GeV.

Another point noteworthy is that most of these requirements have to be fulfilled for a very wide range of energies, from a few GeV to a few TeV. The performance requirements of the ATLAS detector are summarised in table 2.3.

After the LHC accident in September 2008, the ATLAS detector, including all the sub-detectors, the trigger and data acquisition systems, was commissioned using cosmic rays. This period was important to assess the actual detector status and its performance as a fully integrated system. Detector conditions, timing and trigger issues were the main concerns to operate the detector in a stable manner and maximise the data taking efficiency. One of the cosmic-ray events recorded during this period is shown in figure 2.3. The analysis of this data is ongoing for a better understanding of each of the detector components and also to start tuning the Monte Carlo simulation. The current status of each of the sub-detectors, as established with the cosmic data, will be mentioned in the following descriptions of the sub-detectors.
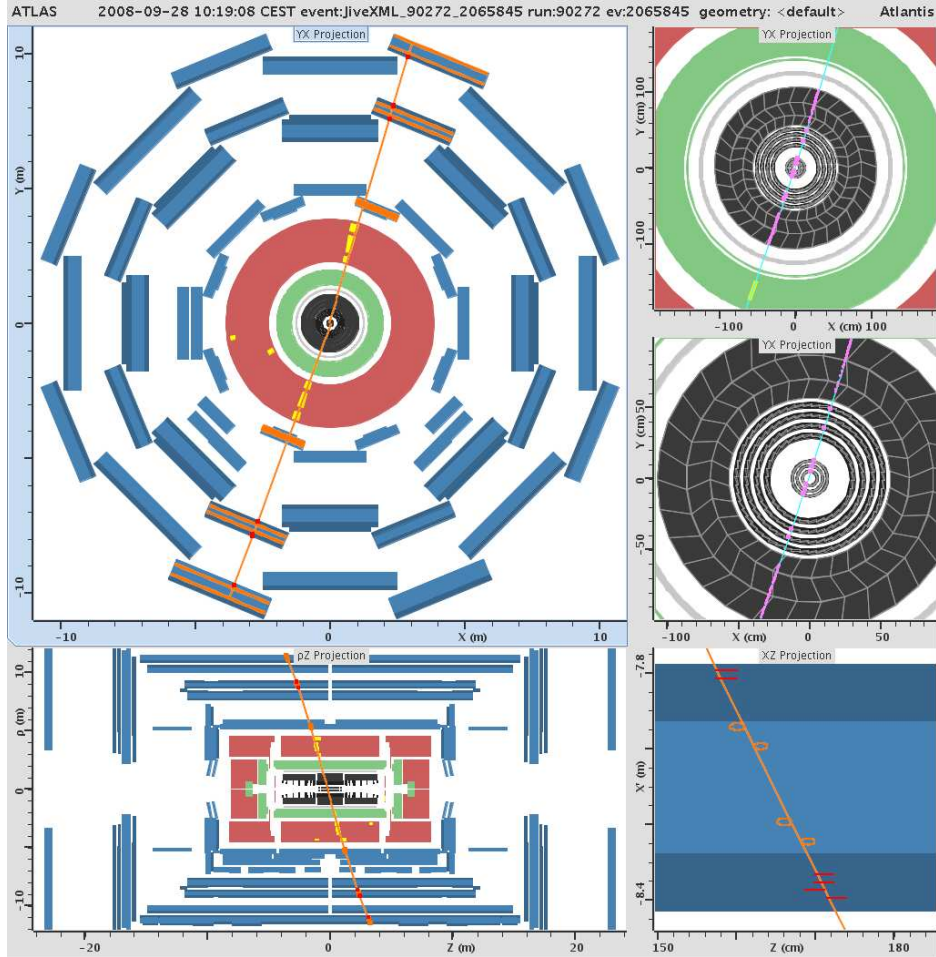
Figure 2.3: Cosmic-ray event recorded in September 2008 and displayed by one of the ATLAS event-display systems (ATLANTIS): the muon crosses all the ATLAS sub-detectors.

2.2.1 The inner detector

The inner detector is the inner tracking system of the ATLAS detector, aimed at reconstructing the trajectories of charged particles. This should be done in an environment with very high track density: a few hundreds of charged particles will pass through the inner detector every 25 ns. High-precision measurements and good pattern-recognition capability require a detector with a fine granularity. The detector is enclosed in a solenoid magnet delivering a 2T axial magnetic field.

Three different and complementary detector technologies were chosen to form the ATLAS inner detector. Silicon-based detectors with different granularities are used close to the interaction point, complemented by a straw-tube detector at

larger radii. The silicon detectors provide high precision measurements for hits on tracks, in $R - \phi$ as well as in z direction, and as close as possible to the interaction point. The straw-tubes provide a large number of measurements, in $R - \phi$ only, spanning a large radius range in order to obtain a good momentum resolution.
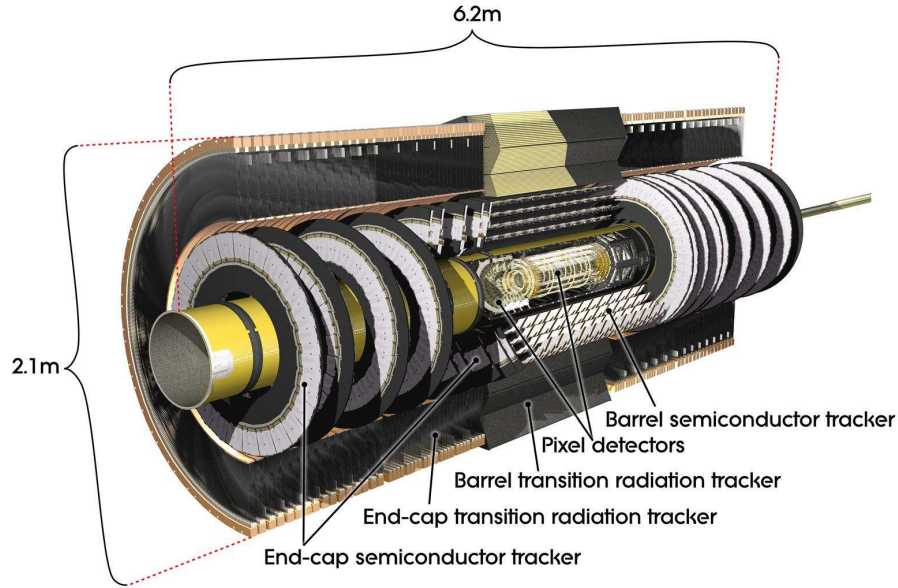
Figure 2.4: General layout of the ATLAS inner detector [32].

The inner detector is illustrated in figure 2.4. Going from the beam-pipe one can find: the pixel detector, the silicon microstrip tracker also known as the semiconductor tracker (SCT) and the transition-radiation tracker (TRT).

2.2.1.1 The pixel detector

The pixel detector is the innermost ATLAS sub-detector. The pixel technology is the most advanced among silicon-based detectors. It is the only technology which can sustain the high level of radiation expected in the vicinity of the interaction point and which furthermore has substantial advantages: low occupancy, very low noise, very high efficiency and 3D measurement with excellent precision. The pixel detector is described more precisely in chapter 3, a short overview will be given here.

The pixel detector is a semi-conductor detector that operates as a diode in reverse polarisation. It is formed of high-granularity n^+n implants connected by bump-bonding to the read-out electronics. A crossing particle will ionise the sensor and the charge will drift in the electric field and will be collected on the n^+ side. The pixel detector sensor, electronics and different services have to cope with

a very high radiation dose next the interaction point. The pixel area of 50×400 μm^2 is dictated by the pitch of the readout electronics. The 50 μm (R-ϕ) to 400 μm (z) ratio was optimised for the best physics performance especially the b-tagging capability. The pixel detector also allows 3D measurements with an excellent resolution: 10 μm in R-ϕ and 115 μm in the Z direction. This will allow an accurate reconstruction of the charged tracks, of the interaction point (primary vertex), and also of the secondary vertices stemming from the decay of particles with lifetime e.g. beauty and charm hadrons and τ-leptons.

The pixel detector is formed of 1744 identical sensors each connected to 16 front-end chips containing 2880 readout channels. This composite object is called a module, and each of these modules contains 46080 pixels. The pixel modules are arranged in three barrel layers, covering the central region, and two endcaps each formed of three disks and extending the coverage up to $\mid \eta \mid < 2.5$.
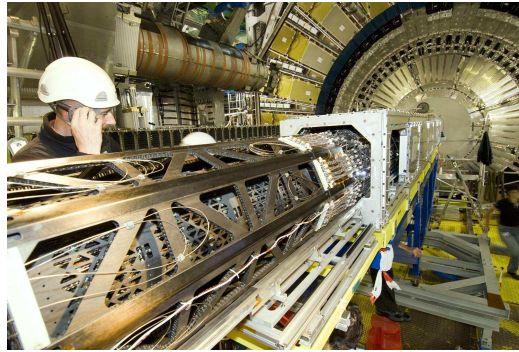
Figure 2.5: Installation of the ATLAS pixel detector and its services in the ATLAS cavern.

The pixel detector is installed and was commissioned using cosmic rays in Autumn 2008. About 96% of the pixel modules were operational and the noise level was very low. Note that a second commissioning period is performed at the time of writing, for which some pixel modules were recovered: 98% of the detector can now be operated. Chapter 3 will describe the pixel detector status and some of the analysis related to noise occupancy and detection efficiency done with the pixel detector in the 2008 commissioning period.

2.2.1.2   The silicon microstrip tracker

The SCT is a semiconductor p-in-n implant detector with the same general detection principle as for the pixel one.

The SCT sensors are formed of 768 strips of 80 μm pitch and $\sim$12 cm long. A SCT module is made of 2 sensors, one on each side. The sensors are rotated by 40 mrad with respect to each other. This allows to have a 2D measurement

using the intersection of the activated strip from both sides. The 40 mrad rotation angle was chosen to minimise the number of intersections between strips from both sides and thus to reduce hits ambiguity. It also brings some robustness by allowing a measurement in the R-ϕ direction even if one of the two sensors is damaged. The sensors are connected to a readout electronics with 1536 channels per module. The barrel and endcap SCT modules have different designs as shown in figure 2.6.

(a) SCT barrel module
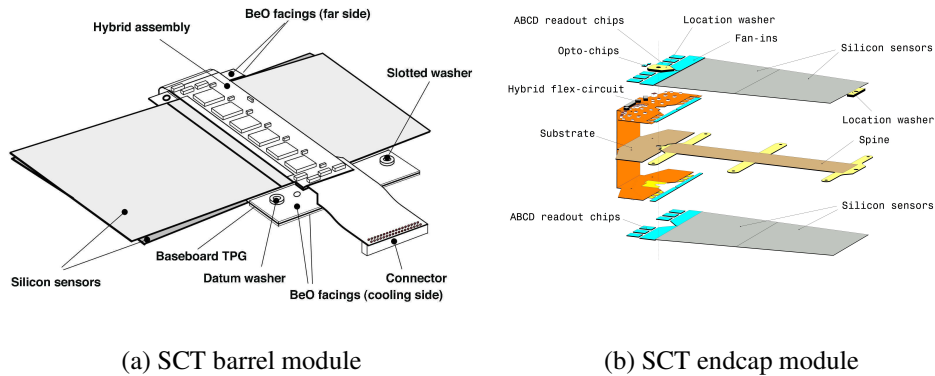
(b) SCT endcap module

Figure 2.6: Layout of the SCT barrel and endcap modules [32].

The SCT modules are mounted on a light support structure mainly formed of carbon fibres. In the central region, 2112 rectangular SCT modules distributed on four cylindric layers form the barrel. Twelve barrel modules are mounted in one row with alternatively a ± 1 mm shift from the cylinder nominal radius. Different rows are positioned with an $11°$ tilt angle with respect to the tangent direction to the support cylinder. This geometry allows overlaps between modules: there is no dead regions. The layer positions are summarised in table 2.4.

On each side of the barrel, there are two endcaps with nine disks each and a total of 1976 modules. Each disk is formed of three types of trapezoidal modules situated at the inner, middle and outer side. Table 2.5 summarises the disks positions and the number of modules for each type on disks.

The SCT detector allows pseudo-3D measurements with an intrinsic accuracy of 17 μm in R-ϕ and 580 μm in the z direction. The noise level in the SCT detector is $< 5 \times 10^{-5}$ in both the barrel and the endcap region. The noise was computed for different conditions and with and without the TRT running. No significant changes in the noise level were detected. After the integration with the TRT on surface, 0.2% of the barrel channels and 0.36% of the endcap channels were defective. After the SCT integration inside ATLAS and during the period of commissioning with cosmic-rays, about 99% of the barrel modules and 97%

Barrel layer	Radius (mm)	Number of modules
Layer 1	284	384
Layer 2	355	480
Layer 3	427	576
Layer 4	498	672

Table 2.4: SCT barrel layers properties. The radii are those of the outer surface of each cylinder.

Endcap disk	z position (mm)	Total number of modules	Number of modules (inner/midle/outer)
Disk 1	854	92	0/40/52
Disk 2	934	132	40/40/52
Disk 3	1091	132	40/40/52
Disk 4	1300	132	40/40/52
Disk 5	1400	132	40/40/52
Disk 6	1771	132	40/40/52
Disk 7	2155	92	0/40/52
Disk 8	2505	92	0/40/52
Disk 9	2720	52	0/0/52

Table 2.5: SCT endcap module distributions.

of the endcaps modules were operationnal. The number of working modules was changing due to off-detector problems that can be recovered. It is expected that more than 99% of the SCT detector modules will be running with the first beam data.

2.2.1.3 The transition-radiation tracker

The TRT is based on drift tubes of 4 mm diameter commonly called straw-tubes. The tubes are filled with a gas mixture of 70% Xe, 27% CO_2 and 3% O_2. The straw surface forms the cathode. The anodes are 31 μm-diameter tungsten wires plated with gold. A passing particle will ionise the gas mixture inside the tubes and the charge will drift and will be collected at the wire end. The drift time can be computed and gives a spatial accuracy of about 130 μm.

For the TRT barrel, the straws are 144 cm long. The wires are separated electrically into two halves and can be read from both sides. Straws are gathered in arrays embedded in polypropylene fibres to form a barrel module. The TRT barrel is formed of three rings of 32 modules each. Up to 76 straw layers are present in the TRT barrel.

The TRT endcap straws are 37 cm-long and are arranged together in wheels.

Each wheel is composed of eight layers of 768 radially-oriented straws. The layers are separated by 8 mm (15 mm) for type-A (type-B) wheels. The space between straw layers is filled with polypropylene. The endcap is divided into two independent sets of wheels. The set that is closer to the interaction point is formed of 12 type-A wheels. The other set is formed of 8 type-B wheels.

The TRT provides about 32 measurements in R-ϕ, with a precision of 130 μm, up to $\eta < 2$. The TRT external radius of 1.08 m provides a large sagitta for tracks bent by the magnetic field. This is important for a better precision on the momentum measurement of a charged particle and also for a better positive-negative charge separation. In addition the TRT helps in identifying electrons. Indeed the polypropylene that is present between straws serves as a transition-radiation material. Transition photons will be mostly emitted by electrons due to the small mass of the latter. These photons are absorbed by the gas mixture inside the straw and yield a large signal amplitude. The TRT electronics provides two thresholds to distinguish these high amplitude signals. The crossing of an electron leads to at least 7 straws with a high-amplitude signal.

After installation in ATLAS, 1.9% of the barrel straws and 1.7% of the endcap straws were dead. The noise level is computed to be less than 2% with a low threshold set to 250 eV.

2.2.1.4   Inner detector environmental services

Controlling environmental conditions is mandatory for a stable operation of the detector and to prevent severe detector damages. The high granularity requires dense electronics that produce a great amount of heat. An efficient cooling system should remove up to 85 kW of heat from the ID volume at nominal luminosity.

The pixel and the SCT detectors share the same cooling system (an evaporative cooling system). The C_3F_8 coolant is enough radiation-hard. The silicon sensors are expected to operate at about -7°C to minimise the impact of radiation damage. Both pixel and SCT detectors will operate in a dry N_2 gas flow. This will insure a low dew point and therefore no accumulation of humidity on the sensors and the frontend electronics.

The TRT straw tubes and electronics will be operated at room temperature. The heat will be removed by a C_6F_{14} coolant. CO_2 gas is used to fill the TRT volume. This will reduce contamination of the straw inner gas by other molecules that can degrade the performances.

2.2.2   The calorimeters

Different technologies were used to build the ATLAS calorimetric system and fulfil the good energy resolutions, good position accuracy and large coverage re-

quirements. The calorimeter should also fully contain the electromagnetic and the hadronic showers and reduce hadron punch-through to the muon system. The calorimetry system can be divided into 3 main parts: the electromagnetic calorimeter, the hadronic calorimeter, and the forward calorimeter. The overall ATLAS calorimeter system is drawn in figure 2.7.
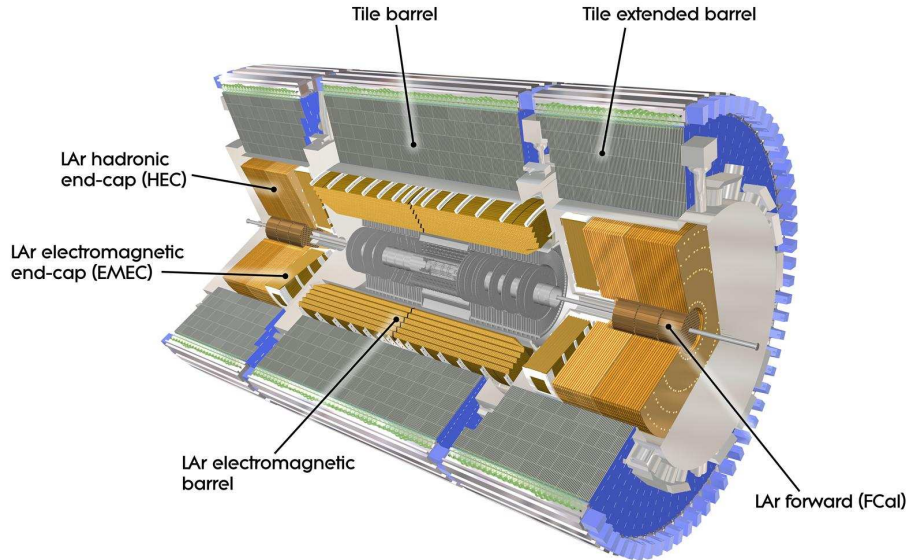
Figure 2.7: General view of the ATLAS calorimetry system showing the different parts of the electromagnetic, hadronic and forward calorimeters [32].

2.2.2.1 The electromagnetic calorimeter

The electromagnetic calorimeter is a sampling calorimeter formed of lead absorbers and kapton electrodes immersed in a liquid argon active material. The accordion geometry of the electrodes leads to a full ϕ coverage with high hermicity. The electromagnetic calorimeter is divided into three parts each housed in a different cryostat. The centre part (called the barrel) is composed of two identical halves separated by a small gap at η=0. The barrel covers the region $|\eta| <$1.475. The barrel is extended by two endcaps each formed of two wheels. The outer wheel covers the region 1.375$< |\eta| <$2.5 and the inner wheel completes the coverage till $|\eta|$=3.2.

For the barrel and the endcap inner wheels, the calorimeter is longitudinally segmented into three layers. This ensures a precise measurement in the region also covered by the inner tracker ($|\eta| <$2.5). The first layer is finely granular in
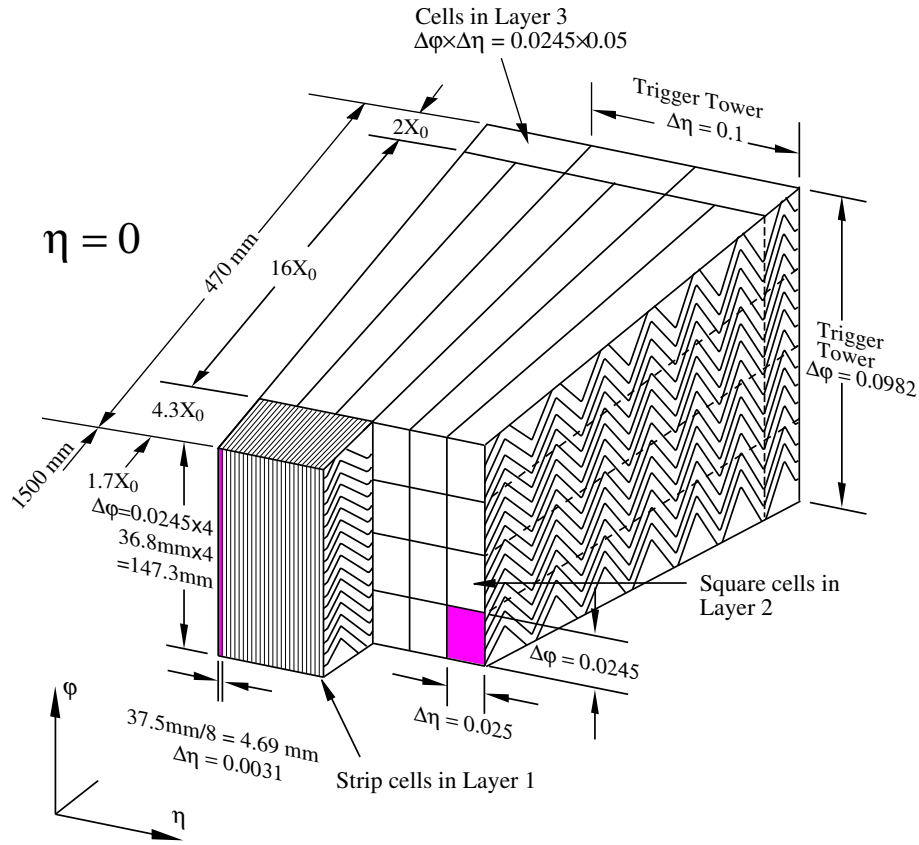
Figure 2.8: Schematic view of a module from the barrel electromagnetic calorimeter. The granularity in η and ϕ directions for each of the three layers is also shown [32].

η direction and thus give the best calorimeter η measurement. The second and third layers provide a better granularity in ϕ direction. A schematic view of the three longitudinal layers is represented in figure 2.8. The endcaps outer wheels are segmented into two layers with a coarser granularity in both directions. The region with $|\eta| < 1.8$ is covered by a presampler situated in front of the electromagnetic calorimeter. This presampler helps to estimate the energy loss due to the material in front of the calorimeter.

In Autumn 2008 during the first ATLAS detector commissioning with cosmic rays, 0.5% of the electromagnetic channels were dead. Only 0.015% of them have on-detector problems, the other channels can be recovered. In addition 0.38% of the channels have calibration problems but can be operated. Only four of the 173312 channels show a high noise level.

2.2.2.2 Hadronic calorimeter

Different technologies were used to build the ATLAS hadronic calorimeter barrel and endcaps. The barrel is formed of steel as an absorber and scintillating tiles as active material. The barrel is divided into a central part covering $|\eta| < 1.0$ and two extensions on each side covering $0.8 < |\eta| < 1.7$. It is segmented into three longitudinal segments of 7.4 total interaction lengths.

The endcaps are liquid argon calorimeters with copper plates as absorber material. They use the same cryostat as the electromagnetic calorimeter endcaps. Each endcap is divided into two independent wheels that cover the region with $1.5 < |\eta| < 3.2$.

2.2.2.3 Forward calorimeter

To allow a measurement of forward jets and a better estimation of the missing energy, two forward calorimeters (FCal) were set at each side of the ATLAS detector. These calorimeters also help limiting the background in the muon chambers.

The forward calorimeters are divided longitudinally into 3 modules. The first module, closer to the interaction point, uses copper as absorber and is optimised for electromagnetic detection. The two other modules use tungsten as absorber and are optimised for hadronic detection. All three modules share the same liquid argon cryostat as the other calorimeter endcaps. A schematic view of the FCal is represented in figure 2.9.
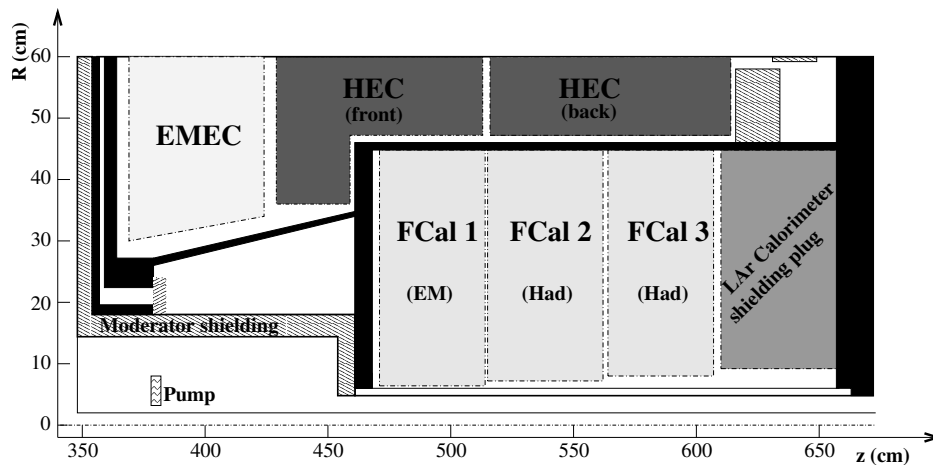

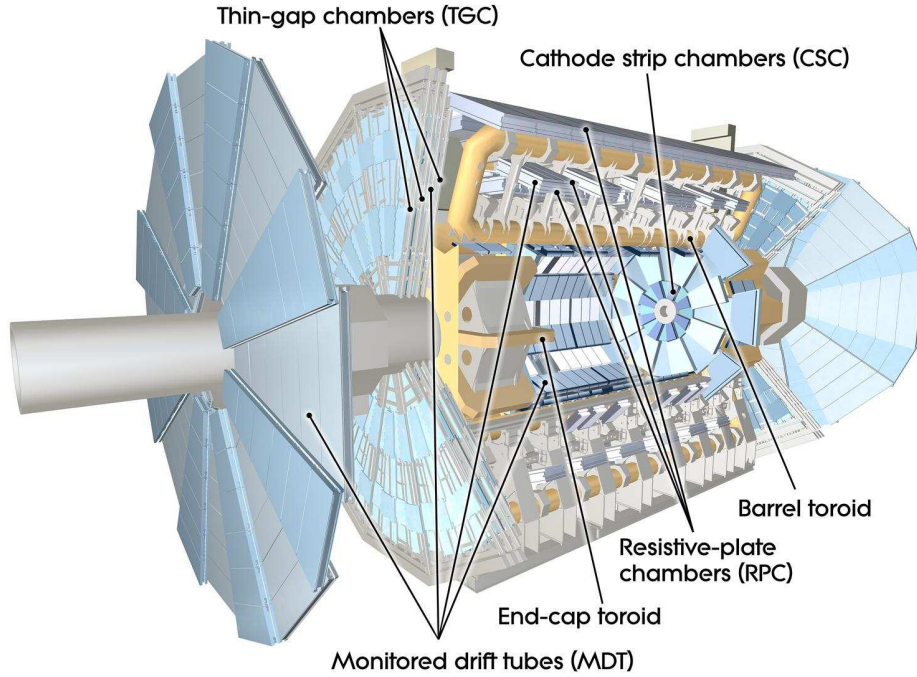Figure 2.9: Schematic view of the three modules of the FCal [32].

Figure 2.10: Overview of the ATLAS muon system [32].

2.2.3 The muon spectrometer

The muon system forms the outermost of the ATLAS sub-detectors and it is represented in figure 2.10. It consists of four different types of muon chambers operating in a toroidal magnetic field. The magnetic field is generated by three air-core toroids. Two toroids forming the endcaps are inserted in the larger toroid that covers the barrel region. Two types of chambers are used for precision measurements in the principal binding direction of the magnetic field. This allows the best precision on the track momentum. Both barrel and endcaps are formed of three layers of muon chambers.

At $|\eta| =0$, there is a hole in the muon system to allow the passage of services for different sub-systems. The Monitored Drift Tube (MDT) covers all the region of $|\eta| <2.7$ but for the innermost layer of the endcaps region at $2.0< |\eta| <2.7$ the MDTs are replaced by Cathode Strip Chambers (CSC).

The MDT's are formed of drift tubes containing a gas mixture of 93% Ar and 7% CO_2. The central wire is formed of tungsten and rhenium with a diameter of 50 μm. The single tube resolution is 80 μm. The CSC's chambers are more adapted to high rates of particles. That is why they are chosen for the inner end-caps layer where the particle flux is high. The CSC are multi-wire proportional chambers with both cathodes segmented in perpendicular directions. This allows

a measurement in both directions. The resolution for a CSC plane is 60 μm in the binding direction while it is 5 mm in the non-binding direction.

The precision chambers are aligned using an embedded optical alignment system. This system allows a monitoring of inter-chamber positions as well as chamber distortions.

Two other types of chambers are used as a trigger system. The Resistive Plate Chambers used in the barrel region and the Thin Gap Chambers (TGC) in the endcap region. These chambers cover the region with $|\eta| <$2.4. They allow a fast but less precise measurements. The measurement is done in the non-binding direction and thus it is complementary to the MDT measurements.

2.3   The ATLAS trigger system

With a 40 MHz bunch crossing frequency, it is impossible to treat and register the huge amount of data delivered by the LHC. It is mandatory to reduce the data by rejecting most of the QCD background that is less interesting for the ATLAS physics program.

ATLAS trigger system is formed of three levels: the level 1 trigger (L1), the level 2 trigger (L2) and the event filter (EF). The L2 together with the EF form what we call the High Level Trigger (HLT).

The L1 uses reduced-granularity information from the entire calorimetry system and from the trigger muon chambers. The L1 trigger is made from hardware electronics. It will search for high-p_T muons, electrons and jets candidates as well as events with high total transverse energy and large missing transverse energy. The data from each sub-detector will wait in pipelines for the L1 trigger decision. This decision must be made within 2.5 μs after the bunch crossing. The L1 output rate is 75 kHz.

The L2 trigger uses more refined information in the regions of interest. The regions of interest are determined by the L1 trigger as region with possible trigger objects. This approach reduces the amount of data that the L2 trigger has to read and process and therefore the trigger decision time. The L2 trigger will reduce the event rate to 3.5 kHz.

The EF is the last step before storing the data. It uses the full detector information and runs the full event reconstruction using offline algorithms. This will significantly enhance particle identification and selection efficiency. The EF reduces the event rate to 200 Hz. Both L2 and EF are built with commercial computer and networking hardware.

Several trigger menus exist in ATLAS for both physics and calibration purposes. The trigger settings will depend on the instantaneous luminosity changes of the LHC. To give a general overview of the ATLAS trigger menu, the most

relevant menus at 10^{33} cm^{-2}s^{-1} for different physics channels are listed in table 2.6.

Trigger name	Trigger description	Threshold at 0% prescale
e25i	Isolated electron	$p_T>25$ GeV
2e15i	two isolated electrons	$p_T>15$ GeV
e60	one electron	$p_T>60$ GeV
g60	one photon	$p_T>60$ GeV
2g20i	two isolated photons	$p_T>20$ GeV
mu20	one muon	$p_T>20$ GeV
tau25i+XE40	one isolated τ-lepton + missing energy	$p_T>25$ GeV + $\not{E}_T>40$ GeV
jet160	one jet	$p_T>160$ GeV
2jet120	two jets	$p_T>120$ GeV
3jet65	three jets	$p_T>65$ GeV
4jet55	four jets	$p_T>55$ GeV
mu10+e15i	one muon + one isolated electron	$p_T>10$ GeV + $p_T>15$ GeV
j45+met50	jet + missing energy	$p_T>45$ GeV + $\not{E}_T>50$ GeV

Table 2.6: Most relevant trigger menu at 10^{33} cm^{-2}s^{-1}. The thresholds are subject to changes for realistic trigger rates when running with data.

Chapter 3

The pixel detector

The active pixel detectors developed over the last twenty years for high energy physics are the most advanced silicon-based detectors. With 80 million pixels, ATLAS built and operates one of the largest of these detectors.

In this chapter we will mainly discuss the calibration of this detector and the first analyses done with cosmic rays. In section 3.1 a short description of the pixel detector, its data acquisition system (DAQ) and the detector control system (DCS) are presented. Detector calibration constants derived from stand-alone calibration scans are presented in section 3.2. In sections 3.2.2 and 3.2.3 an overview of the calibration data used online is presented, focusing on my work regarding the extraction of calibration constants and of the special pixel map from the module production scans. In section 3.2.4 I discuss briefly a part of my technical work related to the implementation of the offline access to the DCS information. In section 3.3 the noise study that I performed with the pixel detector is described in details. The last section is devoted to the pixel hit efficiency measurements that I performed with cosmic muon rays.

In December 2006, endcap A, representing 8% of the pixel detector, was commissioned on surface with cosmic rays. The full detector was completed in 2007 and was integrated into ATLAS. In Autumn 2008, the full ATLAS detector was commissioned in-situ with cosmic rays. However the pixel detector was not completely calibrated due to a delay in the pixel commissioning caused by a serious cooling problem. An old configuration for the pixel modules were used for data taking in September and October 2008. We will refer to this period as the 2008 run 1 cosmic period and the detector tuning used in this period will be called the old tuning. Another data taking period occurred the last week of November 2008, where only the inner detector system was switched on. New configurations from in-situ tuning were available and used. We will refer to this period as the 2008 run 2 cosmic period and the corresponding tuning as the in-situ tuning.

3.1 General description

The pixel detector should provide high precision measurements, next to the interaction point, of the charged particles produced at the LHC. The most important requirements for the pixel detector are:

- three measurements per track over a pseudo-rapidity range of $\mid \eta \mid <2.5$;

- high detection efficiency close to 100% with a low noise rate;

- intrinsic resolution of about 10 μm in R-ϕ and 115 μm in the z direction;

- transverse impact parameter resolution better than 15 μm, This is needed to separate tracks generated by long-lived particles e.g. beauty and charm hadrons;

- good reconstruction of primary and secondary vertices in both the transverse plane and the z direction;

- radiation hardness of all detector components. The first pixel layer, at 5 cm from the interaction point, will accumulate a total dose of 500 KGy after 5 years of operation;

- minimal amount of material to reduce multiple scattering and secondary interactions in front of the other ATLAS sub-detectors.

3.1.1 Layout

The pixel detector active area is divided into three main parts: the barrel that covers the central region and two endcaps for each side. A light mechanical support structure, constructed from carbon composites, supports the active parts as represented on figure 3.1. This structure also integrates the pixel cooling tubes. On both sides of the active area there is a support structure for various services, the complete object being called the pixel package. The pixel package structure contains different power lines for the detector and the different environmental sensors, optical fibres for pixel DAQ and cooling tubes. It also contains the LHC beam pipe with the corresponding support structure. The pixel detector mechanical structure is described in details in [33].

The pixel detector is made of 1744 modules of 6.08×1.64 cm^2 each. A silicon sensitive tile connected to its associated frontend electronics forms a pixel module containing 46080 individual channels or pixels. In the barrel region, 13 modules are mounted on a stave with a 1.1° tilt angle in the Z-R plane. The barrel is composed of three cylindrical layers. The staves are mounted longitudinally on a
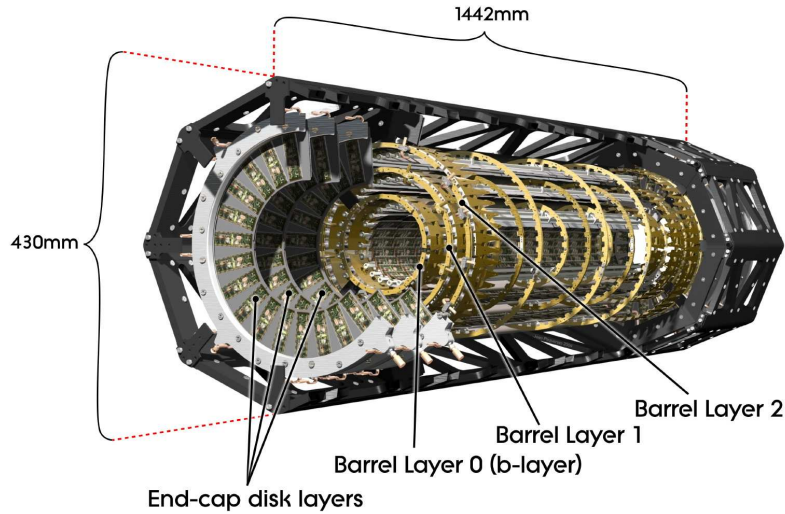
Figure 3.1: Layout of the ATLAS pixel detector [34].

cylindric support with a tilt angle of $20°$ in R-ϕ to form a layer. This geometry allows to have overlaps between neighbouring modules and therefore provides a full coverage without gaps in each of the layers. Two adjacent staves share the same cooling loops and are called a bi-stave. Therefore each cooling loop serves 26 modules in the barrel region. The position of each of the barrel layers and the numbers of corresponding staves and modules are listed in table 3.1.

Layer	Radius (mm)	Number of staves	Number of modules	Active area (m^2)
0	50.5	22	286	0.28
1	88.5	38	494	0.49
2	122.5	52	676	0.67

Table 3.1: Properties of the pixel detector barrel layers.

Each of the endcaps is formed of three disks. The disks consist of 8 sectors with six modules each. These six modules are mounted by two groups of three on each side with the long module side in the radial direction. The modules on the back side are rotated by $7.5°$ in the ϕ direction. This geometry allow an overlap between neighbouring modules on opposite sides and thus a full coverage without gaps. One cooling loop serves 2 disk sectors and thus 12 disk modules. The position of each of the disks in one endcap and the numbers of corresponding sectors and modules are listed in table 3.2.

Disk	z (mm)	Number of sectors	Number of modules	Active area (m^2)
0	495	8	48	0.0475
1	580	8	48	0.0475
2	650	8	48	0.0475

Table 3.2: Properties of the pixel detector disks for each of the endcaps.

3.1.2 Pixel detector sensor and frontend electronics

A detailed description of the pixel detector electronics and sensors can be found in [34]. A pixel detector, as any silicon detector, collects the ionisation charge deposited by a particle passing through the polarised sensor, and outputs an electrical signal. A minimum ionising particle (MIP) will deposit about 19600 e in the 256 μm-thick Si sensor. The pixel sensor is made of a n$^+$ implant on the read-out side and of a p-n junction on the back side. This configuration allows to operate the pixel detector even if it is partially depleted after type inversion of the n-bulk due to radiations. The n$^+$ implants are connected by bump-bonding to the read-out electronics. Each sensor is connected to 16 frontend chips arranged in two rows of eight chips. The 16 frontend chips are controlled by one Module Control Chip (MCC). The sensor along with the chips, the MCC, one temperature sensor and some other power cables and services form a pixel module. A schematic view of a pixel module is represented in figure 3.2.

Each pixel sensitive tile contains 47232 n$^+$ implants arranged in 144 columns and 328 rows. Most (41984) of the implants have a pitch of $400{\times}50$ μm^2 and the corresponding pixels are called normal pixels. The pixel implant area is dictated the pixel electronics size. The other implants have a pitch of $600{\times}50$ μm^2 and the corresponding pixels are called long pixels. Each frontend chip contains 2880 readout channels arranged in 18 columns and 160 rows. The columns 0 and 17 of a frontend chip are connected to the long pixels: this is required to allow some space between adjacent chips. For the same reason, the implants on rows 160-167 can't be covered by the chips: to remove any gap each of these implants are connected by a line to another pixel. These pixels with two connected sensor regions are called ganged pixels. This create an ambiguity on the position of the crossing particle if one hit is observed in one of these pixels. To help solve this ambiguity using clusters, the connection is done on every other pixel of the chip i.e. row 160 is connected to row 153, row 161 to 155 etc.. The normal (long) pixels between ganged pixels are called inter-ganged (long inter-ganged) pixels. This complex region between 4 chips in a module, with different pixel types, is represented in figure 3.3. The long, ganged and long-ganged pixels have different properties, e.g. noise level, due to their different sensor areas and therefore different capacitances.

The pixel cell electronics is represented in figure 3.4. The pixel sensor is
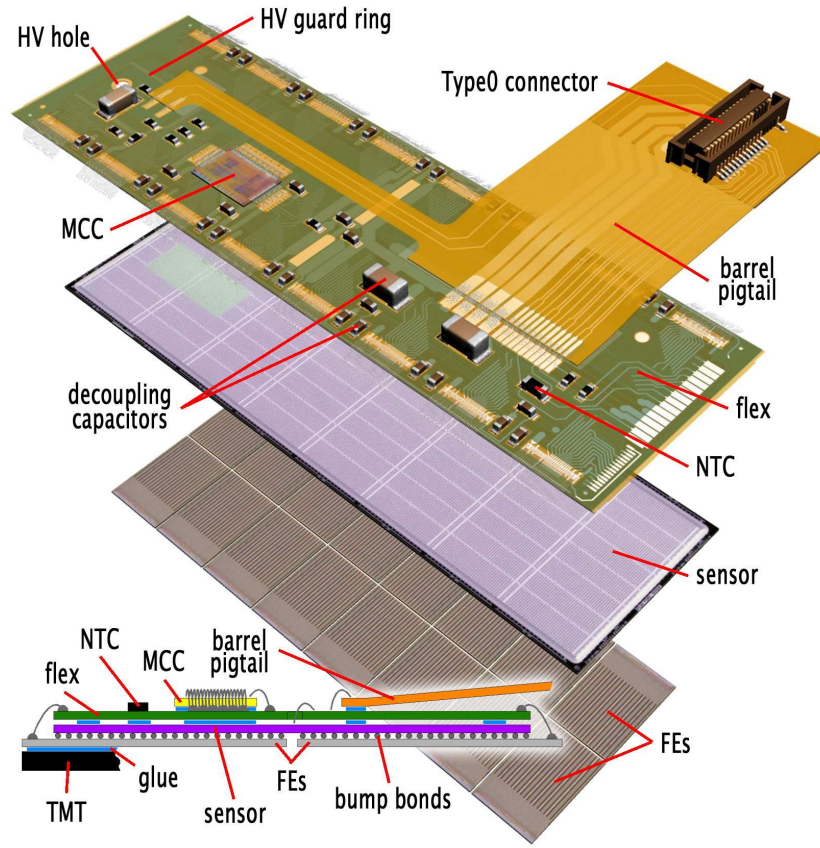
Figure 3.2: Layout of an ATLAS pixel module [34].

connected to a charge sensitive preamplifier with a 5 fF feedback capacitor. A compensating circuit is implemented to compensate for the leakage current. This circuit is also used to discharge the feedback capacitor with nearly constant current. In this way the time to discharge the capacitor is proportional to the collected charge and provides a measurement of the charge. The preamplifier is connected to a discriminator with a programmable threshold. When the deposited charge is high enough to pass the threshold, a hit is detected and temporarily stored in local memory. For each hit, three informations are stored:

- the leading edge (LE), which is the timestamp of the discriminator output passing above the threshold;

- the trailing edge (TE), which is the timestamp of the discriminator output decreasing and passing below the threshold value;
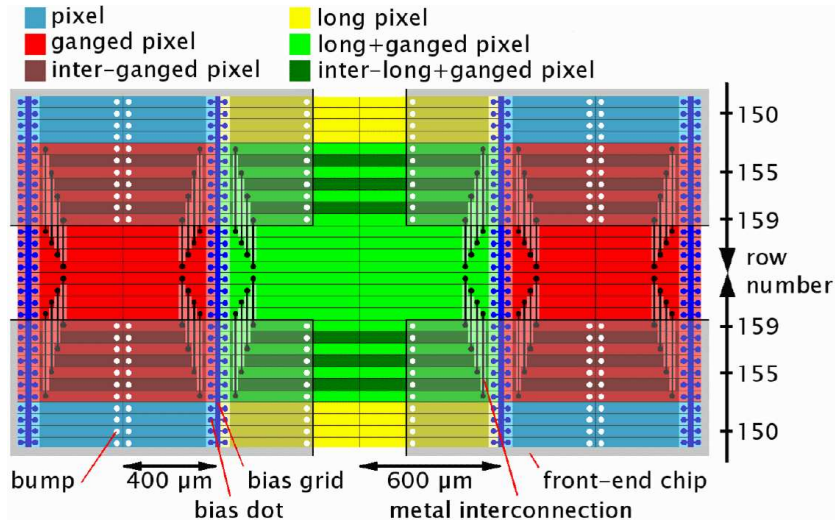
- the pixel address.

Figure 3.3: Inter-chip region showing the different types of pixels. The chips are represented by shaded regions. The white points represent the bump bonds and the black lines the connection wires for ganged pixels.

The hit information is then transfered to the hit buffers at the chip periphery. If a L1 trigger is received within 3.2 μs, corresponding to the trigger latency, the hit information is transfered to the MCC. Otherwise the hit information is cleared. The MCC will build an event using information from all chips and send it to the pixel DAQ system.

Each pixel has several Digital to Analog Converters (DACs) to tune different properties:

- FDAC: 3 bits to tune the feedback current, I_f. This is used to tune the discharge time of the feedback capacitor and thus the time over threshold (ToT) of the discriminator;

- TDAC: 7 bits to tune the discriminator threshold;

- Mask: this is used to mask the output of the discriminator;

- Select: this is used to enable charge injection into the preamplifier. The charge injection is used to tune, calibrate and simulate charge deposited for each of the pixels;

- Shutdown: used to disable the preamplifier.

In addition several bits are used to configure each of the frontend chips. The most important for our purpose is the GDACs used to tune the overall threshold on one chip and the IF DACs used to tune the overall feedback current for all
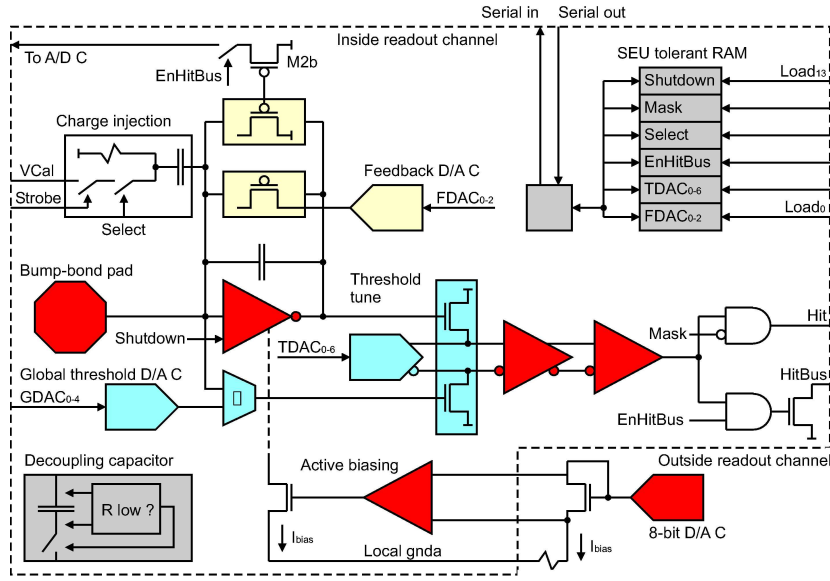
48

Figure 3.4: Diagram showing the pixel cell electronics [34].

pixels on one chip. The redundancy for tuning some quantities both at the chip and at the individual pixel levels allows to have a larger range with less precision at the chip level to tune the overall response of all corresponding pixels. A smaller range with higher precision is used for individual pixels to fine tune and reduce the dispersion for the desired quantity.

3.1.3   Overview of the pixel detector data acquisition system

A general view of the pixel detector data acquisition system (DAQ) is represented in figure 3.5. The main connection between the on-detector electronics inside AT-LAS and the off-detector electronics is done via optical links. Optical connections allow to reduce the material budget and also to avoid additional source of noise by decoupling the on-detector from the off-detector electronics. A module transfers the signal to opto-boards via differential twisted pair electrical connection. Two opto-boards, each on one side, serves a pixel stave. Therefore each opto-board is connected to a so called half-stave i.e. six or seven modules of a stave for the barrel. In the endcap regions, an opto-board is connected to six modules on one sector. The opto-boards convert the electrical signal from modules to optical signal and transfer it to the Back Of Crate (BOC) cards. The opto-boards also receive commands from the BOC and transfer them electrically to the modules. Each module uses its own optical lines: one up-link and one down-link. Down-links are used to send commands, clock, configuration and trigger to the modules. Up-links are used to send events and to read back configuration from the modules.

49

B-layer modules have two up-links to increase the readout speed in the region next to the interaction point.
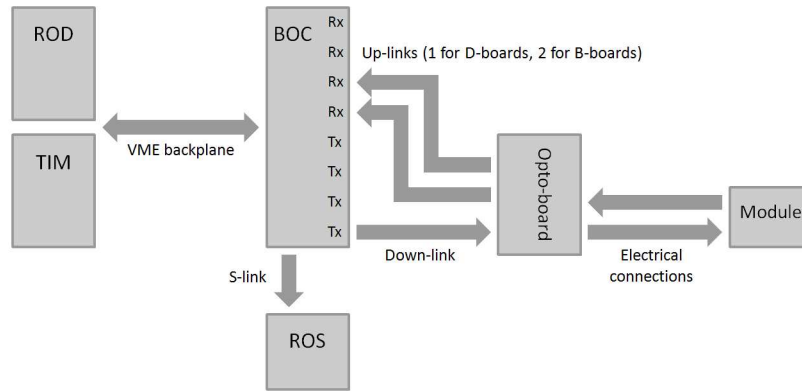

Figure 3.5: Schematic view of the pixel DAQ system showing its main components.

The BOC also acts as an optical-electrical converter. Each BOC is connected to a Read Out Driver (ROD). RODs are grouped in ROD crates that contains one Trigger, Timing and control Interface Module (TIM) and one Single Board Computer (SBC). The TIM controls the detector timing and is used as an interface with the trigger system. The SBC is a commercial computer which runs the pixel DAQ infrastructure to control and configure the pixel detector.

In data-taking mode, the ROD transfers the event to the Read Out System (ROS) without any special treatment. The ROS is a commercial PC-based system that is the interface with the ATLAS overall DAQ. In calibration mode, the amount of data is much higher and can't be transfered following the same path as for the data taking. The detector calibration data is treated directly on the RODs where histograms are filled. Different histogram manipulation, e.g. fitting, are optionally done also inside the RODs depending on the calibration scans type. The needed information is extracted afterwards via a VME-bus by the SBC to be analysed and stored. Some of the calibration information is summarised and copied to offline databases to be used in data simulation and for reconstruction. This is discussed in section 3.2.

3.1.4 Overview of the pixel detector slow-control system

The pixel Detector Control System (DCS) controls the supply voltages and environmental conditions of the pixel detector. It also includes an interlock system to protect different detector components. The pixel DCS system is represented on figure 3.6. The DCS system main components are:
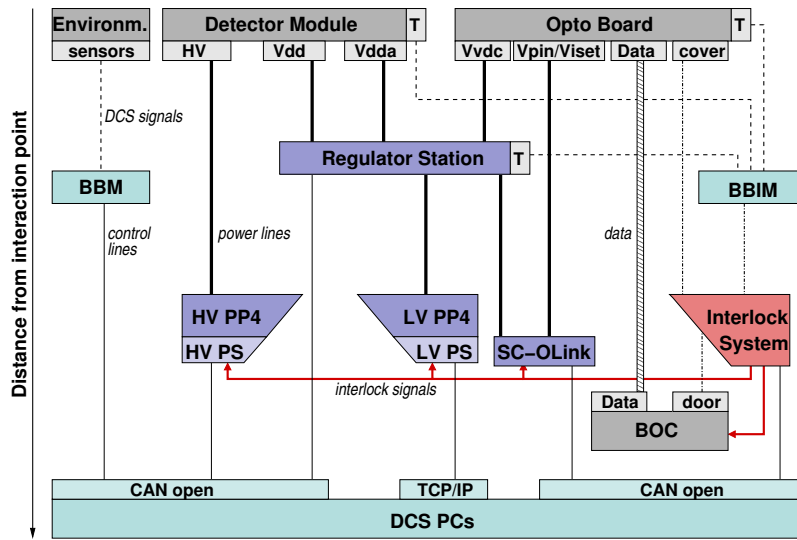
50

Figure 3.6: Schematic view of the pixel DCS system and its main components[34].

- power supplies for modules, opto-boards, temperature and humidity sensors;

- regulator boards to protect some sensitive detector electronics against transient surges. Also these regulators compensate the voltage drop over the long cables between the power supplies and the on-detector electronics;

- an interlock system divided into a hardware based and a software based system;

- commercial computers to control the hardware system and to store relevant data into databases. The DCS computers also run a Finite State Machine (FSM) algorithm that computes the state for each detector components. The FSM uses inputs from different DCS components such as voltages, current measurements and environmental sensors. It also communicates with the cooling system.

Table 3.3 summarises the module nominal operating voltages and temperatures. Some of the DCS measurements (module temperature, bias voltage) are needed for offline reconstruction. In addition the FSM flags are used offline to detect dead or malfunctioning detector components. Two flags are used to describe each pixel module:

- FSM state: describes the operation mode of the module i.e. in which operational state did the user set the module;

51

Measurement	Value	Description
V_{DDA}	1.6V	Supply voltage for the pixel analogue part
V_{DD}	2.0V	Supply voltage for the pixel digital part
HV	150V	Bias voltage for the pixel sensor
Temperature	-7°C	Module temperature

Table 3.3: Some of the DCS nominal values for a pixel module. The HV will increase to reach 600V after sensor irradiations.

- FSM status: describes the operation goodness of the module i.e. how well the module is doing what we wanted it to do.

The FSM status can be OK when the system operation is in good shape or WARN-ING, ERROR and FATAL when there are problems, depending on the severity of the problem. The status is computed using the measurements of currents, voltages and module temperature and comparing them to nominal values. Different FSM states and their description are presented in table 3.4. The ON state is reached when the module is powered, the READY state is reached when the module is configured by the DAQ system. The DCS does not know about module configuration and the READY state is determined using measurements of the analog and digital currents. These currents depend on the configuration of the module. All DCS values along with the FSM flags are stored in a PVSS database. The PVSS database is not used offline and the data should be copied to the offline databases. This is done via a process named PVSS2COOL [35]. The technical implementation of the access to DCS values for offline reconstruction is discussed in section 3.2.4.

FSM state	Description
READY	module on and configured
QUIET	module on and configured with all pixels disabled
ON	module on but not configured
OFF	module off
DISABLED	module disabled
UNKNOWN	lost communication
UNDEFINED	monitored voltage is different from set value

Table 3.4: Some of the pixel module FSM states with a short description.

3.2 Detector calibration and conditions

Several quantities should be tuned or/and calibrated at different levels for the AT-LAS pixel detector. The DAQ system and the on-detector electronics allows different type of scans. In this section we briefly discuss only three types of scans: the threshold scan, the timewalk scan and the ToT calibration scan. Also an overview of the special pixel map (SPM) used offline is presented. This map is built by combining the information from different scans and contains a list of dead, noisy and defective pixels.

All calibration constants from threshold, timewalk and ToT scans are used in the simulation of the detector response, commonly known as the digitisation. This is mandatory for a realistic description of the pixel hit efficiency, noise, charge distribution, cluster size and cluster position. The ToT constants and the SPM are also used in the reconstruction. The ToT calibration provides a measurement of the deposited charge: it is used to introduce a weighting for each pixel in a cluster before computing the cluster position. This leads to a better measurement of the particle crossing point location than a simple method based on the geometrical centre of the cluster. Special treatment for some of the pixels flagged in the SPM is applied in the reconstruction e.g. the noisy pixels are excluded at clustering level.

3.2.1 Description of calibration scans

A schema representing the discriminator input charge as a function of time is shown in figure 3.7. The time is measured in units of 25 ns corresponding to the LHC bunch crossing (BC) frequency of 40 MHz. The figure shows the leading edge (LE) and the trailing edge (TE) as well as the ToT for both a low and a high input charges. The time needed for a given charge to raise above the discriminator threshold value is called timewalk. Small charges take more time to pass the threshold and thus have larger timewalk values. The discharge happens via a constant current: the slope of the discharge curve is fixed regardless of the charge. Therefore small charges have smaller ToT values.

The threshold should be tuned at the lower possible value to maximise the hit efficiency while keeping the noise rate very low. A value near 4000 e is currently used. A large ToT implies a large dead time for the pixel and therefore a decrease of the global pixel efficiency. However the charge resolution decreases with small ToTs. This is due to the fact that the ToT is measured in units of 25 ns. Currently a mean value of 30 BCs for a deposited charge of 20 ke is used. This value was chosen using Monte-Carlo simulations. It minimises the pixel dead time while keeping the charge resolution at an adequate level for achieving a good hit location measurement inside a cluster.
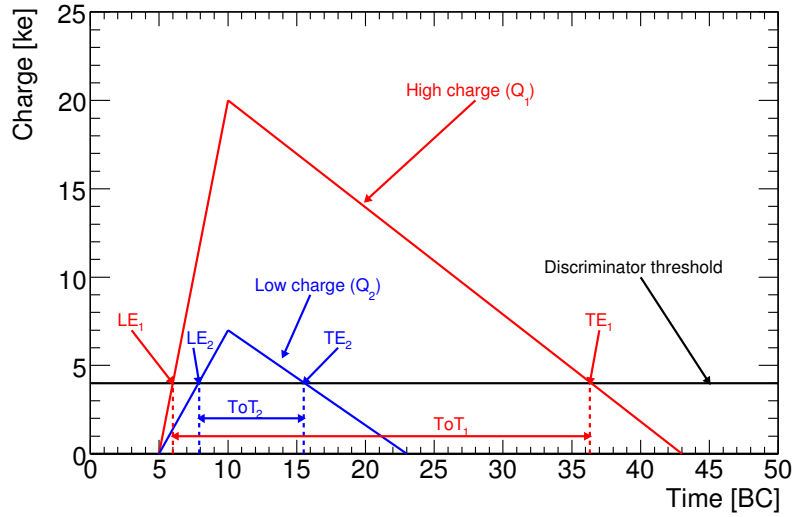
Figure 3.7: Discriminator input amplitude as a function of time for a high charge Q_1 (red solid line) and a low charge Q_2 (blue dashed line) and their corresponding ToT.

Threshold scans The pixel thresholds are first defined by tuning the chip's GDACs that set an overall threshold for all pixels in one chip. Each individual pixel threshold is then tuned more precisely to achieve the preset value and also to minimise the threshold dispersion at the chip level. This step, which sets the individual TDACs, is called the threshold tuning scan. The GDACs and TDACs can only be varied by finite steps, therefore the actual threshold will have a dispersion around the tuned value.

A threshold scan is performed to determine the actual pixel threshold and noise values. This is done by injecting, in each pixel, an increasing charge and counting the hit efficiency at each value. The resulting histogram is fitted by an S-curve that represents the integral of a Gaussian. Figure 3.8 represents an S-curve and the corresponding threshold and noise values: the threshold is defined as the charge corresponding to a 50% hit efficiency. The noise corresponds to one standard deviation: assuming a Gaussian noise distribution, this will correspond to the points at a hit efficiency of 16% and 84%.

Timewalk scan The raising time of small charges can be long and the corresponding leading edge can occur after several BCs, as shown in figure 3.7. When a L1 trigger occurs, the pixel data in a time range up to 16 BCs can be read and attached to the same event. At the beginning of data taking, several BCs will be read after each L1 (8 for the data used in this chapter). This number is known as
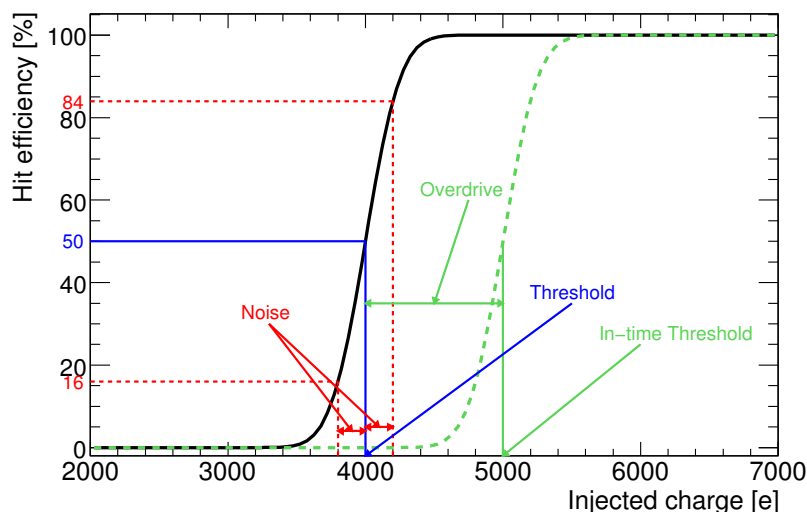
54

Figure 3.8: Schema representing the S-curve and the corresponding threshold and noise. The S-curve corresponding to the in-time threshold is also represented.

the number of Level 1 Accept (LVL1A). Increasing the number of read BCs leads to a better efficiency for low charges. But as the luminosity increases[1], reading several LVL1A will lead to overlaps between successive minimum bias events and the LVL1A should be eventually set to one. In this case low charge hits will be lost since they pass the threshold too late. An effective threshold, called the in-time threshold, is represented in figure 3.8. It is defined using the hit efficiency with a timewalk smaller than a given value. The new S-curve is shifted by a value called the overdrive, corresponding to the difference between the threshold and the in-time threshold. The S-curve shape stays unchanged and thus the noise is not affected by this shift. It should be noted that the frontend electronics can partially correct for this effect online: this is done by defining a minimal ToT value below which the corresponding hit is duplicated in the previous BC.

ToT calibration   The discharge current of the pixel preamplifier, and thus the discharge speed, is fixed by tuning the feedback current. A ToT scan is needed afterwards to calibrate the ToT response of each pixel with the corresponding collected charge. The ToT scan is done by injecting known charges into the pixel preamplifier and measuring the corresponding ToT. The injection can be done through two different capacitors: C-low and C-high. The C-low capacitor provides a more precise measurement up to 100 ke. The C-high capacitor extends the

---

[1]Increase of the number of pileup events and/or decrease of the time between two successive bunch crossings.

range to higher charges but with a worse precision for low charges. The charge as a function of the ToT is fitted by a function given by:

$$Q = A\frac{B + ToT}{E + ToT}$$

In fact the variation of the ToT with the charge is linear in most of the charge range. This function reproduces this linear behaviour while describing the non-linear region at high and low charges close to the threshold value. This function is used offline to determine from the measured ToT the deposited charge by a particle crossing the pixel sensor.

3.2.2 Calibration results

Storing all calibration values (i.e. the threshold, noise, in-time threshold and the parameters of the ToT fit function) per pixel would be very inefficient for offline simulation and reconstruction. Since the dispersion between pixels in the same chip was found to be reasonable, only the mean values and the dispersions per chip are stored for offline usage. Values for the three types of pixels, i.e.normal, long and ganged pixels, are stored separately.

In-situ calibration data were not available until recently. However old calibration scan from module production tests are available. These tests consist of the various usual scans with charge injection described above, and of additional tests with radioactive sources. The scans were used to extract the first calibration data used for offline. This was done using a private standalone code. The data from production tests were used for the first MC simulation and also for the cosmic ray data reconstruction. An official automated procedure is being implemented to update the offline databases using new calibration scans. This automated procedure was not completed at the time of writing. In addition, some scans were missing for some modules or chips in the production data. The fraction of the pixel detector with available calibration from production data for each scan is represented in table 3.5.

	Threshold scan	Intime threshold scan	ToT scan
Available data	99.7%	99.4%	98.1%

Table 3.5: Fraction of available data from the production tests for the three types of scans used for offline calibrations.

Different calibration constants from production scans are shown in figure 3.9. The pixel threshold is around 4200 e and the noise is around 190 e for normal pixels. The threshold dispersion per chip is lower than the individual pixel noise
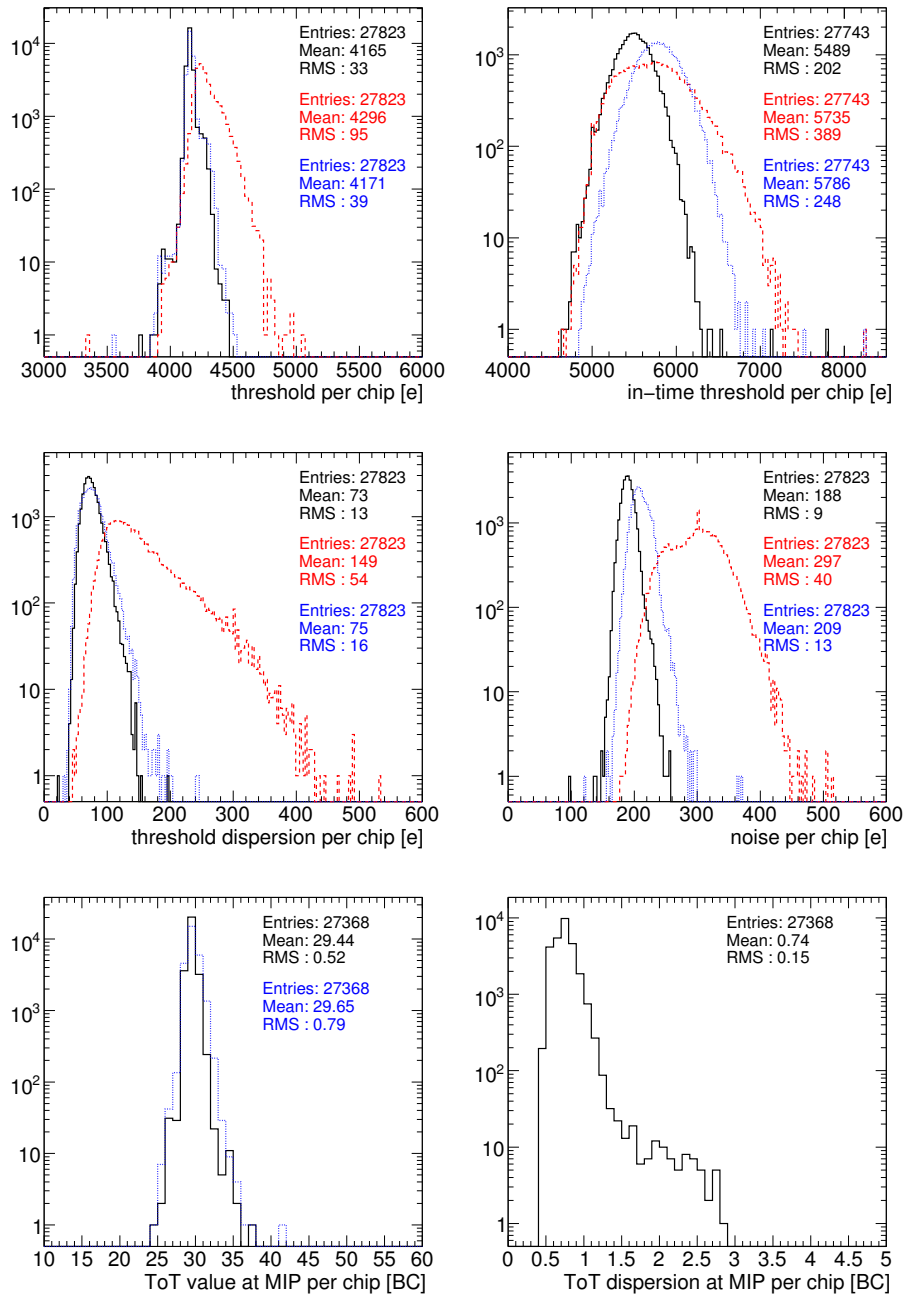
Figure 3.9: Different calibration constants extracted from the module production scans of the pixel detector. In black solid line for normal pixels, in red dashed line for long pixels and in dotted blue line for ganged pixels. For the ToT values, the long pixels are treated with the normal pixels. For ToT dispersions, all pixels are treated together.

and is around 70 e for normal pixels. This validates the choice of using a mean value per chip and not for each individual pixel. Using this procedure, the effective noise is computed by adding in quadrature the pixel noise and the threshold dispersion across the chip. The timewalk shifts the threshold by about 1300 e to be around 5500 e. The peak charge deposited by a MIP, i.e. around 19600 e, corresponds to a ToT value around 29 BCs, and a ToT dispersion of 0.7 BCs per chip. Note that the quoted dispersion represents only the dispersion between different pixels inside the chip: the ToT dispersion for one pixel, which is comparable to the former one, is not included in the plot.

For the pixel efficiency analysis (cf. 3.4), the old calibrations from production data are used. However real data reconstruction requires only the ToT calibration in order to compute the cluster charge: this is of minor importance for an efficiency study. The other constants are used only for the Monte Carlo simulations which were not studied here. For the noise studies (cf. 3.3), some new threshold scans were used to correlate the pixel occupancy with the observed noise. Two sets of scans were performed to get threshold calibrations for both periods with different detector tunings. The individual pixel thresholds and noise are represented in figures 3.10 and 3.11 respectively for the old tuning and the in-situ tuning. The discrepancy is clear between the calibrations, from module production tests (fig. 3.9), and both new calibrations corresponding to the old and the in-situ tuning. However the production calibration constants were sufficient for the very first analysis. Also this initial set of constants allowed to populate the database and to test the reliability of the offline code.

With the old tuning, the threshold data exhibits two peaks corresponding to the two sets of modules that were produced in two different sites. After applying the new in-situ tuning, the two peaks vanish and the pixel threshold distribution is centred around the tuned value of 4000 e with a much lower dispersion. However there is no significant difference between the old and the in-situ tunings for the noise distributions. All plots show some tails ($\sim 10^{-4}$ of the pixels) with higher noise values or a threshold very different from the tuned value of 4000 e. In addition a significant number of pixels have a noise value and/or a threshold equal to zero. These pixels correspond mainly to chips or modules which failed the corresponding scan. A fraction of these pixels are actually bad pixels and will be treated appropriately in the following section.

3.2.3   Special pixel map

The Special Pixel Map (SPM) contains for each defective pixel a 32 bit word describing its status. The description of the most relevant status bits is presented in table 3.6. Bit 0 is a logical OR merging several bits and defining which pixels will be excluded from the reconstruction.
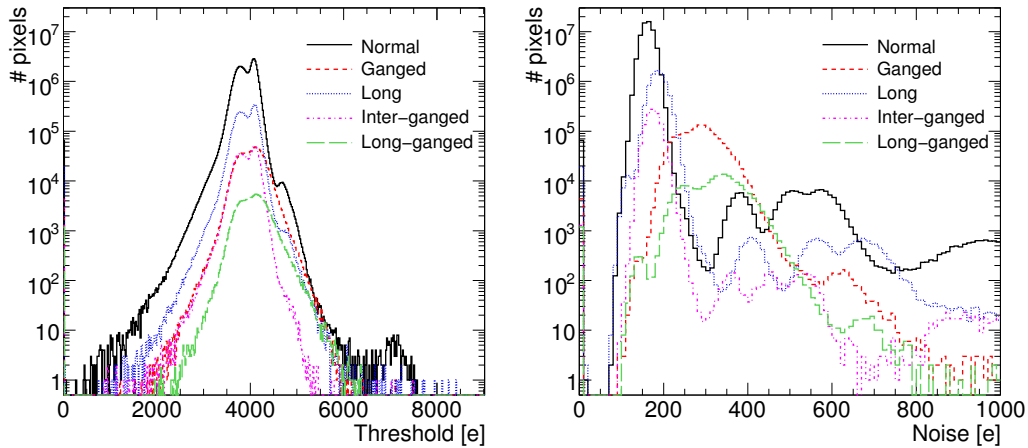
Figure 3.10: Threshold (left) and noise (right) distributions per pixel using an old tuning of the TDACs. The threshold scan used to extract these data is done in-situ. The two peaks present in the threshold distribution correspond to the two sets of modules that were produced in two different sites. The peak at zero in both distributions represents the modules, chips or individual pixels that failed the scan.
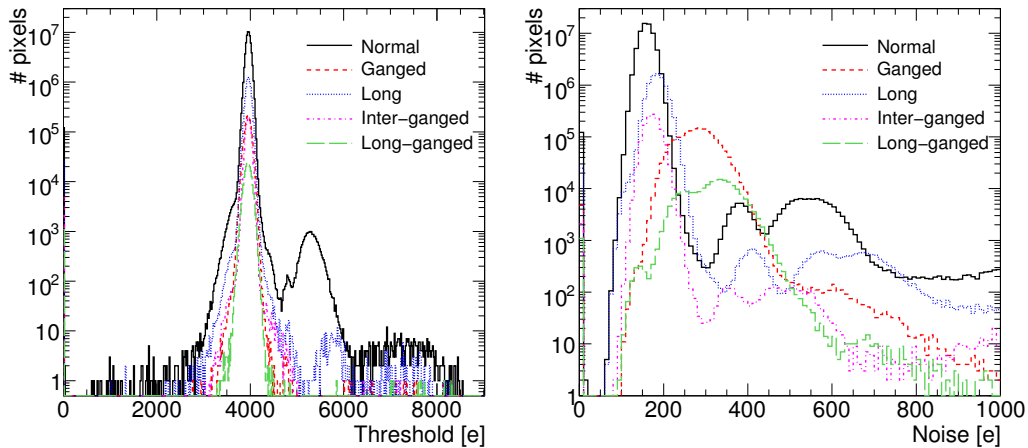

Figure 3.11: Threshold (left) and noise (right) distribution per pixel using an in-situ tuning of the TDACs. The threshold scan used to extract the data is done in-situ. The second peak in the threshold distribution, at about 5300 e, represents one bad module. The peak at zero in both distributions represents the modules, chips or individual pixels that failed the scan.

Bit	Description	How to diagnose
0	Data not useful	-
1	Masked during data taking	-
2	Masked during calibration	-
3	Bad module optical connection	Various optical scans
4	Module can't be scanned	Various scans
8	Problem in pixel digital electronics	Digital scan
9	Disconnected bump connection	Noise difference between HV-on and HV-off
10	Merged bump between neighbouring pixels	Cross-talk
11	No hit with crossing particles	Scan w/ radioactive source
12	Low efficiency with crossing particles	Scan w/ radioactive source
13	Bad S-curve χ^2 fit	Threshold scan
14	Bad χ^2 for ToT calibration fit	ToT calibration
15	High noise level	Occupancy w/ random trigger
17	Problem in pixel analog electronics	Analog scan
18	Noise/threshold high, usually noisy	Threshold scan
20	Can't tune the threshold DACs	Threshold tuning scans
21	Can't tune the ToT DACs	ToT tuning scans

Table 3.6: Bit encoding for the special pixel map including the description of each bit and the means used to diagnose the problem. Only the most relevant bits are listed.

For the moment, there is no SPM describing the complete in-situ detector status, though there is a map with only the noisy pixels. The software infrastructure to merge results from different scans and to construct the SPM is not yet ready. However different analyses were performed during module production to determine some of the special pixels. The most reliable results were extracted and added to the offline database.

Bit	Number of pixels	Fraction of pixels [‰]
1, off for data	5908	0.07
8, digitally dead	11306	0.14
9, disconnected bump	29551	0.37
10, merged bump	1437	0.02
11, dead with particles	61852	0.77
12, low efficiency	62731	0.78
13, threshold not fitted	42567	0.53
14, ToT out of spec	37257	0.46
15, noisy (residuals)	634	0.008

Table 3.7: Number of special pixels classified by SPM bit from the module production data. Only bits with available data are shown. The fraction of special pixels is computed with respect to the total number of pixels.

Detector component	Number of pixels	Fraction of pixels [‰]
B-layer	4578	0.3
Layer 1	32116	1.4
Layer 2	48029	1.5
Endcap A	5643	0.9
Endcap C	4784	0.7

Table 3.8: Breakdown of the fraction of special pixels per detector component. The modules with no available data are excluded.

There are 95150 special pixels from the production data that represent 0.12% of the total number of pixels. The number of special pixels of each type is shown in table 3.7. It should be noted that most of the noisy pixels were masked before performing the scans which lead to the production SPM: this explains the small number of noisy pixel in table 3.7. The noisy pixels are discussed in details in section 3.3. The fraction of special pixels for different layers in the barrel region and for the endcaps is mentioned in table 3.8. As expected the B-layer modules have the best performance with only 0.3‰ special pixels. Figure 3.12 shows the distribution of the fraction of special pixels in a module for different detector components.

The number of special pixels is lower than the original specification of 5%. In fact the individual pixel defects represent only a very small fraction of the pixel detector problems. Problematic modules or cooling loops can induce dead regions of a much larger area. The number of dead/disabled modules during the 2008 cosmic runs was initially varying between 70 and 130 modules. A significant number of modules were later on completely recovered and the number of problematic modules was eventually 73, corresponding to 4.2% of the total pixel detector. Thirty-six of these modules were disabled due to a leak in three cooling loops of the endcap regions. In addition, 23 individual chips suffered from various kinds of problems and were disabled, representing 0.08% of the total number of defective pixels. During 2009, more modules were recovered and the current fraction of dead/disabled modules is around 2%.
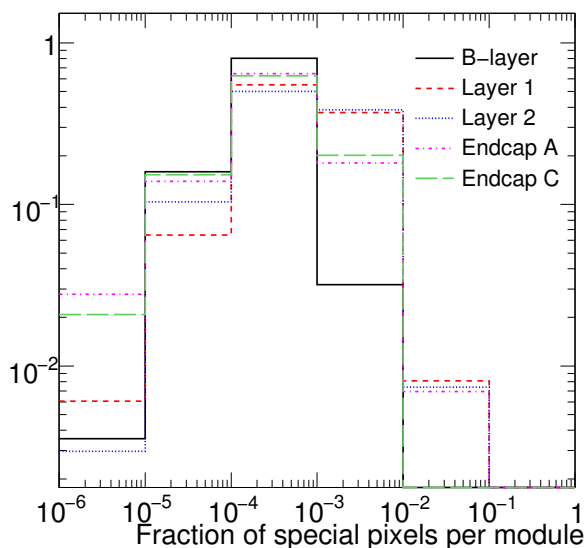

Figure 3.12: Distribution of the fraction of special pixels in the modules of the different detector components. The curves are normalised to unity.

3.2.4 Offline access to slow-control information

Several DCS informations are needed offline for both the simulation and the reconstruction. Modules temperatures and bias voltages are needed for the computations of the Lorentz angle correction and of the depletion depth. FSM state and status are needed to check if modules are enabled and correctly working. Theses values are stored by the DCS system in the PVSS online database. However, in

the ATLAS computing model, the offline code (ATHENA) should only access offline databases that are generally COOL databases [36, 37]. Therefore the PVSS information need to be replicated to the COOL databases. This is done using the PVSS2COOL process [35]. PVSS2COOL is a general tool for all sub-detectors. However each sub-detector should define the organisation of its own data in the offline databases and thus the required configuration of PVSS2COOL.

Data	Type	Deadband	Timeout
Temperature	float	2°C	24h
Bias voltage	float	1V	1h
FSM state	string	-	-
FSM status	string	-	-

Table 3.9: DCS information required for each pixel detector module.

For the pixel detector, the required information is presented in table 3.9 and the four fields correspond to four independent COOL folders. This structure is flexible, allowing to add or remove a variables simply by adding or removing a folder. Each folder contains 1744 channels corresponding to 1744 modules. A channel consist of a channel number, value name, value type, the actual values and the interval of validity [IOVSince, IOVUntil[of the DCS value. The channel number can be mapped to the module identifier used in PVSS by a script using the geometry of the detector. This mapping is unique and does not depend on the connectivity. However, one should run this script whenever the DCS connectivity changes.

The FSM state and status are stored as 255 bytes words and are copied without compression from the PVSS database. The temperature and bias voltage values are stored as floats. Currently one half-stave or one disk sector, corresponding to 6 or 7 modules, are powered by the same power supply and have therefore the same bias voltage measurement in PVSS. This will change in the future when more power supplies will be available and when the bias voltage value will increase up to 600V. To allow future compatibility, the bias voltage values are replicated for all modules using the same power supply so that the 1744 channel architecture is preserved.

It is important to keep small the size of data copied for offline usage. On one hand, this will allow PVSS2COOL to replicate data quickly enough to be available for the first offline processing[2]. On the other hand we should guarantee

---

[2]The DCS data could not directly be used for trigger algorithms. However some older bias voltage and temperature data will be used by the trigger to compute the Lorentz angle. These numbers will have to be updated whenever a significant change affecting the Lorentz angle computation occurs.

a fast offline access to the database that will be accessed frequently by different offline codes. The various DCS values stored in PVSS are updated in two cases:

- if the value changes outside a certain range. The range is commonly called the deadband;

- if a certain time passes without changes outside the deadband. This time interval is called timeout.

The timeouts are set for redundancy. The deadband reflects the accuracy desired for a certain value. Offline physics analysis are not sensitive to all small variation stored in PVSS. Some sort of data compression is needed to reduce the amount of data stored offline for performance issues. This compression is done by setting new deadbands and timeouts inside PVSS2COOL. The current deadband and timeout settings of PVSS2COOL for the pixel detector are summarised in table 3.9. The deadbands are chosen to obtain the accuracy needed for the Lorentz angle computation done in [38]. The values of the timeout were chosen, after some timing tests, to keep reasonable the database update rate.
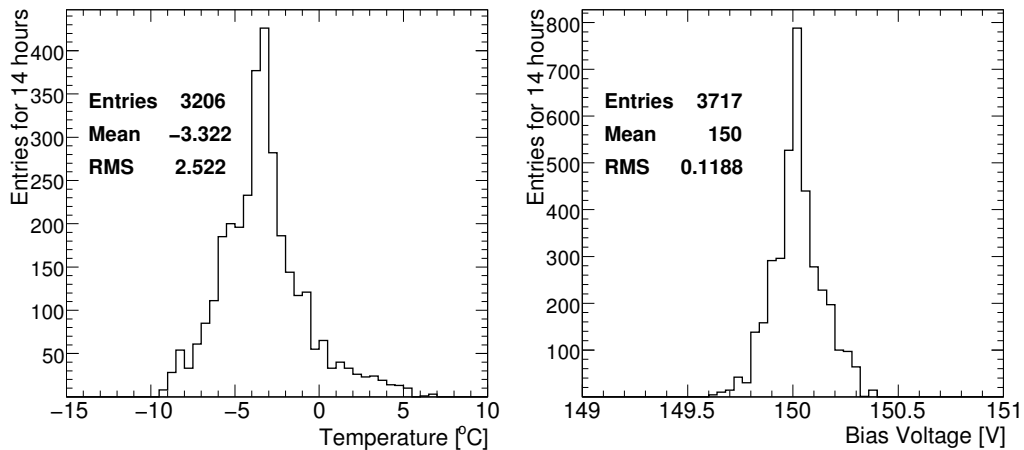

Figure 3.13: Distribution of module temperatures (left) and bias voltages (right) for a 14-hour long run.

A snapshot of the COOL database, corresponding to the temperature and the bias voltage folders for one run of about 14 hours, is represented in figure 3.13. The very small dispersion of the bias voltage values is due to the stability of the bias voltage versus time and to its consistency across different modules. The temperature for each individual module is also stable with time. The spread in temperature was found to arise from the temperature differences among the cooling loops but also from the temperature gradient for modules along a ladder (i.e.

in the same loop). About 3500 entries for each folder were recorded during this run of 14 hours. The duplicated bias voltages for modules powered by the same power supply are counted only once: they will all occur concurrently and will trigger a single database update. This corresponds to about 1 value per module per 7 hours, for each folder, which is very acceptable.

3.3   Noise measurements with the pixel detector

One of the impressive intrinsic properties of the pixel detector is the very low noise level. Most pixels will not have a single noise hit during a full run of several hours. However a very small fraction of pixels can be very noisy. It is very important to mask these pixels for several reasons:

- noisy pixels can fill up the memory buffers. This can screen other pixels in the same column pair, chip or even module and thus can reduce the efficiency;

- noisy pixels can make the pixel operation unstable especially at high trigger rate. Modules with high occupancy will not be able to cope with data rate and will start having communication problems. This can affect the data taking operation at module, ROD or even the full pixel detector levels;

- noise can also affect the reconstruction algorithms and their performance. A high number of noisy pixels can induce fake tracks or can slow-down the pattern-recognition algorithms. This can be a serious problem for the L2 trigger were online tracking is performed.

Noisy pixels can be masked online by disabling the pixel readout, or offline by discarding data from these pixels. Noisy pixels with a high occupancy should be masked online to provide a stable detector operation. After online masking, these pixels will appear as dead for the offline reconstruction. Further masking can be performed offline to remove remaining noisy pixels. Several noise analyses were done using either a part of the detector on surface or the complete detector installed in the pit. Noise determination, masking and monitoring procedures and results are presented in details in this section. It is important to define the occupancy as the number of hits per BC and per pixel. This quantity will be used throughout this section to define the noisy pixels.

3.3.1   Noise measurements on surface with a partial detector

In December 2006, a test with the pixel endcap A was performed to check the full DAQ and DCS system. Several runs with random trigger were performed

to check the pixel noise level. One of the longest runs providing 15M events was analysed. This run was taken at a 13 KHz trigger rate and reading only 1 BC (LVL1A) per event. Nineteen modules were disabled and one module was very noisy due to a HV problem. These 20 modules were excluded and only 124 modules were analysed representing 7% of the full pixel detector. The old tuning of the detector was used and all pixels were enabled. A total of 23.7M hits were recorded corresponding to an overall occupancy of $2.7 \cdot 10^{-7}$ hit per BC per pixel. The occupancy per pixel is shown in figure 3.14 both for pixels already flagged and not flagged as special in the production SPM. The noisy pixels were defined as pixels having an occupancy higher than 10^{-5}. With this definition we found 469 noisy pixels corresponding to 0.08‰ of all analysed pixels. About 89% of these pixels were already flagged as special in the SPM. If one discards offline the hits from the remaining noisy pixels, the total occupancy reaches $5 \cdot 10^{-9}$.
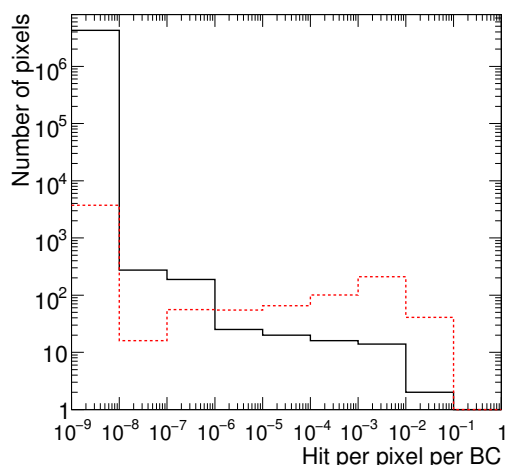

Figure 3.14: Pixel occupancy measured on surface with endcap A. Special pixels from the production SPM are shown as a red dashed line, other pixels as a solid black line.

3.3.2 Online noise masking procedure

Online masking of noisy pixels is important for a stable detector operation as stated before. The online masking procedure was first tested on a set of spare modules on surface. The setup of these modules and their services is called TOOTH-PIX. Seventy-one modules at room temperature were used to test the online noise mask procedure.

The noisy pixels are defined based on a cut on their occupancy, measured in runs with random trigger. A new module configuration with these pixels being

66

masked can then be applied. A first run with random trigger and with a large statistics was taken. Three other runs followed one week later, of which the last one used the new module configuration in order to mask online the pixels found noisy in the first run. All four runs properties are listed in table 3.10.

Table 3.11 shows the number of noisy pixels, for run 1, and the resulting occupancy after removing the noisy pixels using various occupancy cuts. Eventually it was decided to define as noisy the pixels having an occupancy $> 10^{-5}$. The total pixel detector occupancy is 10^{-10} after discarding the noisy pixels.

Sample	Trigger frequency	Number of events	Online noise mask
run 1	15kHz	130M	all enabled
run 2	15kHz	20M	all enabled
run 3	5kHz	20M	all enabled
run 4	15kHz	20M	from run 1 data

Table 3.10: Run properties used to test the online noise masking with TOOTHPIX.

Noise occupancy cut	Noisy pixels	Resulting occupancy
10^{-4}	391 (0.12‰)	1.9×10^{-9}
10^{-5}	515 (0.16‰)	1.4×10^{-10}
10^{-6}	617 (0.19‰)	1.0×10^{-11}

Table 3.11: Fraction of noisy pixels, identified in run 1, and the remaining occupancy after discarding the pixels with an occupancy higher than the cut.

Table 3.12 shows the number of noisy pixels which were in common between two runs. No significant shift like a systematic increase is present by looking at the first three runs. Comparing run 1 and run 2, which were taken one week apart in time, shows that 94% of the initial noisy pixels remained noisy, while 4% of the noisy pixels in run 2 were not noisy in run 1. This is compatible with small fluctuations around the occupancy cut. One could also notice, by comparing runs 2 and 3, that there is no shift in the noise level due to trigger rate.

Run 4 was taken after modifying the module configuration to mask the noisy pixels identified in run 1. A comparison of the pixel occupancy between these two runs is shown in figure 3.15. Twenty-seven additional pixels were found to be noisy, but most of them have actually an occupancy around the occupancy cut of 10^{-5}. The total noise occupancy for run 4 is found to be $4 \cdot 10^{-9}$ and goes down to 10^{-10} after discarding data from the 27 additional noisy pixels: this result is compatible with the one from run 1. However, two pixels with a very high occupancy ($> 10^{-3}$) in run 4 were not detected in run 1. This does not correspond to simple Gaussian fluctuations. These pixels should be masked online as they
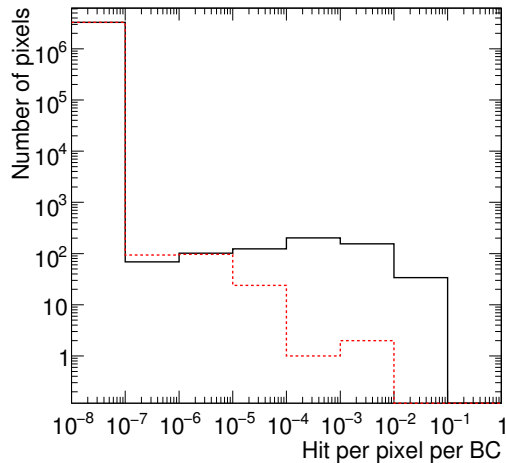
Figure 3.15: Pixel occupancy with the TOOTHPIX setup for run 1 (black solid) and for run 4 (red dashed).

can disturb the pixel operation. Therefore, the noise mask should be updated to detect these pixels. The residual noisy pixels with occupancy around 10^{-5} are not a big problem and can be masked offline.

	run 1	run 2	run 3	run 4
run 1	515	-	-	-
run 2	482	502	-	-
run 3	485	493	502	-
run 4	0	14	14	27

Table 3.12: Number of noisy pixels in common between two runs. Run 4 uses a mask defined from run 1 data.

3.3.3 Noise studies in-situ with the full detector

The in-situ noise level for the pixel detector was studied during the commissioning with cosmic rays in Autumn 2008. To reduce contamination of hits coming from the actual cosmic muons, the RPC and TGC streams, corresponding to the muon trigger chambers, were used: since the muon system volume is much larger than the pixel detector one, the fraction of muons triggered by the muon chambers and passing through the pixel detector is negligible. This makes these triggers a good approximation of a random trigger. The few runs with an actual random trigger that were taken were also used. We only selected the runs with high statistics (typically with more than 200k events for the considered stream), to be able to

compute occupancies lower than the occupancy cut at 10^{-5}. The data from all the runs were combined together, regardless of the status of the solenoid magnet (on or off) and regardless of whether only the pixel detector was taking data in a standalone mode or other ATLAS sub-detectors were taking data as well. Indeed no significant difference in the noise level was seen between these different runs. All data were taken with a pixel configuration reading 8 BCs (LVL1A) per event.
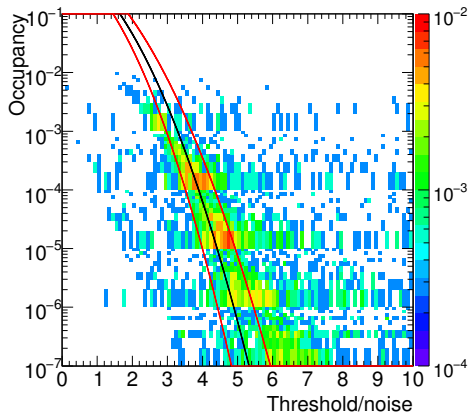

Figure 3.16: Pixel occupancy vs the pixel threshold/noise ratio. The black line defines the expected correlation for a Gaussian behaviour. The red lines define a 10% error band on the pixel threshold/noise ratio.
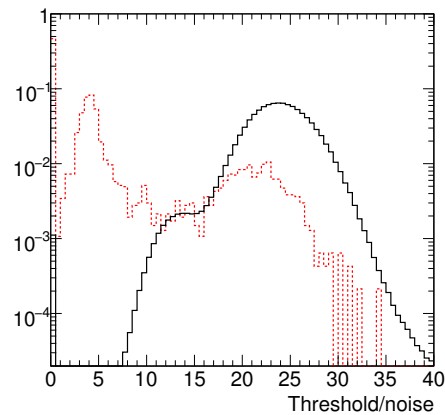
Figure 3.17: Distribution of the threshold over noise ratio for non-noisy pixels (black solid line) and for noisy pixels (dashed red line). The curves are normalised to unity.

3.3.3.1 Noise properties and noise stability

Assuming a Gaussian noise distribution, the threshold to noise ratio defines the number of hits due to noise fluctuation above the threshold and thus the occupancy. Figure 3.16 shows the distribution of the pixel occupancy vs the threshold over noise ratio. This figure was done after accumulating several runs taken within two weeks, for a total of about one million events. The threshold scan was performed in the same period of time. The black line defines the expected correlation if the noise has a Gaussian behaviour. The red lines define a 10% error band on the pixel threshold over noise ratio. Most of the pixels lie within the predicted band. One can notice a shift towards lower occupancies at low threshold over noise values. This can be explained by the fact that very noisy pixels can fill up the memory buffers and thus a saturation behaviour is seen at high occupancy. One should also note that at low occupancy ($<10^{-6}$) the error on the occupancy

is very large and the distribution is not reliable. Figure 3.17 shows the distribution of the threshold over noise ratio, for both noisy and non-noisy pixels. Seventy-nine percent of the noisy pixels have threshold over noise values below 5, while the mean value for non-noisy pixels is around 23. Also 49% of the noisy pixels have a null threshold over noise ratio, which occurs for pixels failing the threshold scan. This is expected as noisy pixels can disturb the threshold scan and make it fail.

To study the pixel noise stability, the pixel occupancy fluctuations should be monitored. We will use the occupancy pull distribution for this purpose: we define it for a given pixel as the difference in occupancy in two different samples, over the occupancy error assuming a Gaussian distribution. Figure 3.18 shows the occupancy pull computed by halving the data from the same run, separating events from the RPC and the TGC stream. The difference between these events shows a pull centred on zero and with a standard deviation of one. If we divide this run into two parts, representing the beginning and the end of the run, the central pull part is compatible with a Gaussian distribution. However some tails appear at higher pull indicating an occupancy fluctuation for some pixels higher than what is expected for a Gaussian noise. Figure 3.19 shows the same pull distribution for different runs with respectively a time separation of a few minutes and of one week. The central part shows a Gaussian noise distribution but there are very large tails at larger pull. These fluctuations are growing with the time separating the two runs. The central value of the pull distribution is however compatible with zero. This indicates that the total noise level is still the same: some pixels are becoming noisy while other noisy pixels are becoming quiet.

The occupancy mean with respect to the occupancy pull, for the last two runs separated in time by one week, is shown in figure 3.20. One can see the very large tails at high occupancy pointing to the presence of some very noisy pixels in only one of the runs. These pixels could not always be identified as noisy even if they can be particularly disturbing and exhibits in some cases cases an occupancy higher than the rest of pixel detector. The solution is to overlap several noise masks made with several iterations, to be sure that most of these pixels are detected.

3.3.3.2 Update frequency for the online noise mask

Updating the online noise mask is an important issue for a stable detector operation. One should define the frequency of this update. Online masks can be cumulated and one should also define when to reset the noise mask and restart from scratch.

Several iterations may be needed to detect all noisy pixels especially the ones lying in a noisy region. In fact a noisy pixel can fill up the memory buffers and
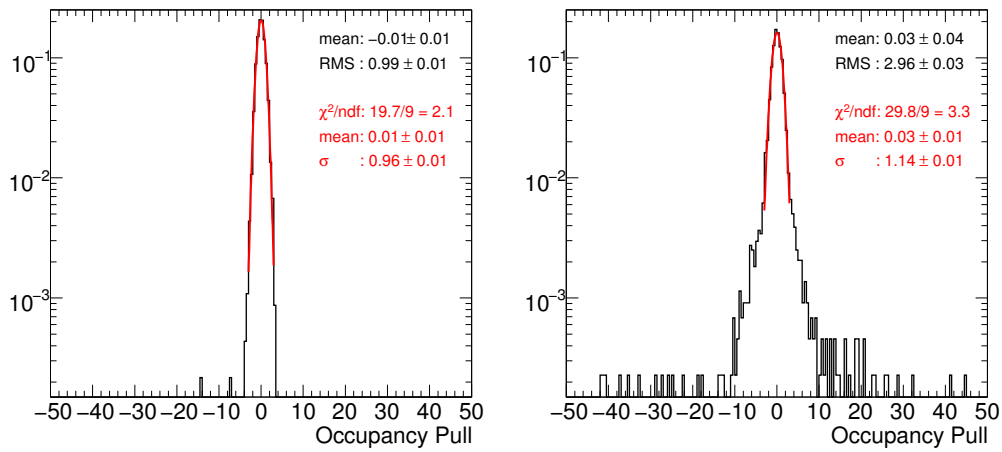
Figure 3.18: Occupancy pull for two samples in the same run. Left plot: the events are chosen randomly. Right plot: the events are divided into two samples representing the beginning and the end of the run.
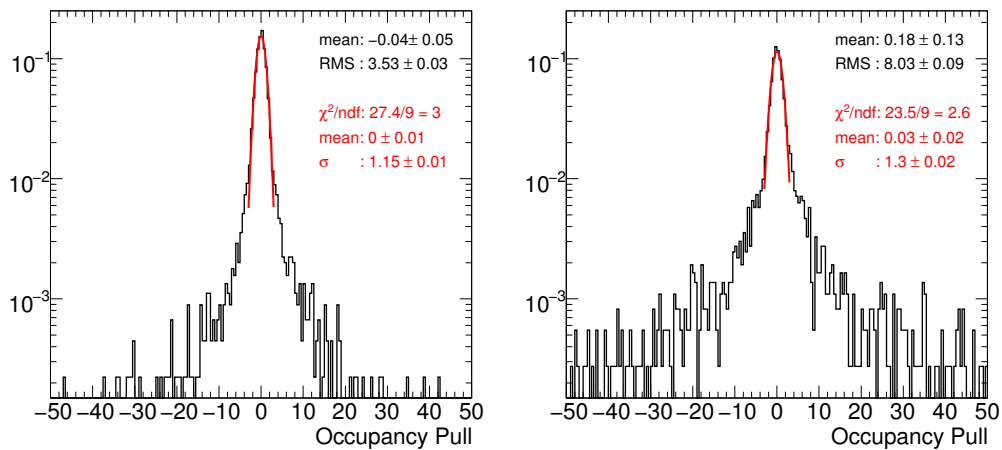

Figure 3.19: Occupancy pull for different runs separated respectively by a few minutes (left) and one week (right).
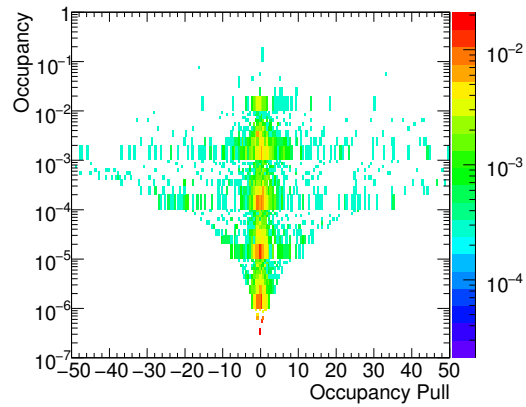
Figure 3.20: Noise occupancy versus occupancy pull. The highest fluctuations occur for pixels with high occupancy.
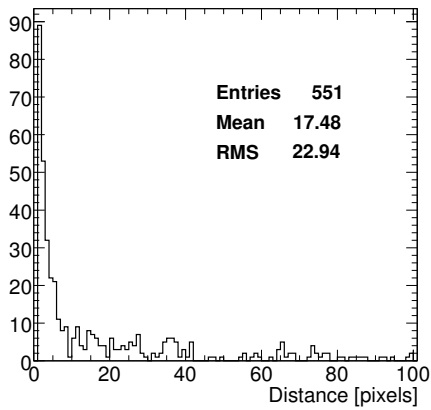

Figure 3.21: Distance in pixel units between new noisy pixels and old noisy pixels in two different runs.
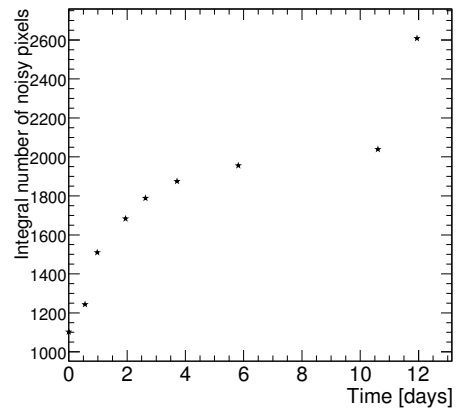

Figure 3.22: Integrated number of noisy pixels for several runs taken during 12 days. About 6000 noisy pixels were already masked online for all these runs and the y-axis only shows the remaining number of noisy pixels. The last run was taken after a cooling failure affecting the pixel detector.

screen an adjacent pixel which can be noisy as well. Figure 3.21 shows the distance (in pixel units) between new noisy pixels with respect to pixels which were noisy in an older run. Both runs were taken without an online noise mask applied. The peak at one indicates that most of the new noisy pixels appear next to previously detected noisy pixels. This screening effect can be quantified by applying an online noise mask and looking at the position of the new noisy pixels with several iterations, provided the detector conditions are stable. Unfortunately, this was not checked during the data taking period and the screening effect was not quantified. But the effect is still clear in figure 3.21 even without applying the online mask.

During the cosmic data taking, six different online masks were used. The last five were added on top of each other. This was done since the data used to produce the latest masks were taken with the previous mask already applied. One could expect that this situation will occur frequently. If the online masks are cumulated, the number of masked pixels will constantly rise and this should be controlled. To simulate this effect, several noise masks were produced for several consecutive runs and the integral number of noisy pixels is computed[3]. This is represented in figure 3.22. All runs were taken with an online mask which was already removing about 6000 noisy pixels. We can see a convergence of the total number of noisy pixels. Only the last run shows a large relative increase in the number of new noisy pixels. This run is indeed special: it was taken after a cooling failure and a power-cycling of the pixel detector involving violent thermal cycling[4]. Ignoring this last run, the study indicates that several online masks can be cumulated without a large increase in the number of masked pixels. However the online mask should be reset when the pixel conditions changes e.g. cooling failure, power-cycling. More statistics, with a more stable operation, are needed in order to define more precisely the criteria for updating and resetting the online masks, as well as the frequency at which these operations should occur.

3.3.3.3 Results after noise masking

The number of masked pixels as a function of time for both the online and the offline masks is presented in figure 3.23. All large fluctuations are understood and correspond to changes in the detector threshold tuning. The number of masked pixels is around 6000 for the first data taking period. It goes up to 12000 pixels with the in-situ tuning applied to the second data taking period. The factor 2 comes from the fact that the old threshold tuning algorithm sets some of the problematic pixels to the highest possible threshold and thus they appear as dead pixels. The

---

[3]This does not completely take into account the screening effect discussed above as the mask is not applied online.

[4]After the cooling failure the modules temperatures went down to about -40°C and then went up to room temperature.

new algorithm tries to set a lower TDAC value and can converge to the lower possible value so that these pixels appear as noisy. After online masking these pixels will be again treated as dead. This is not a big problem as these pixels will end up in a way or another in the SPM and will be excluded.
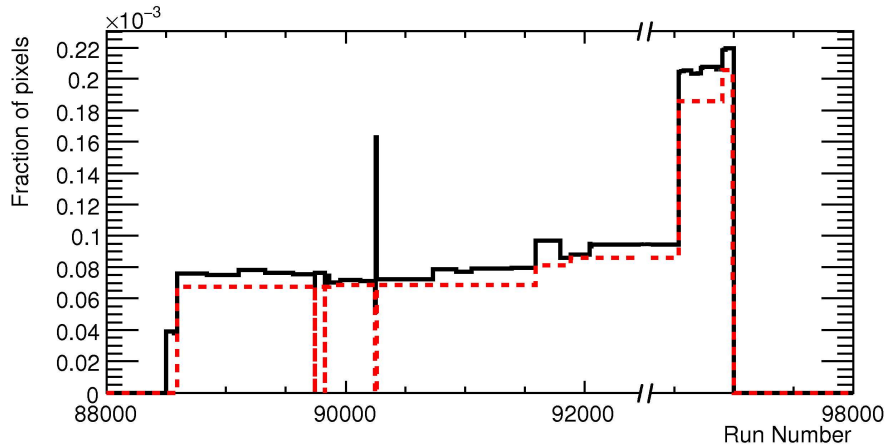

Figure 3.23: Fraction of noisy pixels vs the run number for both data taking periods. Online masked pixels are represented in red dashed line. The total number of masked pixels is in solid black line.

The total detector occupancy as a function of time after applying the offline mask is shown in figure 3.24. The occupancy is around 10^{-10} for most runs. This result is in complete agreement with the results from the TOOTHPIX test done on surface.

To illustrate the online noise masking, figure 3.25 shows the LVL1A and the ToT distributions for two runs, one with and the other without the online masking. This figure was obtained with the IDCosmic stream which requires a track in the inner detector at the L2 trigger level, in order to increase the cosmic signal in the pixel detector. The pixel data taking was reading 8 BCs after each L1 trigger. The noise hits occur at a random time and thus have a flat LVL1A distribution. However cosmic hits occur always at the same time corresponding to the delay with the trigger. Without the noise masking, it is impossible to see any peak corresponding to the cosmic signal. After applying the online mask, the cosmic signal can be seen (red curve) at raw data level before any tracking is performed. We can also see the large drop in occupancy after applying the online mask. The same effect can be seen in the cluster ToT distribution where two peaks can be seen after noise masking: the peak at high ToT (high charge) corresponds to the cosmic rays while the noise peaks at lower ToT.
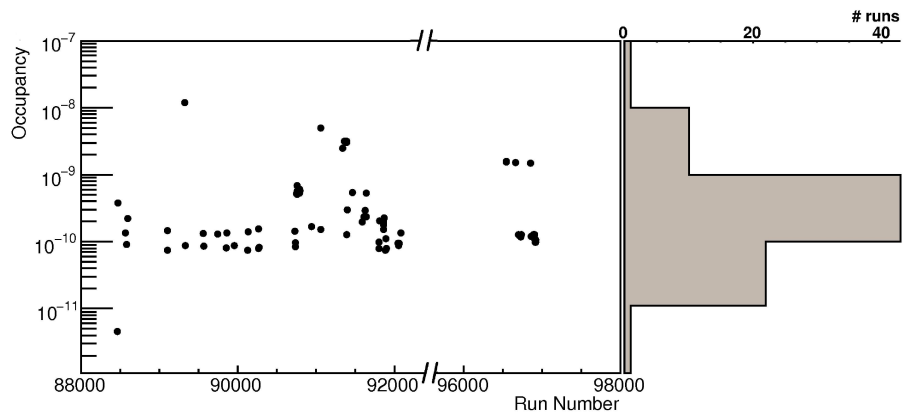
74

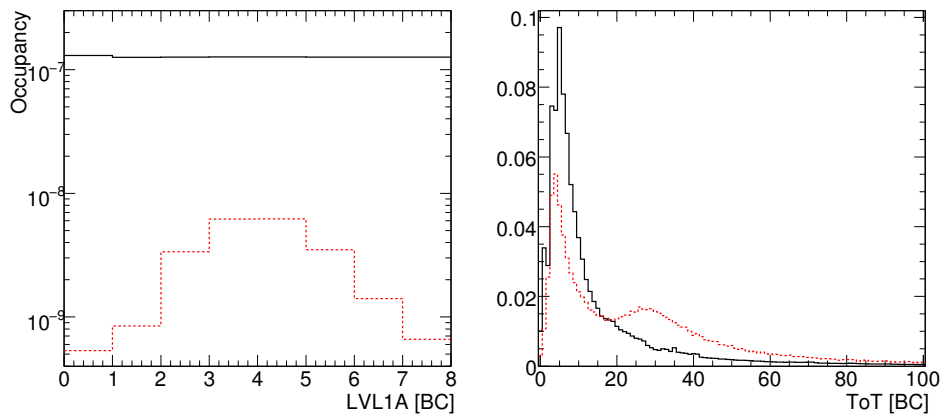Figure 3.24: Pixel detector occupancy as a function of the run number.

Figure 3.25: LVL1A (left) and ToT (right) distributions for two of the cosmic runs, for a run without a noise mask (black solid line) and for a run with a noise mask applied online (red dashed line).

3.4 Pixel hit efficiency with cosmic rays

Using cosmic muons, one can measure the expected number of track intersections with the pixel modules by extrapolating the track to the pixel measurement layers. The number of expected intersections defines the number of expected hits for the track. For a given measurement layer, if a pixel cluster was indeed attached to the track, the intersection is an actual hit. On the contrary, if no cluster is attached while the track did intersect the module, the intersection is called a hole[5]. The pixel efficiency is then defined as the ratio of the number of actual hits to the number of expected hits. This efficiency lumps together two effects: the actual pixel detector cluster efficiency and the tracking efficiency to attach a cluster to a track.

This combined efficiency represents the effective efficiency that will enter physics analysis. In the following the different effects will be deconvoluted in order to be able to quote a generic pixel cluster efficiency i.e. the efficiency of having a cluster in a "good" detector region for a crossing muon. This latter efficiency depends mostly on the charge collection in a pixel, and is expected to be close to 100% since the charge deposited by a MIP (19600 e) is much larger than the pixel threshold (4000 e). One should note that the generic cluster efficiency is not the same as the single pixel hit efficiency even if the two are related: a muon track can hit more than one pixel, especially for large incidence angles[6]. Also the charge diffusion, the Lorentz angle shift and the cross talk between pixels can lead to clusters formed by multiple pixels. Thus at η=0 for a track coming from the interaction point, only 50% of the clusters are made of only one pixel, mainly due to the chosen 20° tilt angle in R-ϕ direction. Therefore an inefficient or dead pixel does not always lead to a missing cluster.

The following studies are based on the 2008 cosmic runs. For the cosmic run 1, the IDCosmic stream is used. This stream contains data from all level 1 triggers with an additional requirement of one track in the inner detector volume at level 2 trigger. For the cosmic run 2, the TRTCosmic stream is used. This stream is based on TRT level 1 trigger. These two streams maximise the probability to have a cosmic muon passing through the pixel detector. Most of the accumulated statistics is used, corresponding to about 182×10^3 muon tracks passing the pixel detector with the solenoid on and 227×10^3 with no magnetic field. Note that all data with the solenoid on were taken using the IDCosmic stream and most data with the solenoid off were taken using the TRTCosmic stream.

---

[5]Note that the track intersections with known dead pixel modules will not be counted as holes.

[6]Note that the incidence angle is defined as the local angle formed by the track and the normal to the module surface.

3.4.1 Basic selection of tracks and clusters

A simple selection was applied to insure good quality tracks. The pixel efficiency depends strongly on this selection. We chose a selection motivated by the cuts usually applied in different physics analysis e.g. electron and b-tagging track selections. This allows us to provide a result close to what one would expect for analyses with collision data. The endcap regions are excluded from the analysis since they have low statistics with cosmic data and they are not well aligned. The disabled modules are also excluded along with the 23 chips presenting different kinds of problems. Data taken with the solenoid switched on or off are treated separately. These two samples contains tracks with very different properties and thus the tracking effects on the pixel efficiency is completely different. The tracks are required to pass the following cuts:

- number of barrel TRT hits on track ≥ 30;

- number of barrel SCT hits on track ≥ 8.

After the tracking selection, all events with multiple tracks are excluded to avoid ambiguities due to shared hits between tracks. The selection efficiency after each cut is represented in table 3.13 for both solenoid-on and solenoid-off samples. Figures 3.26 show the pixel detection efficiency as a function of the number of TRT barrel hits on track. The pixel efficiency drops for tracks with a low number of TRT hits. The drop is larger for the data with solenoid off. This is present only for the data collected with the TRTCosmic stream. Since this region is excluded by the track selection cuts we applied, no further investigation concerning this trigger bias will be discussed here.

Multiple scattering can lead to tracks that are reconstructed in only one half (upper or lower part) of the inner detector. These tracks present a bad cluster-track association efficiency. This explains the drop of the pixel efficiency, for tracks with about 8 SCT barrel hits[7], seen in figure 3.27.

For cosmic data, tracks with very high incidence angle are frequent, unlike in collisions data. In these regions the tracking algorithm can miss clusters with a relatively high probability. Furthermore, the track extrapolation to determine holes is not accurate at high incidence angle. The pixel efficiency drops at high incidence angle as seen in figure 3.28. Therefore we require that a cluster associated to a track fulfils $\sin(\alpha) < 0.7$ where α is the incidence angle between the track and the normal to the pixel sensor. This selects clusters with an incidence angle smaller than $45°$ which is more representative of what we would have from collision data.

---

[7]Note that a cosmic track passing through both the upper and the lower parts of the SCT barrel should have about 16 SCT hits.

	Number of tracks ($\times 10^3$)	
Cut	Solenoid-on data	Solenoid-off data
Total	182.3 (100%)	226.9 (100%)
TRT barrel hits	100.4 (55%)	146.0 (64%)
SCT barrel hits	82.7 (45%)	137.9 (61%)
One selected track per event	82.3 (45%)	136.4 (60%)

Table 3.13: Number of selected tracks after each selection cut. In parenthesis the cumulated efficiency.

	Number of clusters ($\times 10^3$)	
Cut	Solenoid-on	Solenoid-off data
Track selection	298.1 (100%)	498.1 (100%)
Incidence angle	193.3 (65%)	327.7 (66%)
LocalX and LocalY	148.1 (50%)	251.8 (51%)

Table 3.14: Number of selected clusters after each selection cut. In parentheses the cumulated efficiency.

Finally, some regions of the pixel modules are also excluded. Ganged-pixel regions can present clusters with ambiguous position since two pixel diodes are connected to one pixel readout. This can be partially recovered within the clustering and the tracking algorithms, but the ganged-pixel regions are excluded to remove any dependence on these ambiguity solving algorithms. This is obtained by requiring |LocalX|> 0.6. |LocalX| represents the distance to the module centre along the ϕ direction. In the ganged-pixel region, the pixel efficiency slightly drops as shown in figure 3.29.

In addition, the track extrapolation to detect holes was found to be inefficient, especially for badly reconstructed tracks, at the module edges: the number of holes can be underestimated. The underestimation of the number of holes is clear, for the solenoid-off data, at the module edges as shown in figures 3.29 and 3.30. However, the opposite effect can be seen for the solenoid-on data. In fact, the track quality in the solenoid-on data sample is better than in the solenoid-off data sample (cf. 3.4.6). Therefore the underestimation of holes next to module edge is larger for solenoid-off data. For the solenoid-on data, this effect is hidden by the cluster-on-track inefficiency that is larger at module edges. To remove these tracking effects, the region within 1 mm of the module edges are excluded: |LocalX|<7.2 mm and |LocalY|<29.2 mm. |LocalY| represents the distance to the module centre along the z direction. Table 3.14 shows the cumulated efficiency for different selections cuts.
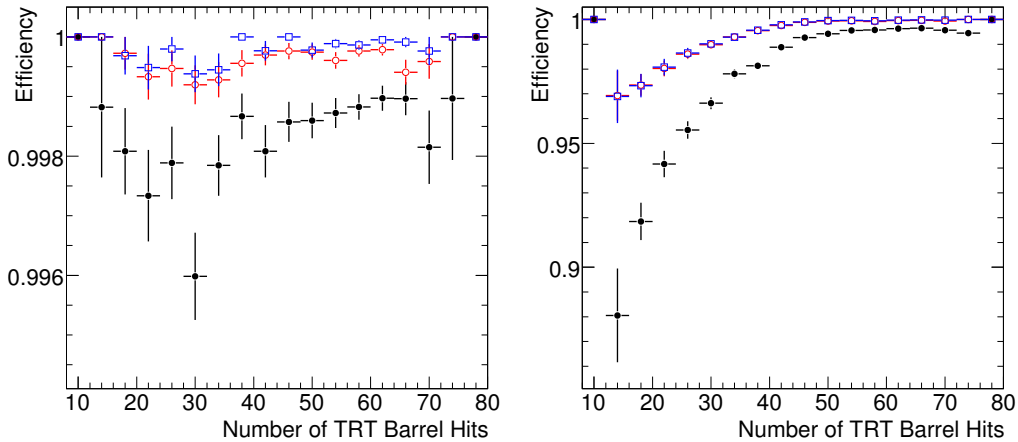
Figure 3.26: Pixel detection efficiency as a function of the number of TRT barrel hits on track with the solenoid magnet on (left) and off (right). The estimated efficiency is shown after the basic selection (cf. 3.4.1) in black solid circles, after the cluster association correction (cf. 3.4.3) in open red circles, and after an additional correction to avoid problematic pixels (cf. 3.4.4) in open blue squares. Note the different *y*-axis scales used for the two plots.

3.4.2 Underestimation of the number of holes

The pixel detector hits, together with the SCT hits, are used by the track finding algorithm. This might introduce a bias to the pixel efficiency measurement. In fact, a pixel inefficiency or more likely several pixel inefficiencies on the same muon track can lead to loose the track i.e. the track finding algorithm might be more efficient for muon tracks with less holes. Another effect that can also lead to an underestimation of the number of holes is the accuracy of tracking extrapolation. In order to quantify these two effects, one can artificially create inefficiencies in the pixel detector and check the number of holes. To do that, we perform a special reconstruction after excluding all clusters on layer 1, for one of the runs. We expect that the number of holes on layer 1 for this special reconstruction should be equal to the sum of the number of hits and number of holes for the normal reconstruction.

Figure 3.31 shows the ratio of the number of expected holes to the number of holes (N_{EH}/N_H) for layer one modules as a function of the incidence angle and of the local position in the module. N_{EH}/N_H is compatible with one for low-incidence angles but one can clearly see that we are missing holes at high-incidence angles. The selection cut at $\sin(\alpha)<0.7$, that is used in the selection will remove this effect. Also it is clear from the localX and localY distributions
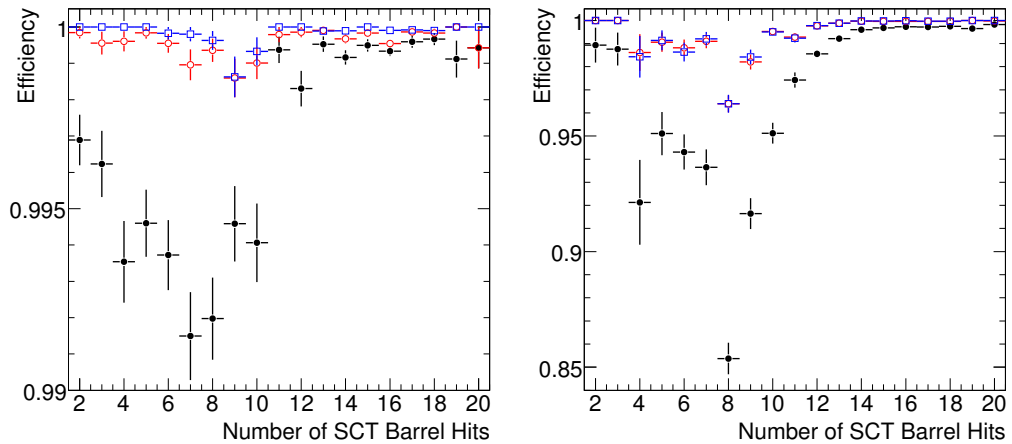
Figure 3.27: Pixel detection efficiency as a function of the number of SCT barrel hits on track with the solenoid magnet on (left) and off (right). The estimated efficiency is shown after the basic selection (cf. 3.4.1) in black solid circles, after the cluster association correction (cf. 3.4.3) in open red circles, and after an additional correction to avoid problematic pixels (cf. 3.4.4) in open blue squares. Note the different *y*-axis scales used for the two plots.
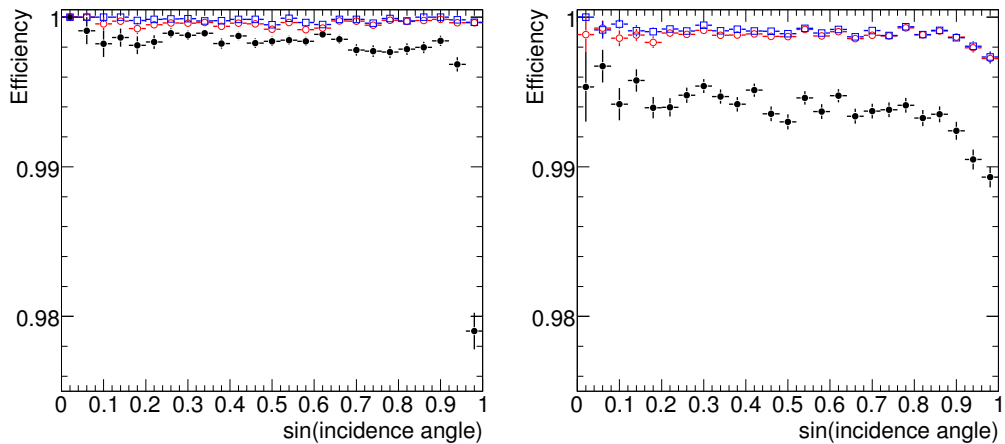

Figure 3.28: Pixel detection efficiency as a function of the sinus of the incidence angle, $\sin\alpha$, with the solenoid magnet on (left) and off (right). The estimated efficiency is shown after the basic selection (cf. 3.4.1) in black solid circles, after the cluster association correction (cf. 3.4.3) in open red circles, and after an additional correction to avoid problematic pixels (cf. 3.4.4) in open blue squares.

Figure 3.29: Pixel detection efficiency as a function of the distance in the local ϕ direction (local x) from the centre of the sensor with the solenoid magnet on (left) and off (right). The estimated efficiency is shown after the basic selection (cf. 3.4.1) in black solid circles, after the cluster association correction (cf. 3.4.3) in open red circles, and after an additional correction to avoid problematic pixels (cf. 3.4.4) in open blue squares.
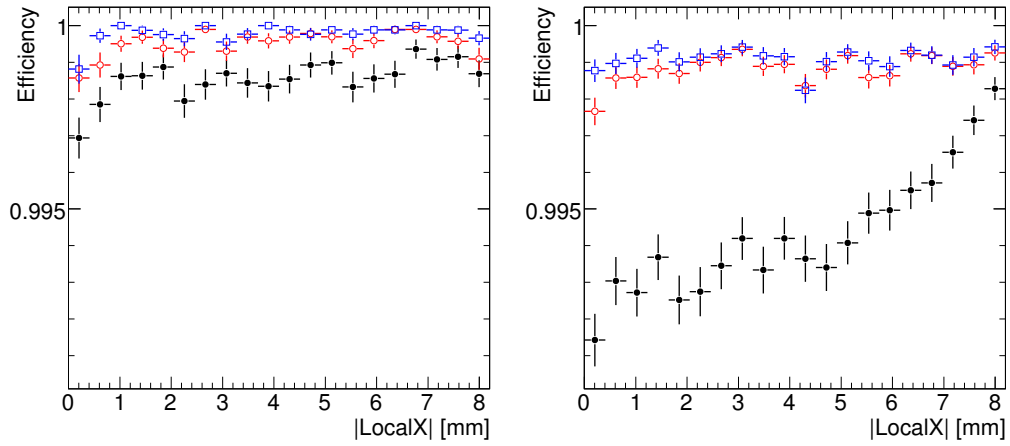

Figure 3.30: Pixel detection efficiency as a function of the distance in the z direction (local y) from the centre of the sensor with the solenoid magnet on (left) and off (right). The estimated efficiency is shown after the basic selection (cf. 3.4.1) in black solid circles, after the cluster association correction (cf. 3.4.3) in open red circles, and after an additional correction to avoid problematic pixels (cf. 3.4.4) in open blue squares.
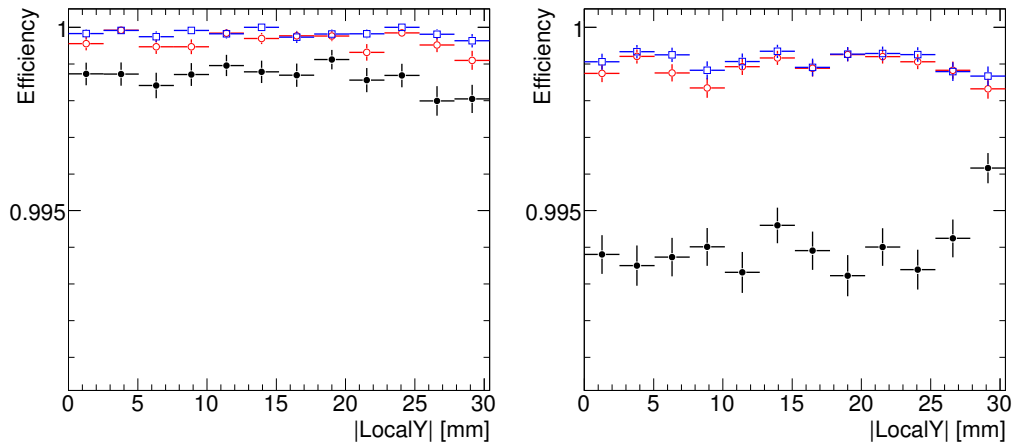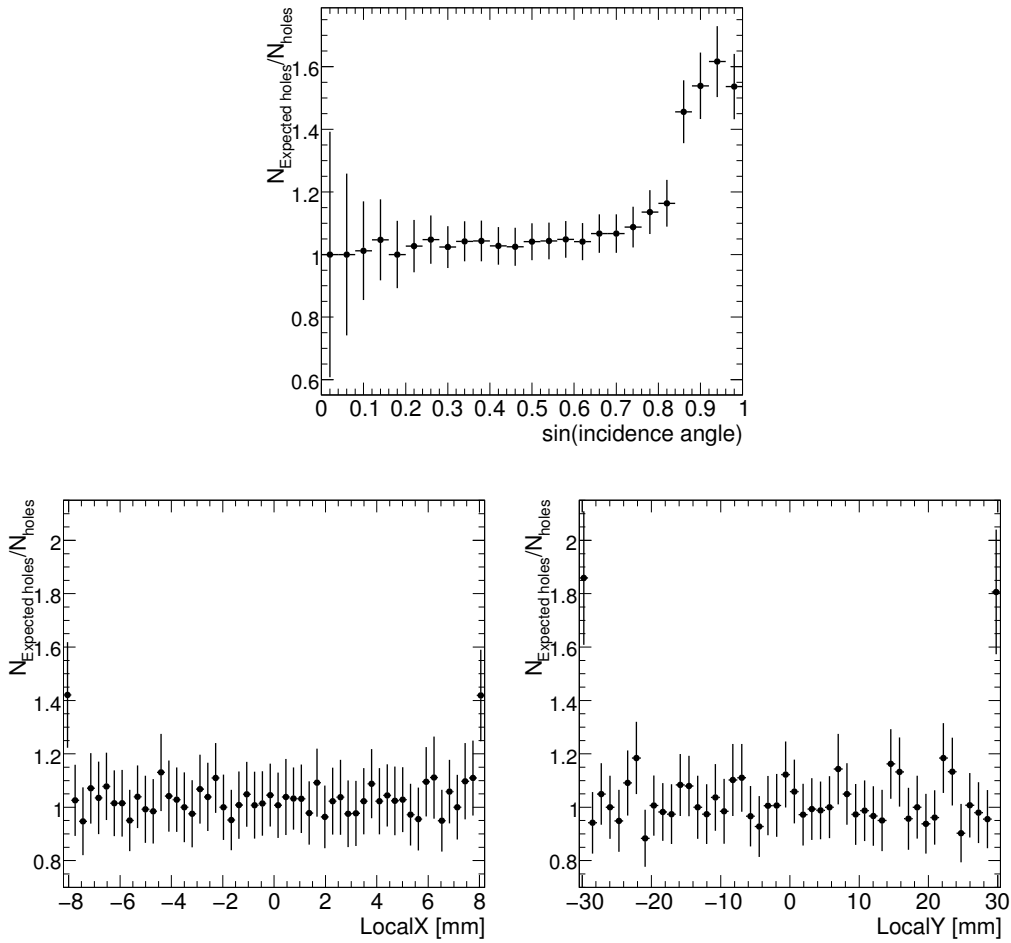
81

Figure 3.31: The number of expected holes over the number of holes, for the special reconstruction with layer one modules artificially disabled, vs the incidence angle (top plot), localX position (bottom left) and localY position (bottom right).

that we are missing holes at the module edges. This is also removed by the selection we applied in section 3.4.1.

N_{EH}/N_H is also shown as a function of the number of SCT barrel hits and of the track p_T in figure 3.32. Before the incidence angle and the module local position selections, the number of holes is underestimated especially for tracks at low p_T and with a low number of SCT hits. This is expected since these tracks have in general larger errors: the extrapolation performs worse at high-incidence and at module edges. However these distributions become flat and compatible with 1 after the full selection is applied. This is also shown in table 3.15 were we quote the underestimation of the number of holes after each cluster selection
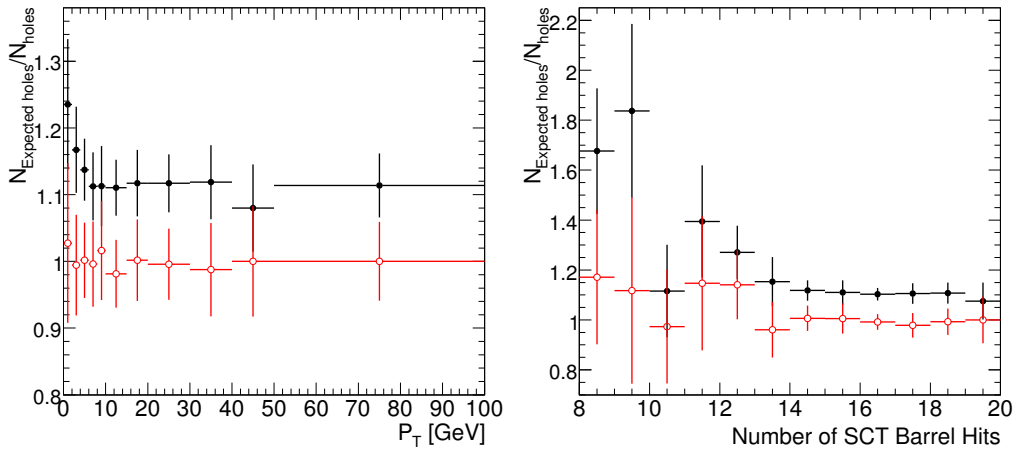
Figure 3.32: The number of expected holes over the number of holes vs the track p_T (left) and the number of SCT barrel hits (right) after the track selection cuts (black points) and after the incidence angle and the local module position cuts (open red circles).

Selection	$(N_{EH}-N_H)/N_H$ (%)
Track selection	12 ± 1.5
Incidence angle cut	3.9 ± 1.7
LocalX and LocalY cuts	-0.1 ± 1.8

Table 3.15: Underestimation of the number of holes on layer 1, due to tracking, after different selection cuts.

cut. We conclude that the number of holes is not underestimated for the selected sample and no further correction is needed.

3.4.3   Inefficiency due to cluster-track association

To be able to check if the detected holes are due to a true detector inefficiency or due to a cluster-track association inefficiency, we look for unassociated clusters in the vicinity of holes. We find that in 80% of the cases in which a hole has been detected in a module, there is a cluster in the same module but this cluster is not associated to the track. By comparison, about 0.2% of randomly generated holes (randomly selecting a position in a pixel module) have a cluster in the same module. The distance between a hole and the closest unassociated cluster in the same module is shown in Fig. 3.33. For the randomly generated holes the distribution is relatively flat as expected. However, one can clearly see the correlation between

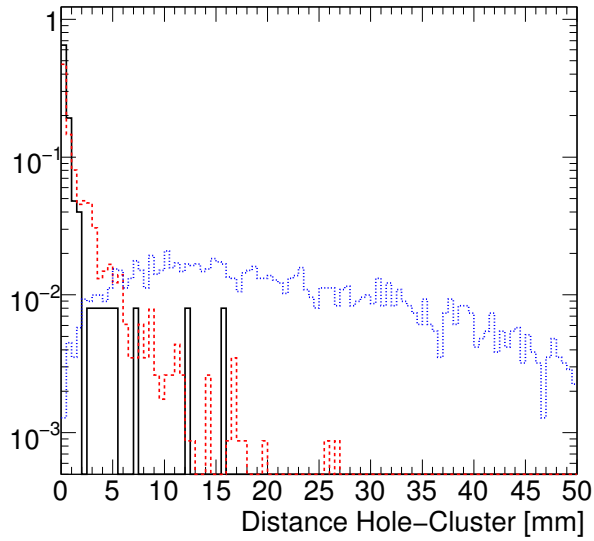Figure 3.33: Local distance (in the module plane) between a hole and the closest cluster for solenoid-on data (solid black line), solenoid-off data (dashed red line) and for a random position of holes (blue dots).
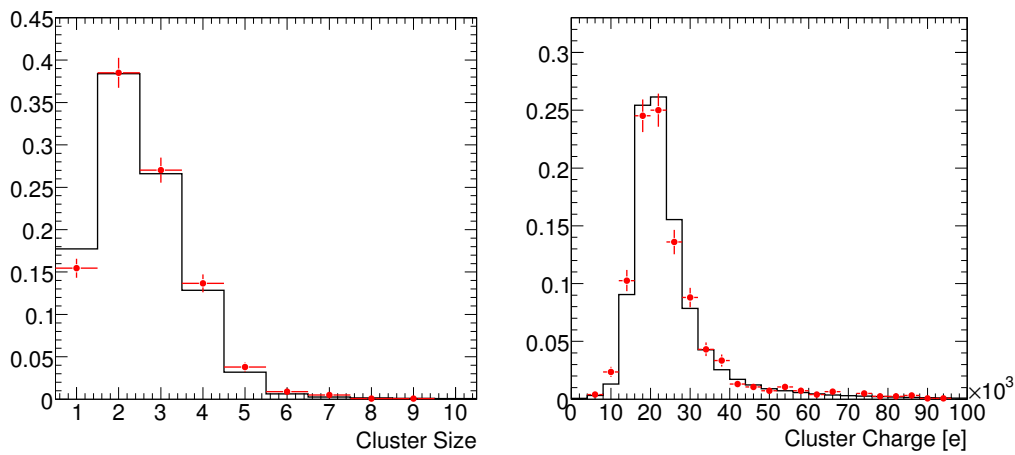

Figure 3.34: The size in pixel units (left) and collected charge (right) for clusters associated with tracks (black histogram) and for unassociated clusters which are close to holes (red points).
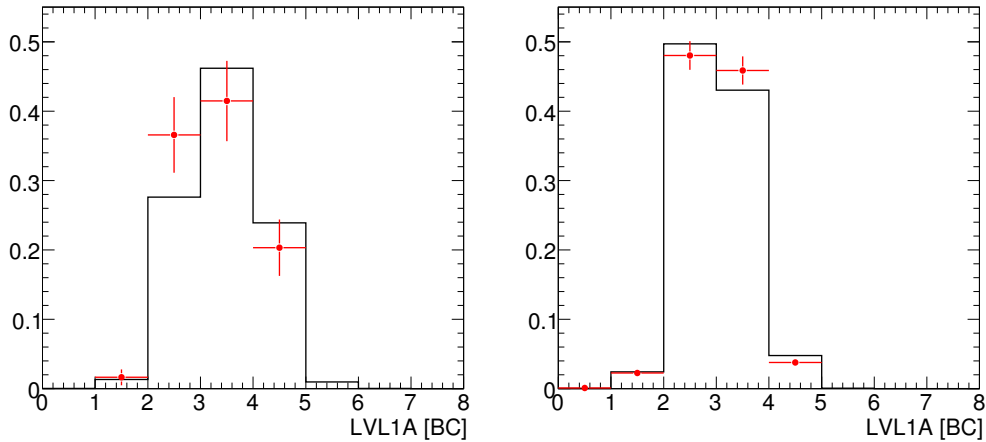
84

Figure 3.35: The LVL1A distribution for solenoid-on data (left) and solenoid-off data (right). Clusters associated with tracks are shown as black histogram, and unassociated clusters next to holes are shown as red points.

the identified holes and their closest clusters, both for solenoid-on and solenoid-off samples. The properties of clusters close to holes within a distance of 10 mm are compared to those of clusters associated with tracks in figures 3.34 and 3.35. The size, charge, and time distributions of the clusters next to holes are all very consistent with those of regular clusters associated to tracks. We conclude that these clusters are true clusters, not generated by noise. This is consistent with the very low noise occupancy computed in section 3.3. To remove this inefficiency due to cluster association to tracks, the clusters within 10 mm to a hole are re-associated to the tracks and therefore the holes are removed. The efficiency as a function of the different selection variables is shown in figures 3.26-3.30 (red open circles) after applying this correction. The distributions are now much flatter since this correction suppresses the dependence on poorly reconstructed tracks.

3.4.4 Inefficiencies and biases due to problematic pixels

A non-functioning pixel can mimic a hole, especially for tracks almost with a low incidence angle (close to normal incidence) for which the cluster size is generally one. The production SPM described in section 3.2.3 is used to determine the problematic pixels. One should note that this map was relatively old and may not describe perfectly the in-situ detector status at the moment of data taking.

The tracking local resolution in the pixel modules, for the considered samples, is about 24 μm in R-ϕ and 130 μm in the z-direction [39]. The resolution is much smaller than the pixel pitch, however the presence of some tails makes it difficult
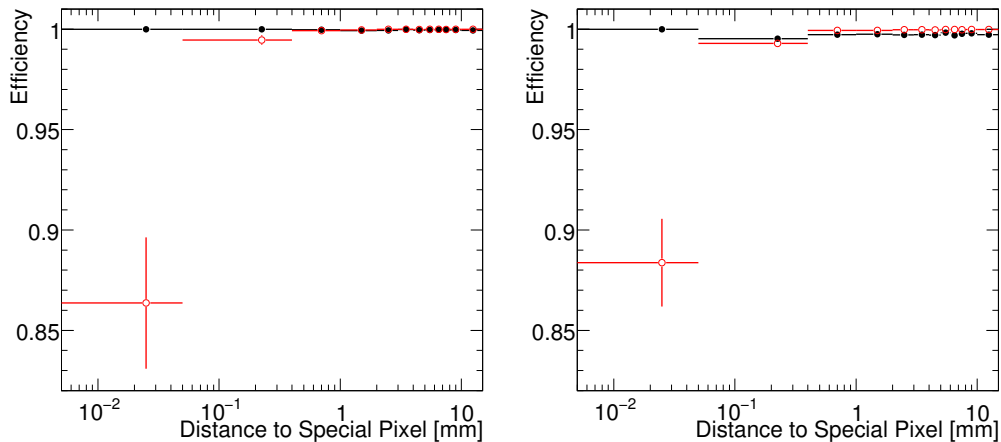
Figure 3.36: Pixel cluster detection efficiency as a function of its distance to the closest non-functioning pixel, for data with the solenoid magnet on (left) and data with the magnet off (right). The holes are separated into two categories: holes near a cluster not associated to a track (solid black circles), and holes with no nearby cluster (open red circles).

to identify the exact pixel crossed by a muon. One can not simply exclude tracks crossing a problematic pixel as done for chips and modules. The solution is to exclude the holes near the problematic pixels. The pixel detection efficiency as a function of the distance between a hole and the nearest problematic pixel is shown in Fig. 3.36. For holes with no nearby clusters we can clearly see a large drop close to problematic pixels. The efficiency is also plotted when considering only the holes near a cluster, as explained in section 3.4.3. The efficiency is flat for these holes, which further motivates the cluster association correction.

To remove the efficiency due to non-functioning pixels we exclude both holes and clusters within 2 mm of known problematic pixels. As expected this correction does not depend on the tracking properties and does not change the efficiency shape versus the selection variables as shown in figures 3.26-3.30 (open blue squares).

3.4.5 Summary of tracking-dependent efficiency and various corrections

Table 3.16 shows the average detection efficiency for the pixel barrel before and after applying the corrections previously described. The inefficiency due to unattached clusters dominates the total inefficiency. The agreement is much better between the solenoid-on and solenoid-off samples after correcting for this inefficiency. The
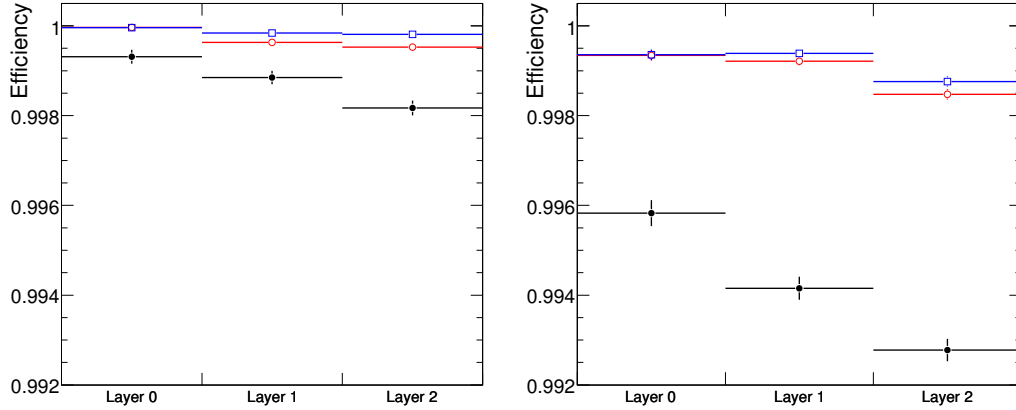
Figure 3.37: Pixel detection efficiency as a function of barrel layer, with the solenoid magnet on (left) and off (right). The estimated efficiency is shown after the basic selection (cf. 3.4.1) in black solid circles, after the cluster association correction (cf. 3.4.3) in open red circles, and after an additional correction to avoid problematic pixels (cf. 3.4.4) in open blue squares.

Figure 3.38: Average detection efficiency, after correcting for cluster association and non-functioning pixels, for the pixel barrel as a function of run for the first (left) and second (right) run periods. Efficiencies are shown for data recorded with the solenoid on (solid black markers) and off (open red markers). Runs with at least 1000 expected pixel hits are selected.

Selection level	Solenoid On [%]	Solenoid Off [%]
Basic Track and Cluster Selection	99.863 ± 0.009	99.386 ± 0.016
+Cluster-Association Correction	99.965 ± 0.005	99.890 ± 0.007
+Avoiding problematic pixels	99.985 ± 0.003	99.910 ± 0.006

Table 3.16: Average pixel detection efficiency for the pixel barrel with residual tracking biases still present.

correction due to non-functioning pixels is compatible between solenoid-on and solenoid-off data, as expected. Overall the solenoid-off sample has a lower efficiency. This is due to residual inefficiencies from tracking and will be treated in more details in the next section. The efficiency per barrel layer is represented in figure 3.37. The b-layer has clearly the best performance before corrections. This is expected as the tracks passing through the b-layer have a larger number of pixel hits and therefore they are generally better reconstructed. Furthermore the b-layer modules have a relative low fraction of problematic pixels. After applying the corrections we have a good agreement between layers. No systematic shift for the efficiency value as a function of time is detected, as shown in figure 3.38. This figure also shows no correlation with the threshold tuning done before the second period of data taking.

3.4.6 Cluster intrinsic efficiency

The cluster intrinsic efficiency does not depend on the track reconstruction. This efficiency should be flat as a function of the different track properties. The efficiency versus the number of SCT, TRT hits as well as the number of expected pixel hits is shown respectively in figures 3.26, 3.27 and 3.39. These distributions are not completely flat even after all the corrections. Several other properties were checked. Figure 3.40 shows the efficiency as a function of the track transverse momentum p_T for the solenoid-on sample. The efficiency decreases at lower p_T because of multiple scattering. This effect is not completely recovered after the cluster-association correction. The number of holes per track is shown in figure 3.41. The probability of having n holes on a track is proportional to ε_h^n where ε_h is the probability of the presence of a hole in a track. In view of the high pixel efficiency, ε_h is very small and the probability to have more than one hole on a track is totally negligible. A toy Monte-Carlo, taking into account ε_h and the multiplicity of the intersections between tracks and pixels gave zero track with multiple holes for the statistics used in this analysis. Therefore the presence of tracks with multiple holes indicates that some correlations between the holes may be due to the tracking reconstruction algorithm itself.

All considered residual tracking effects (inefficiency at low-p_T and at low
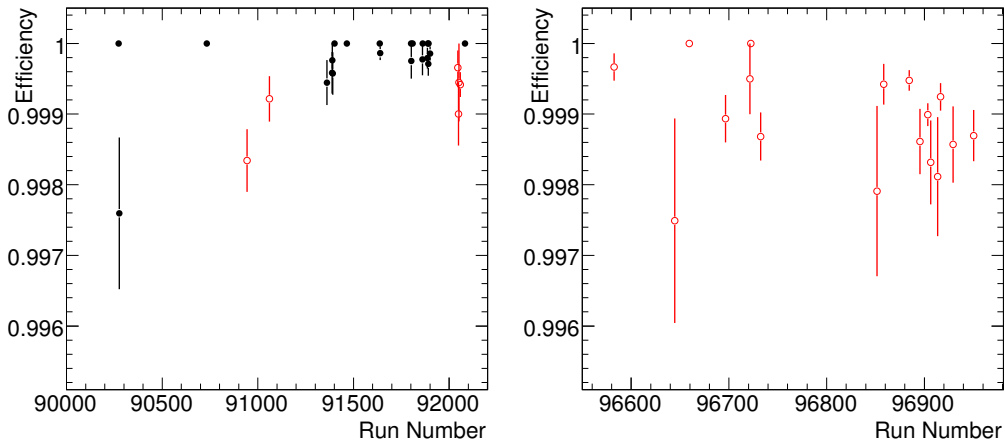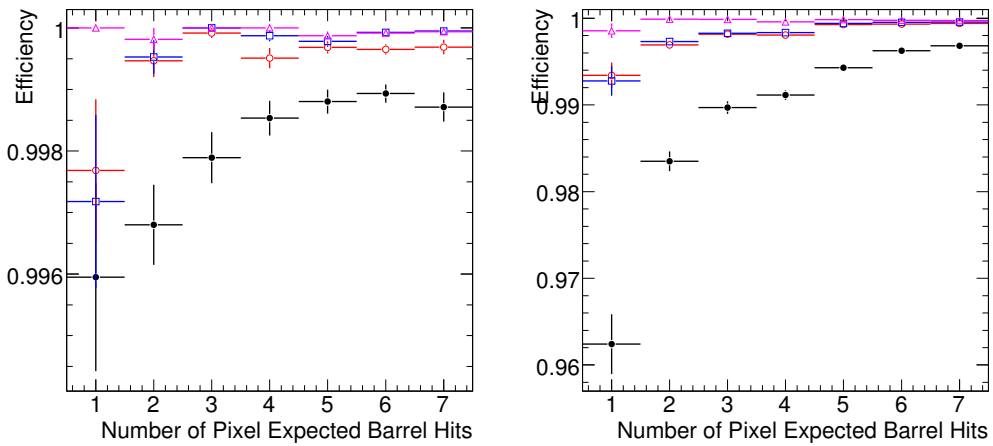
Figure 3.39: Pixel detection efficiency as a function of the number of expected pixel barrel hits on track with the solenoid magnet on (left) and off (right). The estimated efficiency is shown after the basic selection (cf. 3.4.1) in black solid circles, after the cluster association correction (cf. 3.4.3) in open red circles, and after an additional correction to avoid problematic pixels (cf. 3.4.4) in open blue squares and after the final tight selection on the number of SCT and TRT barrel hits (cf. 3.4.6) in open magenta triangles. Note the different *y*-axis scales used for the two plots.
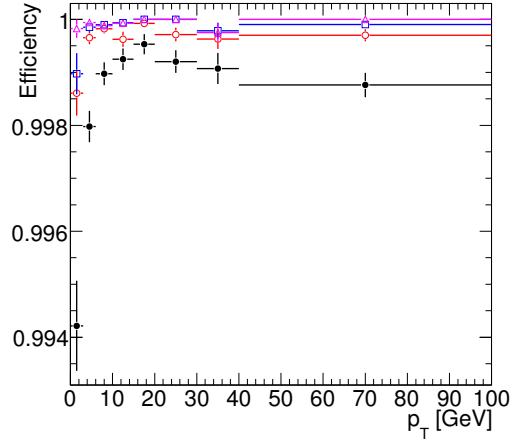
Figure 3.40: Pixel detection efficiency as a function of the track transverse momentum p_T for the solenoid-on data. The estimated efficiency is shown after the basic selection (cf. 3.4.1) in black solid circles, after the cluster association correction (cf. 3.4.3) in open red circles, and after an additional correction to avoid problematic pixels (cf. 3.4.4) in open blue squares and after the final tight selection on the number of SCT and TRT barrel hits (cf. 3.4.6) in open magenta triangles.
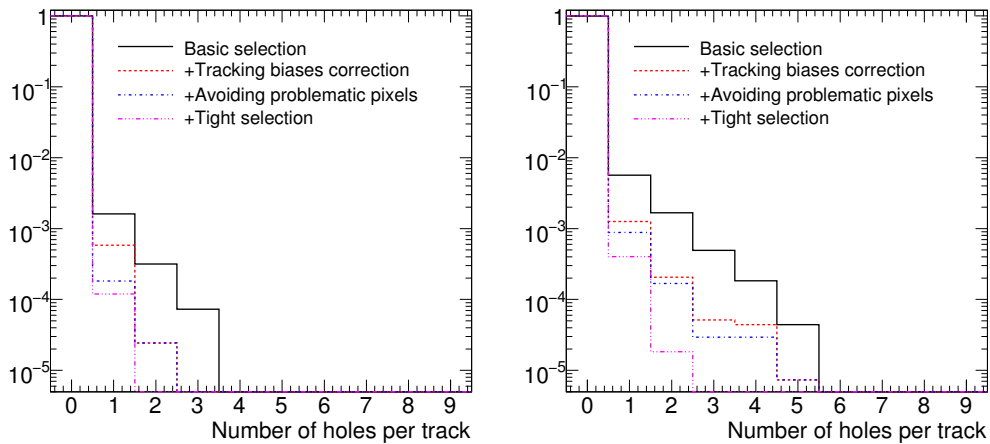

Figure 3.41: Number of pixel barrel holes per track with the solenoid magnet on (left) and off (right), after the basic selection, after different corrections and after the tight selection on the number of TRT and SCT hits.

90

number of SCT, TRT and pixel hits, multiple holes per track) are correlated. The same poorly reconstructed tracks are missing hits in all sub-detectors, and this is mostly affecting low p_T tracks for which multiple scattering is large. To remove these effects, tighter requirements on the number of SCT and TRT hits are applied before quoting the intrinsic cluster efficiency. The cuts are chosen to select the plateau of the distribution for each of these two variables. This corresponds to at least 12 SCT hits for both solenoid-on and solenoid-off data. The TRT-hit requirement for the solenoid-on data remains unchanged, but we require at least 40 hits for the solenoid-off data. These cuts result in a relative drop of the tracking selection efficiency of about 20%. However the selected sample contains only very good quality tracks. After these tight cuts, the efficiencies versus the track p_T and the number of expected pixel hits are now relatively flat (figures 3.39 and 3.40 in open magenta triangles). Also the number of holes per track is significantly reduced (figure 3.41). No extra cuts on these three latter variables is included and all residual correlations, which are relatively small, are treated as systematic uncertainties.

The tight cuts lead to an efficiency of 99.993 ± 0.003 for solenoid-on data and 99.976 ± 0.003 for solenoid-off data. There is a good agreement between these two samples, with a slightly lower efficiency for the solenoid-off sample. This effect was present from the beginning and remains after all corrections. In particular the cluster association correction is much more important for the solenoid-off sample. This points to a better quality of the reconstructed tracks in the solenoid-on sample [8]. Two hypotheses are noteworthy to explain the lower track quality of the field-off sample. First this sample contains tracks from muons with very low p_T (<0.4 GeV) and therefore high multiple scattering, while those tracks would curl in the field-on data and would not be reconstructed. In addition the track p_T is not available for solenoid-off data, while this information is used by the tracking and extrapolation algorithms to correct for material effects: this can lead to a better reconstruction in the presence of magnetic field. However no further attempts were made to investigate the origin of these differences, since the collected statistics is anyway too low to quantify the effects aforementioned.

3.4.7 Efficiency for various detector components

As mentioned before, all known dead modules and chips were excluded from the analysis. The efficiency of individual modules and chips is represented in figure 3.42. The solenoid-on and solenoid-off samples were combined to increase the

---

[8]The effect due to the difference in cluster multiplicity, due to the Lorentz shift, between the solenoid-on and the solenoid-off samples could not be investigated due to the large inefficiency due to tracking.
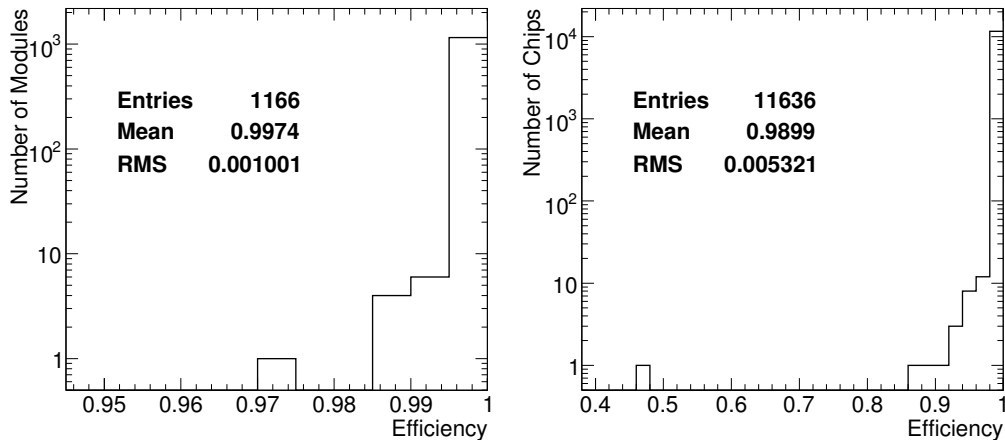
Figure 3.42: The detection efficiency per module (left) and per chip (right). Modules with at least 50 track intersections and chips with at least 10 track intersections were retained.

statistics. However for some modules and especially for some chips the overall statistics is still very low. Only modules with at least 50 expected hits and chips with at least 10 expected hits are shown. All checked components representing 80% of barrel modules and 50% of barrel chips were found to have a relatively high efficiency. One should note that the statistical error on the efficiency presented in figure 3.42 is very large and the numbers are presented just as a qualitative check. Much more statistics is needed to determine the efficiency per module or per chip with a reasonable statistical error.

3.4.8 Systematic uncertainties

The systematic uncertainties were studied only for the pure cluster efficiency, since it is a measurement of a well-defined property of the pixel detector.

The dominant systematic uncertainties are related to tracking. Residual uncertainties are quantified by tightening further the selection cuts and by monitoring the efficiency variations. The uncertainty introduced by the cluster association correction is estimated by shifting the corresponding cut on the hole-cluster distance. Since no updated SPM is available for the moment, the uncertainty due to an eventual wrong description of non-functioning pixels could not be determined. However we know that the number of problematic pixels will not change dramatically and the corresponding correction ought to be relatively small.

The shifts introduced by considering a different tracking algorithm or by a possible change of the alignment constants are not considered as systematic un-
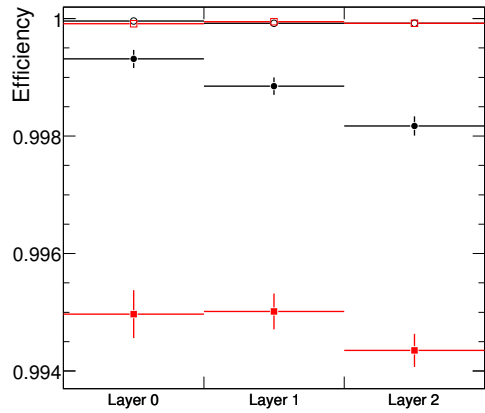
Figure 3.43: Comparison of the pixel detection efficiency (black circles) with the one obtained using an alternative track reconstruction algorithm (red squares). The closed markers correspond to the efficiency computed after the basic track selection (cf. 3.4.1). The open markers correspond to the efficiency computed after applying different corrections (cf. 3.4.3 and 3.4.4) and tightening the selection cuts (cf. 3.4.6). This plot was obtained using the solenoid-on sample.

certainties. In fact the cluster association correction and the tuning of selection cuts will change for distinct track reconstruction, in order to get the corresponding plateau distributions for different track properties. The efficiency will be dictated by the tuned values. Thus any uncertainty due to different reconstruction algorithm or different alignment parameters is already introduced in the uncertainty on different selection and correction cuts that we choose. The same argument is valid for the differences between the solenoid-on and solenoid-off samples. For reference the efficiency versus barrel layers for an alternative track reconstruction algorithm is represented in figure 3.43. There is a perfect agreement for the quoted intrinsic pixel efficiency between the two tracking algorithms, even if the discrepancy was very large before applying any correction.

We considered the following changes in our selection to estimate the upper bound on the efficiency uncertainty:

- tighter requirement on the number of SCT hits: nSCT $\geq$15;

- tighter requirement on the number of TRT hits: nTRT $\geq$40 (50 for B field off data);

- requiring the number of expected hits in the pixel barrel to be greater than two;

93

	Solenoid On [%]	Solenoid Off [%]
Combination of variations	**0.000**	**0.014**
Number of SCT hits	0.001	0.006
Number of TRT hits	0.000	0.007
Numb. Expected pixel hits	0.000	0.000
Number of holes	0.000	0.007
p_T	0.000	-
Loose distance hole-cluster cut	0.000	0.003
Tight distance hole-cluster cut	**-0.001**	**-0.005**

Table 3.17: Shifts in the detection efficiency for variations in selection requirements.

- excluding tracks with more than one pixel hole;

- requiring $p_T > 5$ GeV for solenoid-on data;

- increasing by a factor of two the requirement on the hole-cluster distance used for the cluster association correction: distance < 20 mm.

In addition, we considered the following change to estimate the lower bound of the efficiency uncertainty:

- decreasing by a factor of two the requirement on the hole-cluster distance used for the cluster association correction: distance < 5 mm.

To correctly treat correlations between the different variations, all cuts changes were made simultaneously to get the resulting systematic shift. These shifts are listed in table 3.17.

The final intrinsic cluster efficiencies are 99.993 ± 0.003 (stat.) $^{+0.000}_{-0.001}$ (syst.) for solenoid-on data and 99.976 ± 0.003 (stat.) $^{+0.014}_{-0.005}$ (syst.) for solenoid-off data. The solenoid-on and solenoid-off data are consistent after considering systematic uncertainties. Large effects from tracking in the solenoid-off sample leads to large uncertainties even after all corrections. Most selection changes does not lead to an efficiency change, considering the available statistics, for the solenoid-on sample. This points to the robustness of the tracking correction we applied for this sample.

3.5   Conclusion

The pixel detector is a key sub-detector for a large fraction of the ATLAS physics program: it plays a crucial role in initiating the charged-track pattern-recognition

94

thanks to its very low occupancy; and it is vital to measure the track parameters close to the interaction point, reconstruct secondary vertices and thus identify heavy flavors.

This detector is installed, commissioned and is currently taking data with cosmic rays. The pixel calibration and slow control data are important for a reliable MC simulation and for the data reconstruction. The offline infrastructure and the corresponding databases are ready and were successfully tested. The noise study, performed in this chapter, shows a very low pixel noise level of 10^{-10} hit per pixel per BC after masking about 0.1-0.2‰ noisy pixels. The pixel noise looks relatively stable with time. However more studies are needed to exactly quantify the noise fluctuations and determine a clear strategies especially for the online noise mask productions. The pixel detector exhibits a very high intrinsic cluster efficiency, close to 99.99%. The effective efficiency, including inefficiencies due to cluster-track association, goes down to about 99.8% for a track sample using basic selection cuts motivated by the ones that are generally used for physics analysis with collision data.

Chapter 4

The $t\bar{t}H(H \rightarrow b\bar{b})$ channel

The spontaneous symmetry breaking leading to the Standard Model Higgs boson, as well as our current knowledge of this boson, are summarised in chapter 1 and will not be repeated here. We will begin with a short review of the Higgs boson phenomenology at the LHC and with the ATLAS experiment. We will focus on the light Higgs boson scenario ($m_{b\bar{b}}$ <130 GeV) which is the region of interest for the $t\bar{t}H$ production. This region is also preferred by the electroweak data as shown in chapter 1. After a review of the event generators, the preselection of events with a signature compatible with the $t\bar{t}H(H \rightarrow b\bar{b})$ channel final state will be explained in details. Three reconstruction methods are then used to extract the Higgs boson invariant mass. Finally, we will discuss some of the problems leading to the bad significance and the large systematics for this channel.

4.1   The Higgs boson at the LHC

The Higgs boson coupling to fermions (λ_f) and to gauge bosons (λ_W and λ_Z), using the relations listed in chapter 1, are given by:

$$\lambda_f = \frac{gM_f}{2M_W}, \quad \lambda_W = gM_W, \quad \lambda_Z = \frac{gM_Z}{2\cos\theta_w}$$

where g is the weak coupling constant and θ_W the weak mixing angle. The Higgs boson coupling to a particle is proportional to the mass of the latter. This implies that the Higgs boson does not couple to massless particles as gluons and photons. These will define the Higgs boson production and decay.

At the LHC most hard-scattering events will proceed via gluon-gluon fusion. Since the Higgs boson does not couple to gluons, the $gg \rightarrow HX$ production happens through an intermediate particle which couples to both the Higgs boson and the gluons: the top quark is contributing the most to the amplitude, given its large
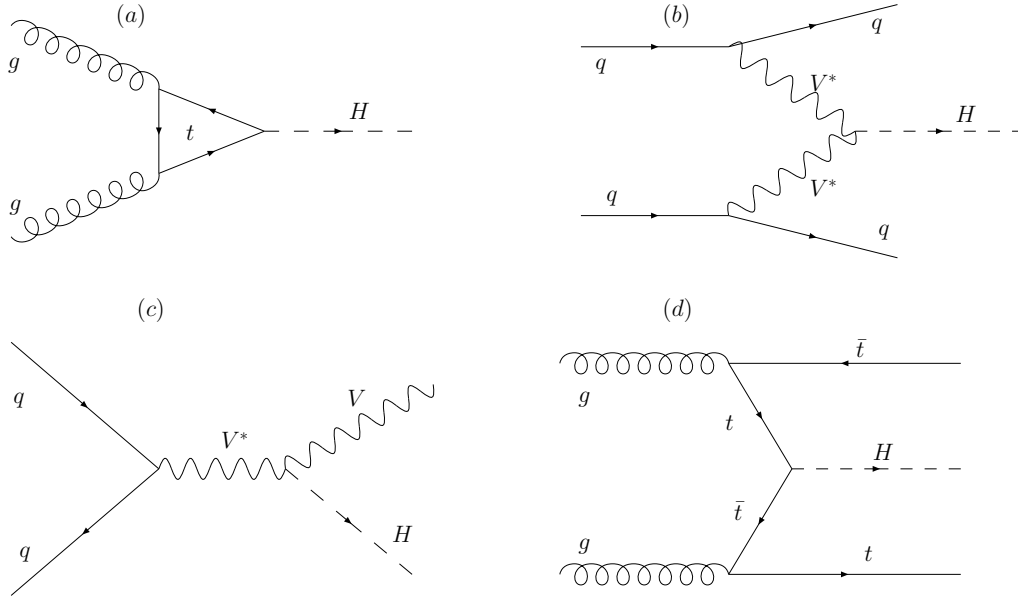
Figure 4.1: Some of the Higgs boson production channels: (a) Direct production, (b) VBF production, (c) WH and ZH associated productions and finally the $t\bar{t}H$ production in (d).

mass. Instead of a closed loop of quark tops, a pair of quark tops can also be produced in association with the Higgs boson. Finally, the Higgs boson can also be produced by quark-(anti)quark hard interactions through vector boson fusion (VBF) or associated production with a W or a Z boson. These four different production channels of the Higgs boson are illustrated in figure 4.1. The Higgs boson production cross-sections at the LHC, as function of its mass is represented in figure 4.2. One can clearly see that the direct production is one order of magnitude larger than the other production modes.

The branching ratios of the Higgs boson as a function of its mass are represented in figure 4.3. At low mass the Higgs boson decays predominantly into a $b\bar{b}$ pair. The ZZ and WW decay modes begin to be important above 130 GeV. The $t\bar{t}$ decay mode becomes important once the channel is open. The $\tau\tau$ and $\gamma\gamma$ decay modes are also represented. These channels are important at low mass even if they have a lower branching ratio as discussed in the following.

4.2 The light Higgs boson scenario with ATLAS

As mentioned in chapter 1, a light Higgs boson is the preferred scenario by the electroweak fits. In this case the channel with the highest cross-section (times
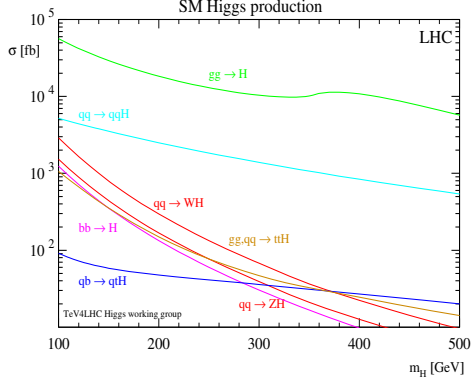
Figure 4.2: Cross-sections of the different production modes of the Higgs boson at the LHC as function of its mass [40].
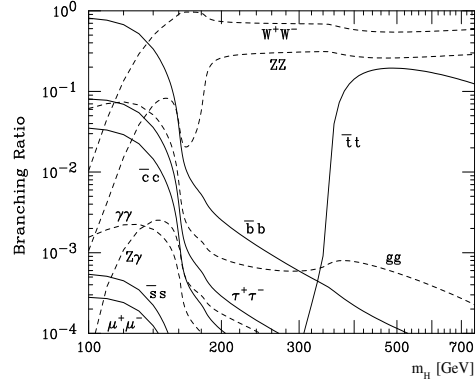

Figure 4.3: Branching ratios of the Higgs boson as a function of its mass [40].

branching ratios) is $gg \rightarrow H \rightarrow b\bar{b}$. This signature is impossible to extract in a hadron collider due to the large QCD background (order of mb). Several alternative channels had been tested e.g.:

- Direct production with the subsequent decay of the Higgs boson into two photons. The small branching ratio is compensated by the relatively large direct production cross-section, and this channel is considered as one of the most important channels at low mass. In fact a $\gamma\gamma$ signal provides a clean signature that can be relatively easily extracted from the background;

- The VBF channel with the subsequent decay of the Higgs boson into two τ leptons. This channel also provides a promising potential for a Higgs boson discovery at low mass. This channel is characterised by the absence of jets in the central region. A jet veto at small $|\eta|$ can reduce the QCD background;

- Associated production of the Higgs boson with a W or a top quark pair with the subsequent decay of the Higgs boson into a $b\bar{b}$ pair. The W or one of the top quarks provides a lepton required for the trigger and for a good rejection against the QCD background. The Higgs production with a top quark pair will be the subject of the analysis treated in this chapter.

At low mass a Higgs boson discovery is really difficult and the combination of several channels is definitively needed. The expected significance with the AT-LAS detector after combining different channels for 10fb^{-1} is represented in figure 4.4. One can clearly see that at low mass (<130 GeV) even the combination of several channel does not provide a significance of 5 which is needed for a

discovery, except at the upper end of the mass range. The $t\bar{t}H(H \to b\bar{b})$ channel was removed from the final combination for reasons that will be discussed in this chapter.
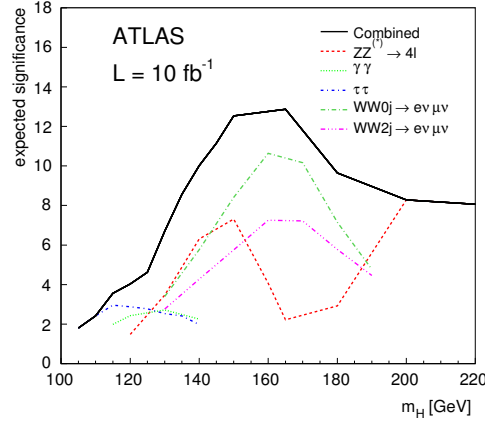

Figure 4.4: Expected significance for a Standard Model Higgs boson search, with the ATLAS experiment, as a function of its mass [1].

4.3 The $t\bar{t}H(H \to b\bar{b})$ channel

The $t\bar{t}H(H \to b\bar{b})$ channel is important to understand the electroweak sector of the Standard Model. This channel opens the possibility of measuring the top and b-quark Yukawa couplings. Even being challenging, this channel might also play its role for a light Higgs boson discovery with the ATLAS detector. One should note also that a recent analysis shows an improved potential for the WH channel [41].

Within the Standard Model, the top quark decays in 99.91% into a W boson and a b-quark. The $H \to b\bar{b}$ is dominant for a light Higgs boson and the final state of the $t\bar{t}H$ channel will at least be formed of four b-jets. The final state topology will be then defined by the decay of each of the two W bosons. We can distinguish 3 different final states having 0, 1 or 2 leptons:

- The all-leptonic final state: both W bosons decay to a lepton and a neutrino. This channel has the smallest branching ratio, 10%. The presence of the two neutrinos makes the reconstruction of the $t\bar{t}$ system very difficult. On the other hand this channel has the cleanest topology and the highest trigger efficiency;

- The all-hadronic channel: both *W* bosons decay hadronically. This channel has the largest branching ratio of 46%. On the other hand the final state consists of at least 8 jets. This present a serious problem for the trigger and for the extraction from the QCD background. Also solving the jet combinatorics is an important problem for this channel;

- The lepton-plus-jets channel: One *W* boson decays hadronically and the other one decays leptonically. This channel is a compromise between the two channels listed above. It has an acceptable branching ratio of 44%, and the presence of one lepton ensures a high trigger efficiency.
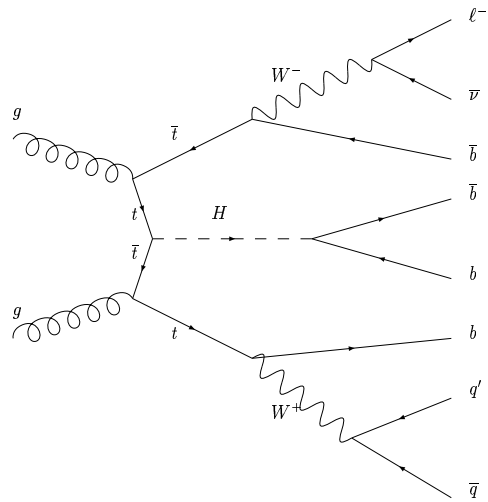

Figure 4.5: Feynman diagram representing the lepton-plus-jets final state configuration of the $t\bar{t}H(H \to b\bar{b})$ channel.

In the present analysis, we will consider only the lepton-plus-jets channel represented in figure 4.5. The τ-leptons were not considered since they can decay leptonically or hadronically and contribute to both leptonic and hadronic channel. Without the τ-leptons the lepton-plus-jets channel branching ratio goes down to 29%. In the following, the word lepton will mean only electron or muon.

Physics backgrounds   The main physics background for the $t\bar{t}H(H \to b\bar{b})$ channel comes from the $t\bar{t}$ production with at least two extra jets. When two of the extra jets are *b*-jets the background has the exact same signature as the signal. This is the so-called irreducible $t\bar{t}b\bar{b}$ background. In the other cases, extra jets are *c*-jets or light-jets, the background is reducible using *b*-tagging. This $t\bar{t}$+jets background is important, even after *b*-tagging jets, due to its huge cross-section. The $t\bar{t}c\bar{c}$ background cross-section is 60% higher than $t\bar{t}b\bar{b}$. However the *c*-jet b-tagging

efficiency is about five times lower than for b-jets. Therefore the $t\bar{t}c\bar{c}$ background is expected to be negligible compared to $t\bar{t}b\bar{b}$ when requiring 4 b-tags and will not be treated separately. The contribution from $t\bar{t}c\bar{c}$ is anyway considered in the $t\bar{t}$+jets background.

Other physics processes can also contribute to the final background. The large QCD background can still fake a lepton-plus-jets final state if a jet is misidentified as an electron or by the semi-leptonic decay of a heavy-flavor hadron inside the jet. This background is expected to be heavily reduced after applying b-tagging and after the reconstruction of both top quarks. Also b-tagging and the full reconstruction of the $t\bar{t}$ system protect against other non-top backgrounds such as W+jets [42] and single-top production. For this study, we will only consider the main backgrounds coming from $t\bar{t}$ +jets production.

4.4   Monte Carlo generation and detector simulation

Process	Generator	σ(pb)	K-factor	PDF set
$t\bar{t}H$	Pythia	0.671 NLO	1.25	CTEQ6L1
$t\bar{t}b\bar{b}$(QCD)	AcerMC	15.7 NLO	1.8	CTEQ6L1
$t\bar{t}b\bar{b}$(EW)	AcerMC	1.7 NLO	1.8?	CTEQ6L1
$t\bar{t}X$	MC@NLO	833 NLO+NLL	-	CTEQ6M

Table 4.1: Monte Carlo generators and cross-sections for different processes. All generators, except MC@NLO which uses Herwig, are interfaced to PYTHIA for the simulation of the initial and final state radiation, hadronisation, and further decays. Usually the generators are at leading order (LO) and the cross-sections are rescaled to the next-to-leading order (NLO) using the K-factors.
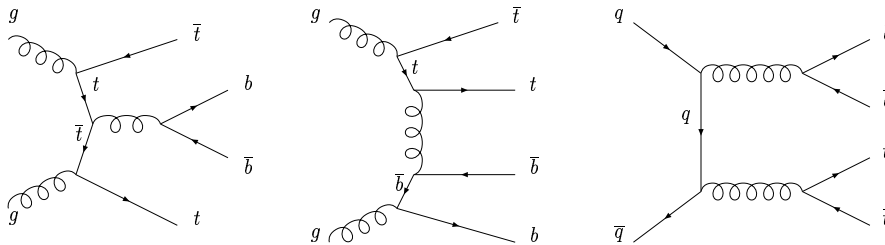

Figure 4.6: Some of the Feynman diagrams describing the $t\bar{t}b\bar{b}$ (QCD) production.

NLO cross-section for the $t\bar{t}b\bar{b}$ process was computed recently [43, 44]. Unlike previous studies, this study will use the NLO cross-sections for both signal
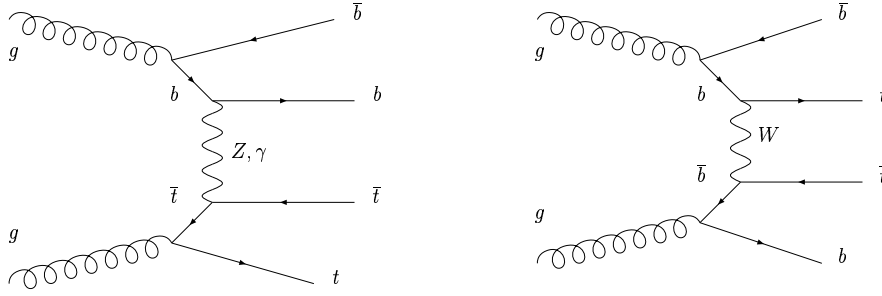
Figure 4.7: Some of the Feynman diagrams describing the $t\bar{t}b\bar{b}$ (EW) production.

and background processes. The different processes along with the used cross-sections, generators, and the PDF sets are summarised in table 4.1. The signal sample is generated for a Higgs boson mass of M_H = 120 GeV with Pythia 6.403 [45]. The generated process is $pp \rightarrow t\bar{t}HX \rightarrow \ell v b q \bar{q}' \bar{b}b\bar{b}X$, with $\ell =$ e or μ. The factorisation and maximal ISR scales are identical, their value being $Q^2 = m_t^2 + \max(p_T{}^2{}_t, p_T{}^2{}_{\bar{t}})$ with $m_t = 175$ GeV. The cross-section of this process is known at the next-to-leading order (NLO) with a K-factor of about 1.25^1 [46, 47, 48].

The $t\bar{t}b\bar{b}$ process is divided into two samples: QCD and electroweak (EW) samples. The $t\bar{t}b\bar{b}$ (QCD) sample correspond to all diagrams not including electroweak bosons which are separated in the $t\bar{t}b\bar{b}$ (EW) sample. Some of the diagrams describing these two processes are described in figures 4.6 and 4.7. Both processes can be initiated by a gluon-gluon or a $q\bar{q}$ pair. Only the dominant (95%) gluon fusion has been simulated whith AcerMC [49] program interfaced with Pythia. The generated process is gg $\rightarrow t\bar{t}b\bar{b}X \rightarrow \ell v b q \bar{q}' \bar{b}b\bar{b}X$, with $\ell =$ e or μ. The gg $\rightarrow t\bar{t}b\bar{b}X$ cross-section is increased to account for the $q\bar{q}$ production. The Q-scale used is $Q = M_H/2 + m_t = 235$ GeV. The NLO cross-section for the QCD process is found to be 1.8 [43, 44]. It is important to note that the scale dependence is reduced from $\pm 70\%$, for the LO cross-section, to $\pm 33\%$ for NLO cross-section. The errors on the cross-section are computed by varying the scale by factors of one-half and two. In this analysis, we will consider the K-factor of the $t\bar{t}b\bar{b}$ (EW) process, which is not available currently, to be the same as for the $t\bar{t}b\bar{b}$ (QCD) process even if we naturally expect this factor to be closer to the $t\bar{t}H$ or $t\bar{t}Z$ processes of about 1.3. However the EW process corresponds to only 10% of the total $t\bar{t}b\bar{b}$ cross-section and the approximation we make does not have any major effect on the analysis.

The $t\bar{t}$ background events have been generated with the MC@NLO 3.1 [50], interfaced to Herwig 6.510 [51, 52] and Jimmy [53] for the underlying event. The exact generated process is $pp \rightarrow t\bar{t} \rightarrow (\ell v, q\bar{q}')b\ell v b$ with $\ell =$ e, μ, τ. The $t\bar{t}$

---

^{1}for $Q^2 = (M_H/2 + m_t)^2$.

cross-section is known to the NLO order with additional NLL corrections [54].

One should mention that the signal and the background samples were generated with a filter requiring one electron or one muon with $|\eta| < 2.7$. To increase the Monte Carlo statistics, an additional filter is applied to the $t\bar{t}$ sample before the full simulation. This filter requires at least six jets with $p_T > 14$ GeV and $|\eta| < 5.2$ and at least four jets with $p_T > 14$ GeV and $|\eta| < 2.7$. The $t\bar{t}$ filtered sample will be called the $t\bar{t}$+jets background. Table 4.2 lists the number of generated events with the corresponding cross-sections and integrated luminosity at the LHC. All branching ratios and filter efficiencies are included when computing the cross-sections. A $H \to b\bar{b}$ branching ratio of 67.5% at 120 GeV is used[55]. The $W \to \ell\nu$ branching ratio is taken to be 10.8% [40]. One should note that the $t\bar{t}$+jets sample contains about 14% of events with negative weight. These events are taken into account when counting the event number and the cross-section for the corresponding samples.

The $t\bar{t}b\bar{b}$ and the $t\bar{t}$+jets samples present an overlap when the two extra jets in the $t\bar{t}$+jets sample are b-jets. In the $t\bar{t}$+jets sample the extra b-jets are generated by parton shower. The $t\bar{t}b\bar{b}$ sample provides a better description of this important background, using matrix elements. To account for this overlap, all events with a $b\bar{b}$ pair in the $t\bar{t}$+jets sample are removed. This correspond to about 10% of the total number of events. The overlap is also accounted in table 4.2.

To increase the $t\bar{t}$+jets statistics, another $t\bar{t}$+jets sample was produced with exactly the same specifications described before. A 'mixed' simulation of the AT-LAS detector is used to gain in CPU time relative to the full simulation. This simulation is done with ATLFAST-II (AF-II) program which provides a full simulation of the inner detector and a fast simulation of the calorimeter [2]. The 'mixed' simulation allows to preserve exactly by construction the b-tagging performance and correlations. This is very important as the b-tagging is a major ingredient for this analysis. This sample will be only used to extract the final mass shape and numbers of the $t\bar{t}$+jets background. This allows to reduce the large statistical errors on the Monte Carlo generated events present in the fully simulated sample.

4.5 Previous studies

The first ATLAS sensitivity study for the $t\bar{t}H(H \to b\bar{b})$ channel has been presented in the ATLAS physics TDR [56]. This study was performed for a generated Higgs boson mass of 120 GeV and with a fast simulation of the ATLAS detector. A cut-based technique was performed to reconstruct the entire final state of the $t\bar{t}H(H \to b\bar{b})$ channel. The analysis results in a significance of 3.6 for 30 fb^{-1} of

---

[2]In the version used for this analysis, a fast simulation is also used for the muon system.

Process	Detector simulation	Filter efficiency	$\sigma \times$ BR (fb)	Generated events	L (fb^{-1})
$t\bar{t}H$	full	95.3%	126	92.7×10^3	733
$t\bar{t}b\bar{b}$ (QCD)	full	94.3%	4312	98.3×10^3	22.8
$t\bar{t}b\bar{b}$ (EW)	full	94.3%	466	24.7×10^3	53.1
$t\bar{t}$+jets	full	14.6%	121618	710×10^3	6.4
$t\bar{t}$+jets AF-II	mixed	14.6%	121618	749×10^4	67.7

Table 4.2: Simulation type, filter efficiency and number of generated events with the corresponding cross-section (NLO) and the equivalent integrated luminosity for all samples.

data.

This study was repeated by Cammin and Schumacher [57] and leaded to an updated significance of 2.0. This significance drop was due to the differences in the Monte Carlo generators and to the updated cross-sections used. Cammin and Schumacher also used a likelihood technique to solve the jet combinatorics which improved the significance up to 2.7.

The likelihood technique as well as the cut-based analysis were also performed by Corréard [58] in his thesis work. A significance of 4 was found but the statistics of the simulated $t\bar{t}$+jets process was too low to make a final statement. Systematic errors were not included in any of these later analysis.

The latest ATLAS results concerning this channel were reported in the latest Physics CSC book [1]. Both cut-based and likelihood analysis were repeated using a full simulation of the ATLAS detector. Both techniques result in a estimated S/$\sqrt{B}$ around 1.9. The significance drop is mainly due to a more realistic description of the detector that leads to a decrease in the b-tagging performance. The $t\bar{t}$+jets cross-section was increased by a factor of two after using the NLO+NLL calculation. Also a third study was reported in the Physics TDR that leads to S/$\sqrt{B}$ of 2.2. This study is based in a constrained fit associated with a multidimensional likelihood technique to reconstruct the $t\bar{t}$ system. The studies presented in this chapter correspond to the cut-based and likelihood analysis presented in the latest ATLAS CSC book.

Finally, it is worth mentioning that CMS reported [59] a significance of 1.8 for the electron channel and 1.6 for the muon channel, in both cases for 60 fb^{-1}. A detailed comparison with the ATLAS analysis was not performed however a general comparison of the final results can be found in [60].

4.6 Scope of the analysis

To be able to extract the $b\bar{b}$ signal corresponding to the Higgs boson decay, one should choose two b-jets among the four present in the final state. We will use the same technique used in all previous analysis i.e. reconstruct the full $t\bar{t}$ system and then use the additional b-jets to reconstruct the Higgs boson invariant mass. To do that, a first preselection step is performed to select events with a final state corresponding to one lepton and at least six jets configuration. *B*-tagging is used to select the four b-jets coming from both top quarks and Higgs decay. This will help to reduce the jet combinatorics. *B*-tagging is also mandatory to discriminate against the large $t\bar{t}$ plus additional light jets background. We will present three different techniques to solve the jet combinatorics and reconstruct the $t\bar{t}$ system: the cut-based, the likelihood and the boosted decision tree (BDT) techniques. No final selection is applied to discriminate between the signal and the physical background. In fact the signal exhibits a poor reconstruction performance: kinematic differences between the signal and the $t\bar{t}$ backgrounds, especially the irreducible $t\bar{t}b\bar{b}$ background, are diluted by the large jet combinatorics in the signal. Finally an attempt to extract the $b\bar{b}$ mass from the background is presented. The method, first proposed in [1], will be investigated. The final result will be given assuming 30fb^{-1} of data at low-luminosity (10^{33} cm^{-2}s^{-1}) , which correspond to the initial LHC scenario. At this luminosity, with a LHC scenario assuming 75 ns between bunch crossings, an average of six pile-up events is expected. The pile-up was not included in the simulated samples and will not be studied.

4.7 Important definitions

For convenience, we will refer to the *W* boson which decays into a lepton and a neutrino as the leptonic *W* and the one that decays into two jets as the the hadronic *W*. Similarly, we will refer to the top quark decaying into a leptonic *W* as the leptonic top and the one decaying into a hadronic *W* as the hadronic top.

The notion of purity is very important for this analysis. In fact as seen in section 4.13, it is important to find the correct combination of jets used to reconstruct the top quarks and the Higgs boson. Before defining the purity one should match reconstructed object with the true generated partons and leptons. A matching in space (distance in terms of ΔR) is used to assign a reconstructed object a truth match. For leptons, a cut of $\Delta R < 0.1$ is used, while a cut of $\Delta R < 0.4$ is used for jets. In case of multiple reconstructed objects matching the same truth object, the closest one is considered.

After solving the jet combinatorics, we define the correct combination for a given object as the one where all its decay products match the corresponding truth

information e.g. the correct combination for the leptonic top is defined as the one where the preselected lepton matches the true lepton from the W boson decay and the chosen jet matches the b-quark from the leptonic top decay. The purity is defined as the fraction of events for which the correct combination is used.

It is also important to define the original flavor of a jet (commonly known as the jet labelling). This is important to study the b-tagging performance presented in section 4.8.4. A jet is labelled as a b-jet if a b-quark is present in a cone of $\Delta R <$ 0.3 around the jet axis. If this is not the case, we search recursively for c-quark then τ-leptons, in the same cone size, to define c-labelled jets and τ-labelled jets. If none of the previous cases is valid the jet is labelled as a light jet.

4.8 Event pre-selection

This step selects events with one lepton, at least six jets of which four are tagged as b-jets: we begin by selecting events that pass the trigger requirements. The events with exactly one reconstructed lepton are then selected. Vetoing the presence of a second isolated lepton is intended to remove additional sources of background. After the lepton requirements, we ask for at least six calorimeter jets of which at least four must be b-tagged.

4.8.1 Trigger efficiency

No dedicated $t\bar{t}H$ trigger has been used for this analysis. As for the extraction of $t\bar{t}$ samples, we will use a general hight-p_T lepton trigger which is efficient in the presence of a W boson that decays to leptons. ATLAS trigger menu [1] includes several choices for a lepton trigger. For this analysis a logical OR is used combining three different triggers:

- The 'e25i' trigger: this trigger require a hight-p_T isolated electron with a $p_T > 25$ GeV. The efficiency of this trigger with respect to signal events with an offline preselected electron is about 78%;

- The 'mu20' trigger: the trigger requires a muon with p_T higher than 20 GeV. The efficiency of this trigger with respect to signal events with an offline preselected muon is about 80%;

- The 'e60' trigger: This trigger requires an electron with p_T higher than 60 GeV. The isolation requirement is dropped. This can improve the efficiency of the 'e25i' trigger. The efficiency of this trigger with respect to signal events with an offline preselected electron is about 45%. Among these,

7% were not triggered by the 'e25i' trigger. This will increase the electron trigger efficiency to about 85%.

The trigger efficiency with respect to events with one preselected lepton is about 83%. It is similar for the signal and the background samples considered. This is expected since all considered samples contains the same $t\bar{t}$ topology with an isolated hight-p_T lepton from a W decay.

4.8.2 Lepton pre-selection

As previously stated, one and only one lepton with identification, acceptance and isolation cuts should be reconstructed in the events. We define the lepton efficiency as the number of selected leptons with respect to the true generated leptons in the same p_T and pseudo-rapidity (η) ranges. Since we are only interested by leptons coming from the W boson decay, all leptons generated by other processes, e.g. semi-leptonic decay of heavy flavors, are considered as a contamination of our selected lepton sample and will be counted as fake leptons.

4.8.2.1 Electron pre-selection

Cuts	$t\bar{t}H$	$t\bar{t}b\bar{b}$ (QCD)	$t\bar{t}b\bar{b}$ (EW)	$t\bar{t}$+jets
Acceptance	89.5±0.1	89.6±0.1	89.1±0.3	87.7±0.0
+Identification	81.5±0.2	82.1±0.1	81.3±0.4	80.3±0.0
+Isolation	79.3±0.2	80.3±0.2	79.6±0.4	78.7±0.0

Table 4.3: Efficiency for electrons after each selection cut for all samples. The errors are statistical only.

An electron is defined as a calorimeter cluster that match with an inner detector track. The ATLAS 'hight-p_T' electron algorithm [1] is used for this analysis. Electrons candidates are required to fulfil the acceptance cuts: $p_T > 25$ GeV and $|\eta| < 2.5$. Identification cuts, corresponding to the 'isEM loose' electron selection described in [1], are applied. These cuts make use of the hadronic leakage in the hadronic calorimeter and of the shower shape in the middle layer of the EM calorimeter. Further calorimeter based cuts, concerning the shower shape were added. These correspond to the calorimeter cuts used for the 'isEM medium' electron selection. These cuts use the shower shape in the first layer of the EM calorimeter. The tracking cuts used for the 'isEM medium' electron selection were not applied since they reduce significantly the efficiency. Finally, an isolation cut is applied on the ratio between the transverse energy of additional tracks inside a
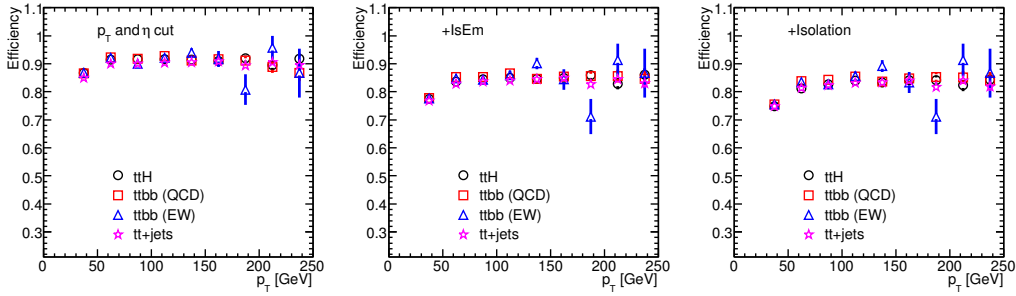
Figure 4.8: Efficiency for electron reconstruction and identification as a function of the generated electron p_T, for all the samples considered. From left to right, selection cuts are cumulated.

Figure 4.9: Efficiency for electron reconstruction and identification as a function of the generated electron η, for all the samples considered. From left to right, selection cuts are cumulated.
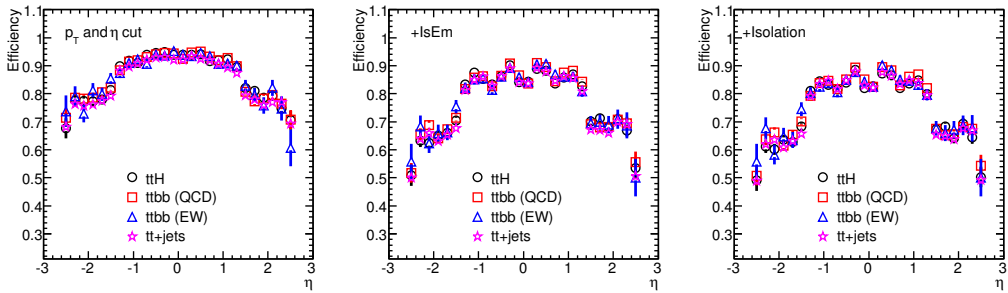
cone of size 0.2 in ΔR around the electron track, and the electron p_T. This ratio is required to be below 0.15.

The cuts were optimised to ensure a good efficiency for selecting an electron coming from a W boson decay. The integrated efficiency after each of the pre-selection cuts, are summarised in table 4.3. As expected, all samples have a comparable behaviour since the electron is generated by a W boson from a top quark that is present in all samples. The efficiency, as a function of the electron p_T and η for all different physics samples, are shown in Fig. 4.8 and 4.9. The efficiency drops at low-p_T next to the 25 GeV cut. In addition, the efficiency presents a large drop in the crack regions ($|\eta| \simeq 1.4$) and in the end-cap regions ($|\eta| > 1.4$).

The electron selection cuts also ensure a low contamination level from fake electrons or from electrons not generated by a W. After all cuts the contamination rate is 1.7% for the signal sample. About 40% of the contamination is coming from actual electrons from B- and D-mesons decay. For the remaining fakes, about a fourth of them were traced back as originating from photon conversions

where the photon was emitted by a W.

Since no QCD simple was generated for this analysis, the rate of jets faking an electron could not be precisely measured. However the rejection against jets for the 'isEM loose' and 'isEM medium' selections are given in [1]. We should note that the isolation requirement should provide a further jet rejection. A rough estimation, assuming six jets per event and 1% contamination from jets faking an electron, leads to a jet rejection of about 1200.

4.8.2.2 Muon pre-selection

Cuts	$t\bar{t}H$	$t\bar{t}b\bar{b}$ (QCD)	$t\bar{t}b\bar{b}$ (EW)	$t\bar{t}$+jets
Acceptance	94.7±0.1	94.5±0.1	94.9±0.2	83.7±0.0
+χ^2/dof	93.5±0.1	93.3±0.1	93.6±0.2	92.6±0.0
+Isolation	89.1±0.1	89.9±0.1	90.6±0.3	89.2±0.0
+d0 cut	88.4±0.1	89.2±0.1	89.9±0.3	88.4±0.0

Table 4.4: Muon efficiency after each selection cut for all samples. The errors are statistical only.

A muon is defined as a combination of a muon spectrometer track and an inner detector track. Muon candidates are reconstructed using the ATLAS Staco 'hight-p_T' muon algorithm [61]. The muon candidate must fulfil the acceptance cuts: $p_T > 20$ GeV and $|\eta| < 2.5$. In order to remove poorly reconstructed muons a loose upper cut of 30 on the reduced χ^2 of the muon combined fit is applied. We also require an isolation cut of 0.3 on the ratio between the transverse energy deposited inside a cone size ΔR=0.2 around the muon track and the muon p_T. A further cut is applied on the muon track transverse impact parameter ($|d_0| < 50$ μm) to discriminate against muons generated by the decay of long-lived mesons.

The muon efficiency after each selection cut is summarised in table 4.4. This quantity is also shown in figures 4.10 and 4.11 as a function of muon p_T and η for all different physics samples. As for electrons, the efficiency drops at low p_T. The low p_T region also presents a higher contamination from muons originated by a meson decay. The effect of the crack region is clear. Also the efficiency drop at $|\eta|$=0. This region is not instrumented for the muon system to allow the passage of different services. The selected muons are contaminated by 1.9% of reconstructed muon not originated by the W boson decay for the signal sample. The actual muons coming from B- and D-meson decays represents 84% of this contamination.
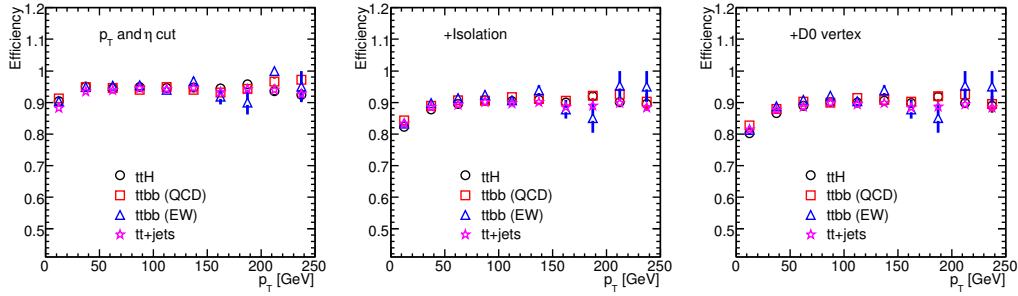
Figure 4.10: Efficiency for muon reconstruction and identification as a function of the generated muon p_T, for all the samples considered. From left to right plots, selection cuts are cumulated.

Figure 4.11: Efficiency for muon reconstruction and identification as a function of the generated muon η, for all the samples considered. From left to right plots, selection cuts are cumulated.
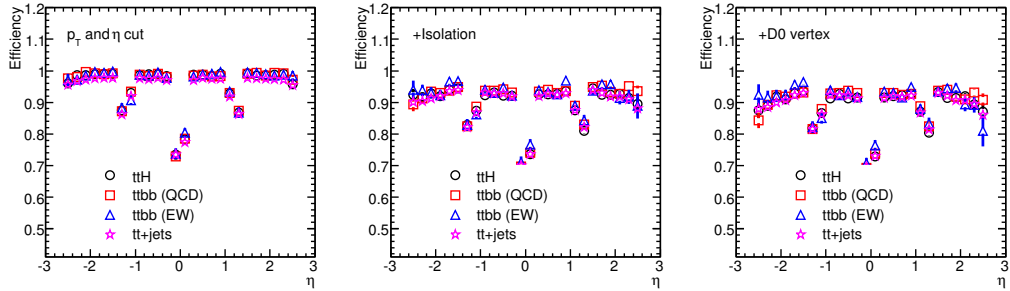
4.8.3 Jet pre-selection and calibration

To reconstruct the four-momentum of the partons produced in the original collision, calorimeter jets are reconstructed using a seeded fixed-cone algorithm with a cone size of $\Delta R = 0.4$ [1]. The jets must fulfil the acceptance cuts: $p_T > 20$ GeV and $|\eta| < 5$. Jets overlapping with electrons are removed as described in section 4.8.3.1. The calorimeter jet energy is corrected by adding the energy of muons inside the jet and then calibrated to correct for residual effects as described in sections 4.8.3.2. The p_T of the leading jets are shown in figure 4.12. Signal events have the most energetic jets. The ones from the $t\bar{t}$+jets sample present the lowest jet energy especially for the sixth leading jet which is mostly generated by the parton shower and may be too soft. There is no significance difference between the $t\bar{t}b\bar{b}$ (QCD) and the $t\bar{t}b\bar{b}$(EW). The jet multiplicity is shown in figure 4.13 after the acceptance cuts and the jet-electron overlap removal. One can clearly see the large number of events with more than six jets which might present an additional

110

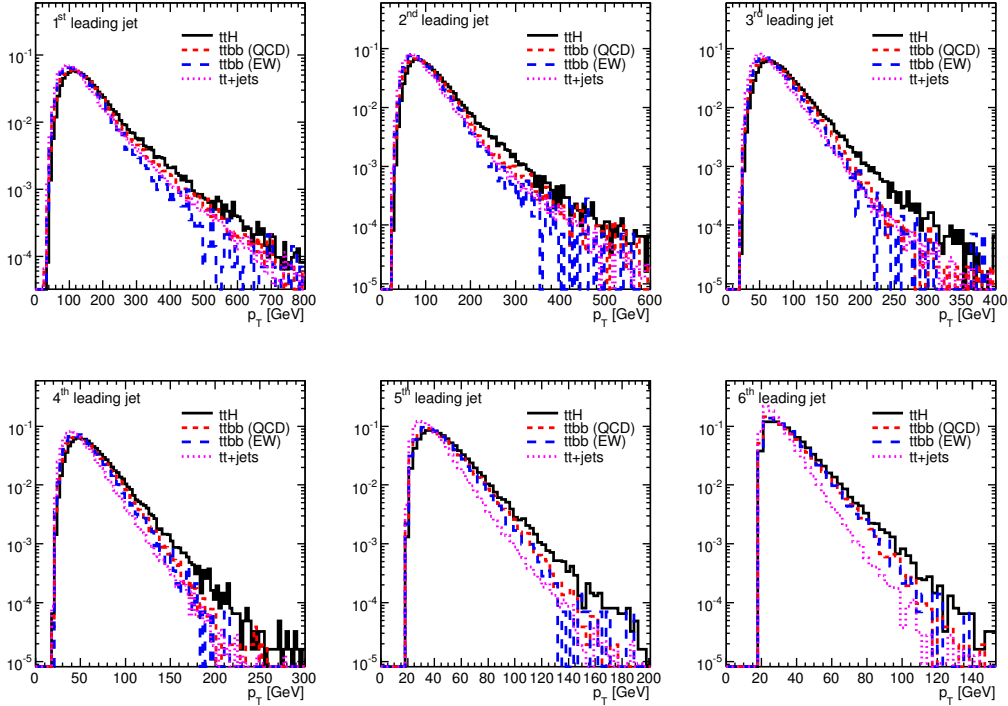problem from the jet combinatorics solving. Only events with at least 6 jets are kept for the analysis.

Figure 4.12: p_T spectra for the first 6 leading jets in events with at least 6 jets for the signal and background samples.

4.8.3.1 Overlaps with electrons

Most high-energy electrons are reconstructed by the jet algorithm. It is important to identify these electrons in the jet collection and remove the overlap with the electron collection. To remove the overlap we consider the following procedure: each jet matching a reconstructed electron, fulfilling the cuts defined in section 4.8.2.1, within a ΔR of 0.2, and for which the ratio of the electron to the jet transverse momenta is greater than 0.75, is considered as an electron and discarded from the jet collection. About 4% of the jets are removed by this selection, 99% of them being generated by actual true electrons.

4.8.3.2 Jet four-momentum corrections

About 20% of the time a B-meson decay cascade gives rise to a muon. These muons are usually called soft-muons due to their relatively low energy. A muon
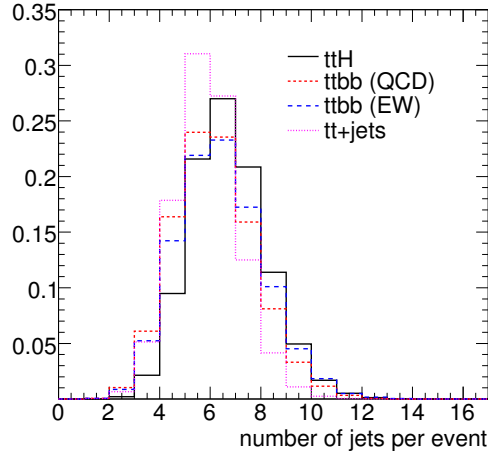
Figure 4.13: Multiplicity of jets, inside p_T and η acceptance, and after the removal of the jet-electron overlap, for the signal and background samples.

deposits a small amount of energy (about 3 GeV) in the calorimeter and thus the full muon energy is not computed within the reconstructed jet corresponding to the original parton. The muon four-momentum, measured in the inner detector and the muon spectrometer, should be added to the jet four-momentum for a better estimation of the b-partons four-momenta. Both high-p_T and low-p_T Staco muon algorithms are used to reconstruct the soft muons. The overlap between the two algorithms are removed if two muons match within $\Delta R = 0.1$. All muons already selected as coming from a W boson decay (cf. 4.8.2.2) are discarded. All soft muons are required to pass the acceptance cuts: $p_T > 4$ GeV and $|\eta| < 2.5$. An upper cut of 30 on the reduced χ^2 of the muon fit is also applied. Finally, we apply a loose anti-isolation requirement, corresponding to a lower cut of 0.1 on the energy, reconstructed in the calorimeter within a cone of $\Delta R = 0.2$ around the muon track, divided by the muon p_T. This selection results in a soft muon efficiency around 87% and a contamination around 24% for the signal sample. 25% of the contamination is actualy true muons coming from W boson decay but poorly isolated.

The muon four-momentum is added to the jet momentum if it is inside a cone of $\Delta R < 0.4$ of the jet axis. 91% of the soft muons are added to jets. 41%(35%) of those are actually matching to true soft muons originated by a $B(D)$-meson. Figure 4.14 shows the improvement in the leptonic top and the Higgs boson mass resolutions for combinations with at least one corrected b-jet. The correct combinations of jets is used. The shift in the mass due to the missing energy from the muon is clear. Also the soft muon correction improves the mass resolution.

Physics effects e.g. out-of-cone effects and neutrinos, are not corrected when
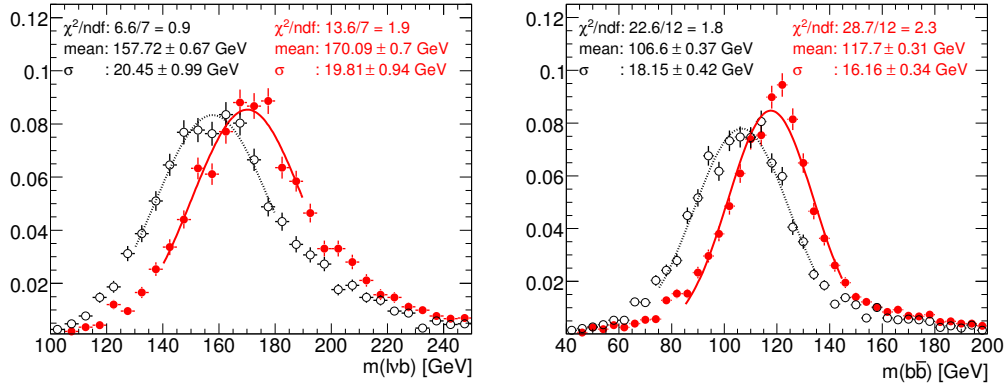
112

Figure 4.14: Effect of adding a reconstructed soft muon to the b-jets on the leptonic top mass (right) and the Higgs boson mass (left), where the correct jet combination is chosen. In these plots, the b-jet used for the top reconstruction and at least one of the b-jets used for Higgs reconstruction have been corrected by the muon correction. Red solid (black open) markers and solid (dotted) line show the mass distribution and fitted values for jets after (before) correction. The Monte Carlo based calibration is applied for both plots.

the jet calibration, at calorimeter cell level, is applied. To correct for these residual calibrations a parametrisation (five degree polynom dependent of the jet p_T) was derived from the full simulation [62]. b-jets are treated separately from other jets as they present a high level of neutrino production due to semi-leptonic decays. This correction is applied after adding the soft muon to the jet momentum. The impact of the calibration on the Higgs boson mass peak where the correct jet combination is chosen is shown in Figure 4.15. Both the mass peak location and the resolution are improved.

Table 4.5 summarises the jet calibration correction effects for both b- and light-jets. The p_T offset w.r.t. true partons is improved from 5.72 GeV to -0.48 GeV for b-jets. The resolutions remain the same around 10 GeV. For light jets, the offset with true parton changes from 2.43 GeV before corrections to -1.51 GeV after corrections. The resolution is about 8 GeV is both cases. The effect of the soft muon correction is clear when only the jets concerned by this correction are considered.

4.8.4 B-tagging

B-meson have a relative large lifetime with respect to other mesons. A B-meson with p_T=50 GeV will fly about 5 mm in the detector before it decays. The resulting child particles will create tracks that can be distinguished from tracks coming
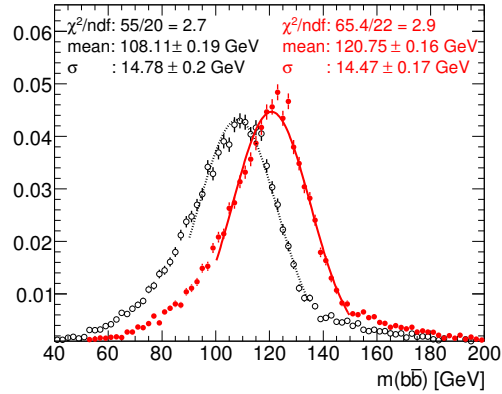
Figure 4.15: Effect of the Monte Carlo based calibration on the Higgs boson mass reconstructed using the true combinations. Red solid (black open) markers and solid (dotted) line show the mass distribution and fitted values for jets after (before) correction. The soft muon correction is applied for both plots.
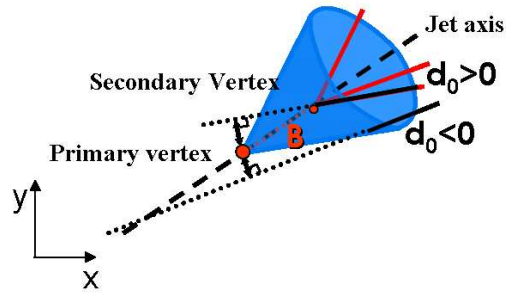

Figure 4.16: Schema representing the secondary vertex and tracks coming from a *B*-meson decay.

from the collision point called primary vertex. These tracks can also be used to reconstruct the *B*-meson decay point called secondary vertex. A *B*-meson decay schema is represented in figure 4.16. We define the impact parameter as the distance of closest approach, in the transverse plane, between the primary vertex and the track. The impact parameter of tracks originated by the *B*-meson child have a relative large value. This property is one of the most important to identify jets originated by a *b*-quark.

In this analysis, *b*-jets are identified using the IP3D+SV1 tagger [1]. The IP3D tagger is based on a likelihood approach combining the transverse and longitudinal impact parameter of tracks inside jets. The SV1 tagger is based on the explicit reconstruction of the secondary vertex. Several properties of the reconstructed secondary vertex are combined in a likelihood:

Treatment	Value (GeV)	No Calibration	Added muons	Calibrated	Both corrections
All b-jets	Mean	5.72±0.05	5.36±0.05	-0.09±0.04	-0.48±0.04
	Sigma	9.98±0.05	9.84±0.05	10.18±0.05	9.97±0.04
b-jets with muons	Mean	26.51±2.57	7.64±0.22	11.37±0.48	2.28±0.17
	Sigma	18.15±1.07	11.79±0.21	13.55±0.35	12.00±0.19
All light jets	Mean	2.43±0.04	2.33±0.04	-1.40±0.04	-1.51±0.04
	Sigma	8.39±0.04	8.37±0.04	8.38±0.04	8.34±0.04
Light-jets with muons	Mean	10.51±0.88	2.35±0.41	7.32±0.67	-0.98±0.39
	Sigma	11.29±0.79	10.92±0.45	11.50±0.61	10.68±0.39

Table 4.5: The true parton p_T minus the measured jet p_T, with and without adding muons and applying the Monte Carlo based correction. The quoted values are the results of a Gaussian fit in the core region ±20 GeV.

- the number of vertices with two tracks that can be formed using the tracks used for this secondary vertex;

- the mass of the secondary vertex;

- the fraction of the secondary vertex energy with respect to the jet that contains it.

Both IP3D and SV1 likelihood outputs are simply summed together to give the so-called IP3D+SV1 weight which will discriminate b-jets. The b-tag weight (W_b) spectra for b-, c-, and light jets in the $t\bar{t}$+jets sample is shown in figure 4.17. A cut on the weight defines which jets will be identified as b-jets. The performance of the tagger is expressed in terms of the rejection of c- or light jets as a function of the efficiency of tagging a b-jet. The rejection is defined as the inverse of an efficiency i.e. a light jet rejection of 100 will mean that for 100 light jets, one is selected as a b-jet.

The rejection of c- and light jets versus the b-jet efficiency, obtained by varying the weight cut, is shown in figure 4.18. The c-jet rejection is much lower than the light-jet rejection because of the lifetime of D-hadrons. Rejections are similar across different samples, with the exception of the light-jet rejection which is higher for the $t\bar{t}$+jets sample. This is expected as this sample contains less b-quark and the light jets contamination by tracks coming from particles with lifetime is relatively small. This effect can be removed by the so-called purification procedure which ignores light and c-jets that are close to b-jets ($\Delta R <0.8$). The effect of the purification is represented in figure 4.19, where all sample perfectly agree.

In this analysis we define a b-jet as a jet having $W_b>6$ and $|\eta| < 2.5$. This cut was optimised to have the best $t\bar{t}H(H \to b\bar{b})$ signal significance while keeping
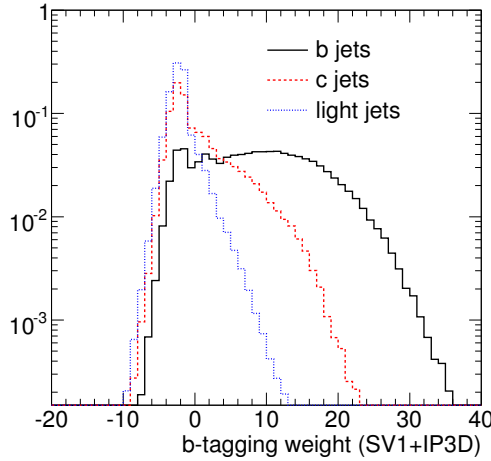
Figure 4.17: Distribution of *b*-tagging weight for *b*-, *c*- and light jets in $t\bar{t}$+jets events, using the IP3D+SV1 tagger.

Sample	*b*-tag efficiency (%)	*c*-jet rejection	light-jet rejection
$t\bar{t}H$	63.1±0.1	6.9±0.1	80±2
$t\bar{t}b\bar{b}$ (QCD)	62.8±0.1	7.1±0.1	99±2
$t\bar{t}b\bar{b}$ (EW)	61.7±0.2	7.2±0.2	103±5
$t\bar{t}$ +jets	62.6±0.1	6.6±0.0	122±1

Table 4.6: *b*-tagging efficiency and *c*- and light-jets rejection for different samples, for the cut used as a working point for this analysis: $W_b > 6$.

a reasonable signal to background ratio. This is shown in figure 4.20 which was done for the cut-based analysis presented in section 4.11.1. The two other analyses have similar behaviour regarding the *b*-tagging cut. The chosen cut leads to the *b*-tagging efficiencies and *c*- and light-jet rejections listed in table 4.6. Four and only four *b*-jets are required in each event. If more than four jets pass the *b*-tagging requirements listed above, only the four jets with the largest *b*-tag weights are considered as *b*-jets. The other jets are considered as light jets and will not be used to reconstruct the top quarks or the Higgs boson.

It is important to mention that in the analysis described in [1], the *b*-tagging performance were intentionally degraded by 30% to simulate the expected effect[3] of residual misalignments that was not included in the simulation. Even if we are using the same samples we will not apply this procedure for two reasons:

- The residual misalignment effects were found to be only 15% [1];

---

[3]This result was based on preliminary studies. Recent studies shows a degradation of 15% only.
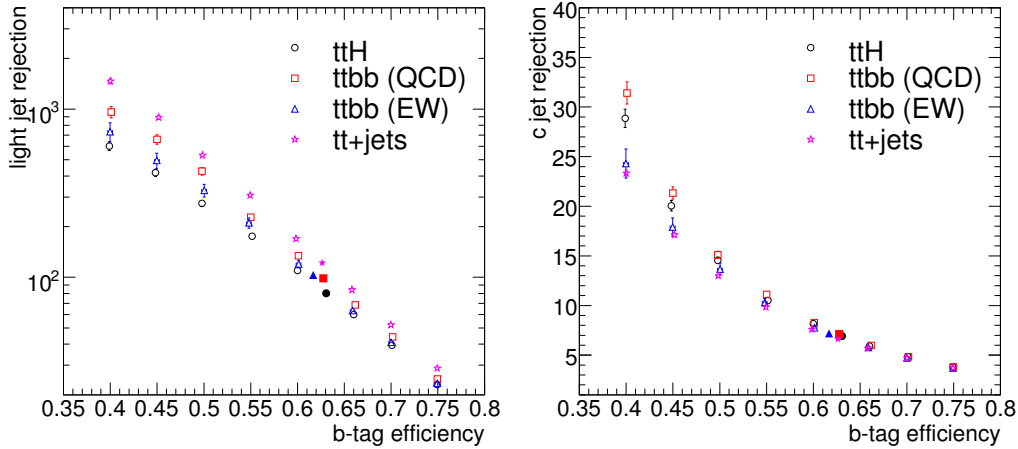
Figure 4.18: Rejection of light and c-jets versus b-tagging efficiency. Solid markers indicate the working point ($W_b > 6$) used for this analysis.

- The latest development in the b-tagging algorithm and especially the track to jet association methods can recover this degradation [1].

4.8.5 Results of pre-selection on signal and background

cut	$t\bar{t}H$	$t\bar{t}b\bar{b}$ (QCD)	$t\bar{t}b\bar{b}$ (EW)	$t\bar{t}$+jets ($\times 10^3$)	$t\bar{t}$+jets AF-II ($\times 10^3$)
trigger	2476±10	83446±331	8717±70	2170±3	-
+lepton	2155±9	73948±312	7673±65	1930±3	1930±0.8
+≥ 6 jets	1369±7	36300±218	4153±48	794±2	906±0.5
+≥ 4b-tags	119 ±2	1294 ±41	182 ±10	0.789±0.06	0.739±0.02

Table 4.7: Number of events for 30 fb^{-1} after each preselection cut for signal and background samples. The errors are statistical only.

The numbers of signal and background events, for 30 fb^{-1} and after each preselection cut, are listed in Table 4.7. The lepton and jet requirements result in a comparable efficiency for signal and background samples. This is expected since all samples are $t\bar{t}$X samples. The main difference comes from b-tagging that reduces the $t\bar{t}$+jets background by a factor of 500 while keeping 10% of the signal events. The efficiency is lower for the $t\bar{t}b\bar{b}$ background compared to the signal even if this background contains 4 b-quark in the final state. This is due to some differences in the p_T and η distributions for b-jets in those samples. The
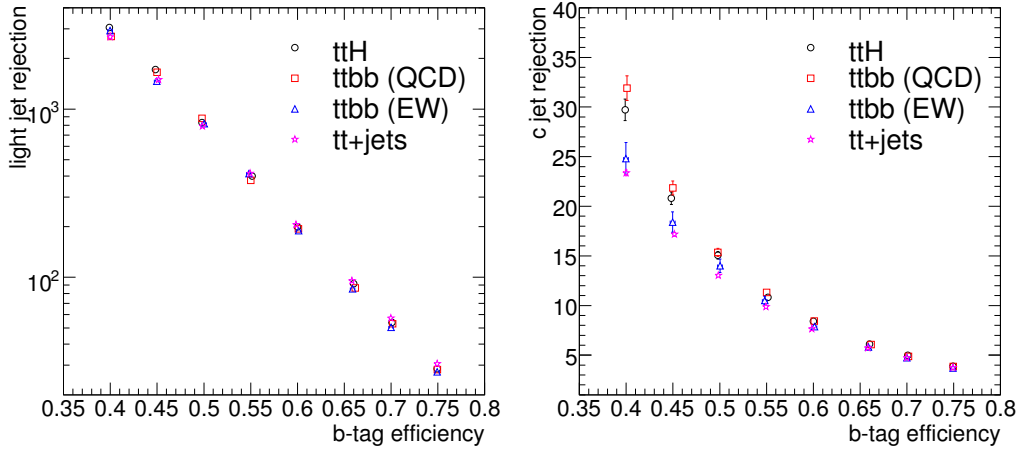
Figure 4.19: Rejection of light and *c*-jets versus *b*-tagging efficiency after applying the purification procedure.

pre-selected sample contains 95.7% of background events including 38% of the irreducible $t\bar{t}b\bar{b}$ background.

The $t\bar{t}$+jets AF-II sample is also listed in table 4.7. The trigger information is not available for this sample. Furthermore an old fast simulation was used for the muon system. This leads to large differences between the $t\bar{t}$+jets and the $t\bar{t}$+jets AF-II samples at the level of lepton preselection. To be able to have a fair comparison, the $t\bar{t}$+jets AF-II sample was normalised to meet the $t\bar{t}$+jets sample at the one lepton cut level. The $t\bar{t}$+jets AF-II sample has a higher efficiency for the jet requirement while the $t\bar{t}$+jets sample is more efficient for the *b*-tagging requirement. This is due to the fact that the mixed simulation is relatively slightly more efficient for low-p_T jets. There is a reasonable agreement between the $t\bar{t}$+jets and the $t\bar{t}$+jets AF-II samples after the cumulated preselection cuts.

4.9 Reconstruction of the leptonically decaying *W* boson

To reconstruct the leptonically decaying *W* boson, we need the neutrino momentum. The fact that the initial transverse energy of the two hard scattering partons is zero allows us to determine the neutrino transverse momentum. This can be done by measuring the imbalance of the transverse energy in the event. This measured quantity is referred to as the missing transverse energy. However, the longitudinal component of the neutrino momentum ($p_{z\nu}$) is not measurable given that the sum of the p_z of the two hard scattering partons is not known.
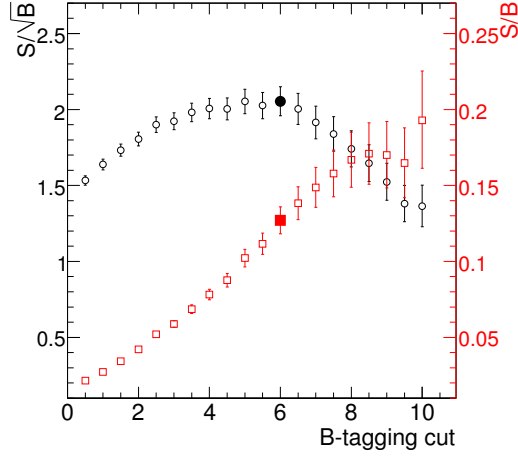
118

Figure 4.20: $S/\sqrt{B}$ and S/B versus the b-tagging cut. S and B are computed for the cut-based analysis for 30 fb^{-1} of data. Solid symbols indicate the chosen cut.

The sum of the lepton and neutrino four-momenta is equal to the W four-momentum. We constrain the mass of the neutrino-lepton system by the true W boson mass. This leads to a quadratic equation with one unknown, $p_{z\nu}$. There are two possible solutions for $p_{z\nu}$:

$$p_{z\nu}^{\pm} = \frac{1}{2} \frac{p_{z\ell}\beta \pm \sqrt{\Delta}}{E_{\ell}^2 - p_{z\ell}^2}$$

with:

$$\beta = M_W^2 - M_{\ell}^2 + 2p_{x\ell}p_{x\nu} + 2p_{y\ell}p_{y\nu}$$

$$\Delta = E_{\ell}^2 \left(\beta^2 + (2p_{z\ell}p_{T\nu})^2 - (2E_{\ell}p_{T\nu})^2 \right)$$

The transverse missing energy measurement is limited by several factors e.g. jet resolution, underlying event. Therefore the quadratic equation does not have a real solution for a significant fraction of events (28% for the $t\bar{t}H$ sample). In this case two approximations are considered:

- The "$\Delta = 0$ approximation": this is done by considering the discriminant of the quadratic equation to be zero. This is equivalent to dropping the imaginary part of the complex solutions;

- The "collinear approximation": this is done by assuming that $p_{z\ell} = p_{z\nu}$. In fact the W boson is boosted due to the large top quark mass so that the neutrino and the lepton are produced preferentially in the same direction which corresponds to the W direction.
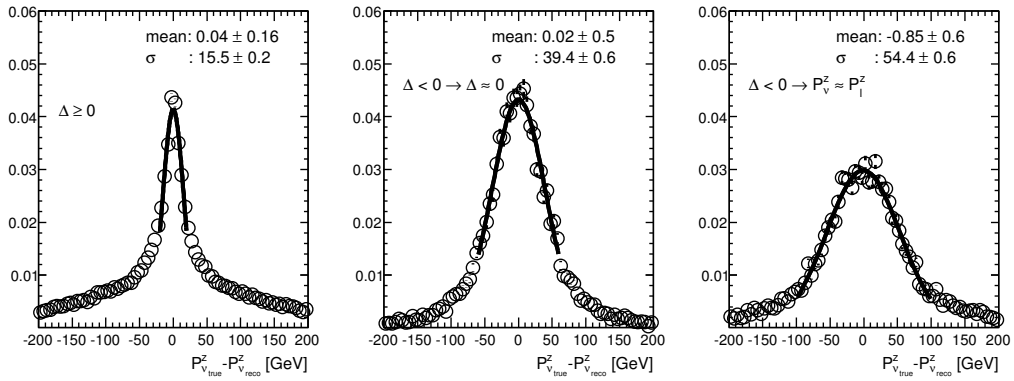
119

Figure 4.21: Neutrino p_z resolution when there are real solutions (left plot), or when there is no solution and the $\Delta = 0$ solution is used (middle plot) or the collinear approximation is used (right plot).
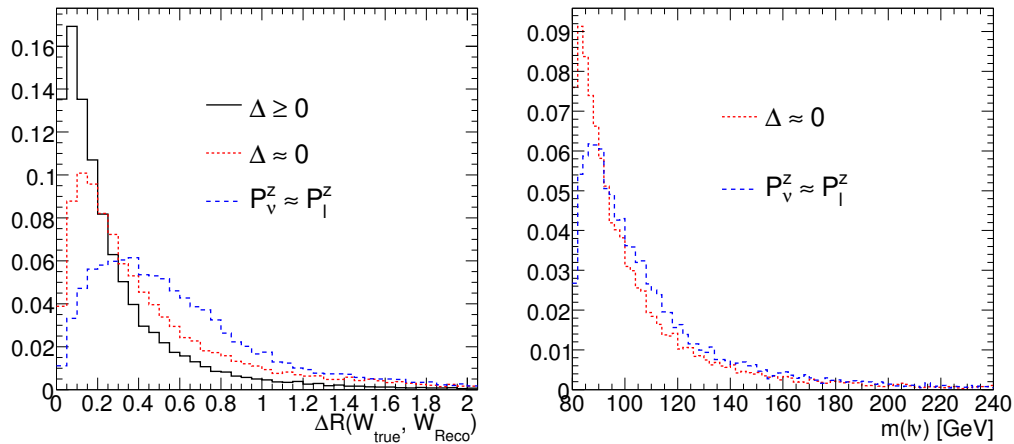

Figure 4.22: Distributions of ΔR between the true and the reconstructed leptonic W boson (left) and of the leptonic W mass (right) for events where a solution for p_z is found (solid black line) and events where there is no solution and the $\Delta = 0$ solution is used (dotted red) or the collinear approximation is used (dashed blue).

120

In the $t\bar{t}H$ events, 72% of the time $p_{z\nu}$ has real solutions considering all events after the lepton pre-selection. In this case two W bosons are reconstructed and the choice between the two is made while reconstructing the top quarks. Figure 4.21 shows the $p_{z\nu}$ resolution. The central resolution is 15.5 GeV for events with real solutions. However, for these events the resolution has a very large tail corresponding to the other neutrino solution that does not describe well the true $p_{z\nu}$ value. For the 28% of the cases in which there is no solution, choosing $\Delta = 0$ leads to a better resolution of 39.4 GeV compared to 54.4 GeV for the collinear approximation. A comparison between the true generated W boson and the reconstructed W boson can be seen in Figure 4.22. The direction is better reconstructed in the case where the real solution exist. For both considered approximations, the constraint on the W boson mass is lost and the mass of the lepton-neutrino system is always higher than the real W boson mass. The mass is better described by the $\Delta = 0$ approximation which will be used for the top reconstruction for events with no $p_{z\nu}$ real solutions. A loose upper cut of 140 GeV is applied on the corresponding reconstructed W mass. This cut removes about 3% of the events in all samples.

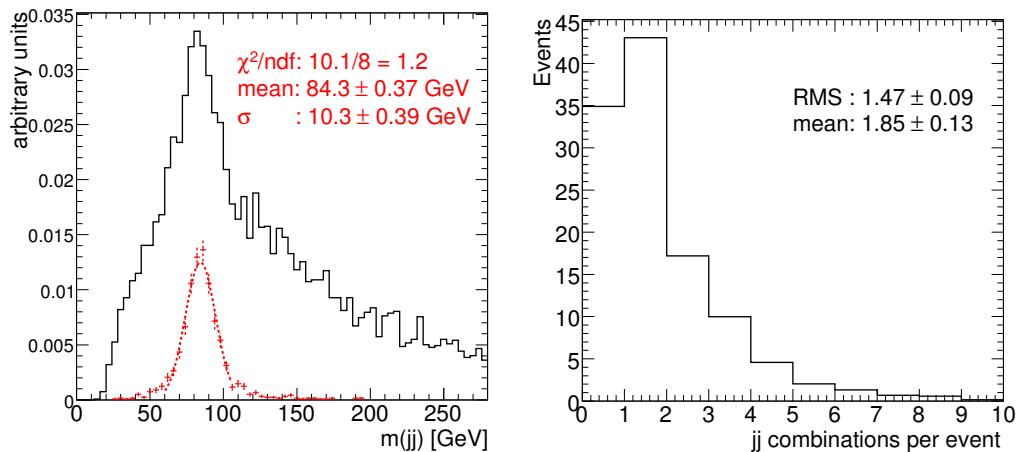## 4.10   Reconstruction of the hadronically decaying W boson

Figure 4.23: (left) Invariant mass spectrum for hadronically decaying W candidates. The dotted line shows combinations where the jets forming the W are correctly assigned. (right) Number of hadronic W combinations per event for candidates within 25 GeV of the true W mass in the signal sample for 30 fb^{-1} .

The hadronic W is reconstructed using all combinations of 2 jets that are not considered as b-jets in the preselection. Figure 4.23 shows the mass distribution of all W candidates. For the cut-based analysis, described in section 4.11.1, only candidates within 25 GeV from the true W mass are kept. The number of candidates after this cut is represented in figure 4.23. We can see that a large number of events have more than on reconstructed W boson. This will complicate furthermore the reconstruction of the top quarks. For the likelihood and BDT analyses described in section 4.11.2, there is no explicit cut on the W mass. The mass is considered as a discriminating variable for these two analyses and thus the cut is implicit.

4.11 Top-quark pair reconstruction

The top quarks are reconstructed by associating a W boson to a b-jet. Several combinations are possible and only one combination[4] should be chosen in order to be able to select the two remaining b-jets to make the Higgs boson. The combination resulting in the best reconstruction for the top candidates is chosen. Three different methods will be considered for the combinatorial solving: the cut-based, the likelihood and the BDT analysis. In all cases, before computing the top-quark four-momentum, the W four-momentum is rescaled so that the reconstructed W invariant mass corresponds to the mass of the W boson.

4.11.1 The cut-based approach

From all possible combinations of W bosons and b-jets, the one that minimises a χ^2 based on the top quark mass is chosen. The χ^2 is expressed as:

$$\chi^2 = \left(\frac{m_{jjb} - m_{top}}{\sigma_{m_{jjb}}} \right)^2 + \left(\frac{m_{l\nu b} - m_{top}}{\sigma_{m_{l\nu b}}} \right)^2,$$

where $\sigma_{m_{jjb}}$ and $\sigma_{m_{l\nu b}}$ are the mass resolutions estimated using the true combinations from signal events. Their respective values are: $\sigma_{m_{jjb}}$=12 GeV and $\sigma_{m_{l\nu b}}$= 19 GeV. The best combination is then required to fulfil $|m_{jjb} - m_{top}| < 25$ GeV and $|m_{l\nu b} - m_{top}| < 25$ GeV. The top quark mass distributions for the chosen combination in the signal sample is shown in figure 4.24. The resolution on the reconstructed top is better than the one from the true combinations. This is expected as the χ^2, by construction, biases toward a better resolution. Therefore bad

---

[4]One should note that several combinations can be selected with different weights but an attempt to do this lead to worse results.
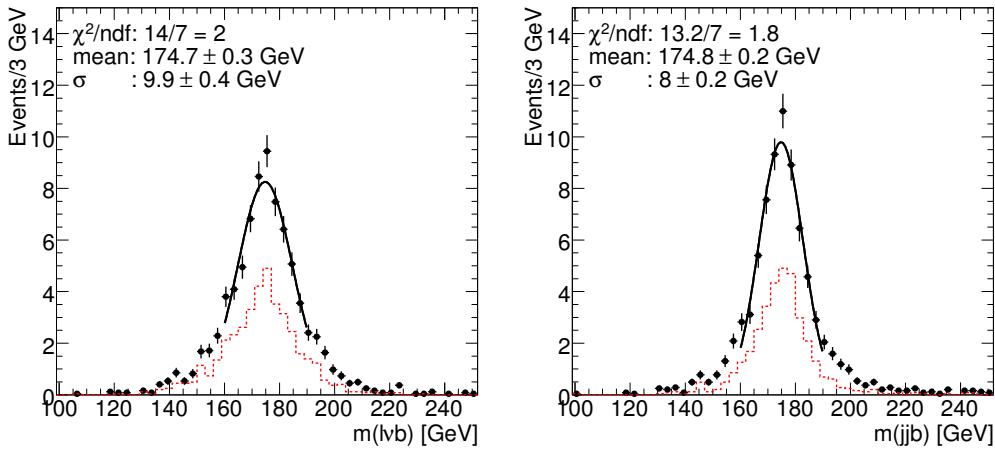
Figure 4.24: Reconstructed invariant mass spectrum for top-quark selected candidates in the signal sample. The dotted red line indicates the candidates for which the b-jets are correctly assigned.

combinations which have a reconstructed top mass closer to the true top mass are selected.

4.11.2 The multivariate approaches

To achieve a better signal efficiency and purity, two different multivariate approaches are tested as an alternative to the χ^2 approach to reconstruct the $t\bar{t}$ system.

The likelihood approach Six variables, depending only on the top-quark pair system, are combined in a likelihood function. The variables used, shown in Figure 4.25 are:

- m_{jj}: invariant mass of the light jets from the hadronic W decay;

- $\angle(j,j)$: angle between the light jets from the hadronic W decay;

- m_{jjb}: invariant mass of the hadronic top decay products;

- $\Delta R(jj,b)$: ΔR between the reconstructed hadronic W decay and the b-jets from the hadronic top;

- $m_{\ell\nu b}$: invariant mass of the leptonic top decay products;

- $\Delta R(\ell,b)$: ΔR between the lepton and the b-jets from the leptonic top.
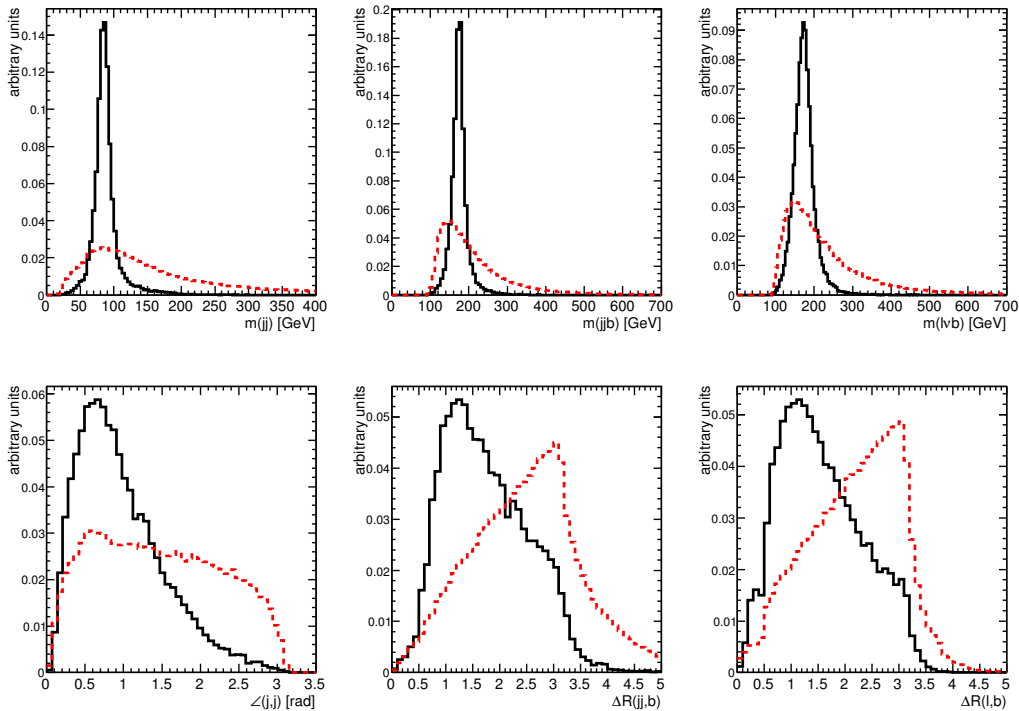
123

Figure 4.25: Combinatorial likelihood templates derived from the $t\bar{t}H$ signal sample. Solid lines correspond to the correct combinations while the dashed lines show the combinatorial background.

Due to the lack of statistics, the b-tagging cut was removed before building the likelihood templates. Instead, the truth labelling was used to determine the jet flavors.

While building the templates, the correct combinations are treated separately for each variable e.g. m_{jj} is considered correct if both jets used for the hadronic W reconstruction match the true partons from the generated W boson. This is done without looking at the other objects in the event. If the correct combination does not exist, for a given event and for a given variable, all the corresponding combinations are excluded.

The boosted decision-tree approach The likelihood function does not take into account the correlations between variables. However the angles and masses used previously are correlated. We choose a BDT to be able to take into account these correlations. A decision tree (DT) is a machine learning algorithm based on the recursive growth of a tree-like diagram where at each node a decision is made: the node is a signal leaf node or it is a background leaf node or additional cuts
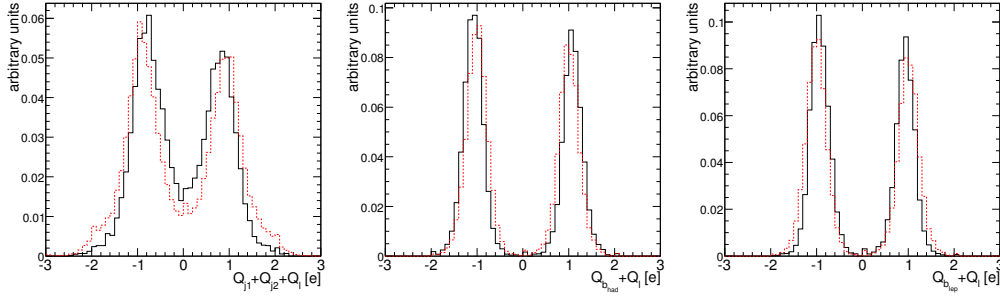
Figure 4.26: Variables based on the jet charge (see text) and used as inputs for the BDT classifier.

are required to split furthermore the sample at the considered node. A DT is frequently subject to overtraining. An efficient way to reduce this effect, while increasing the separation power, is to use a sort of a weighted average of several DTs. This is the so called boosting procedure and the resulting classifier is called a boosted decision-tree.

For the BDT, we use the same variables used for the likelihood technique. Moreover, we add seven new variables to help improving the purity. Three of these variables are computed using the jet charge. This charge is constructed using the tracks in each jet in order to have an estimation of the original quark charge. The charge (Q_{jet}) is defined as following:

$$Q_{jet} = \frac{\sum p_{T\,track}^{\alpha} \times Q_{track}}{\sum p_{T\,track}^{\alpha}} \text{ where } track \in jet$$

α is chosen to be 0.75 as this value gives the best performance.
The following variables, built using the jet charge information and represented in figure 4.26, are chosen:

- $Q_{j1} + Q_{j2} + Q_{\ell}$: the sum of the charges of the two jets from the hadronic W and the lepton charge;

- $Q_{b_{had}} + Q_{\ell}$: the sum of the charge of the b-jet from the hadronic top and the lepton charge;

- $Q_{b_{lep}} + Q_{\ell}$: the sum of the charge of the b-jet from the leptonic top and the lepton charge.

The four other additional variables deal with the structure of the event. The following variables, represented in figure 4.27, are considered:

- $m(\ell\nu b_{had})$: invariant mass of the leptonic W and the b-jets used for the hadronic top reconstruction;
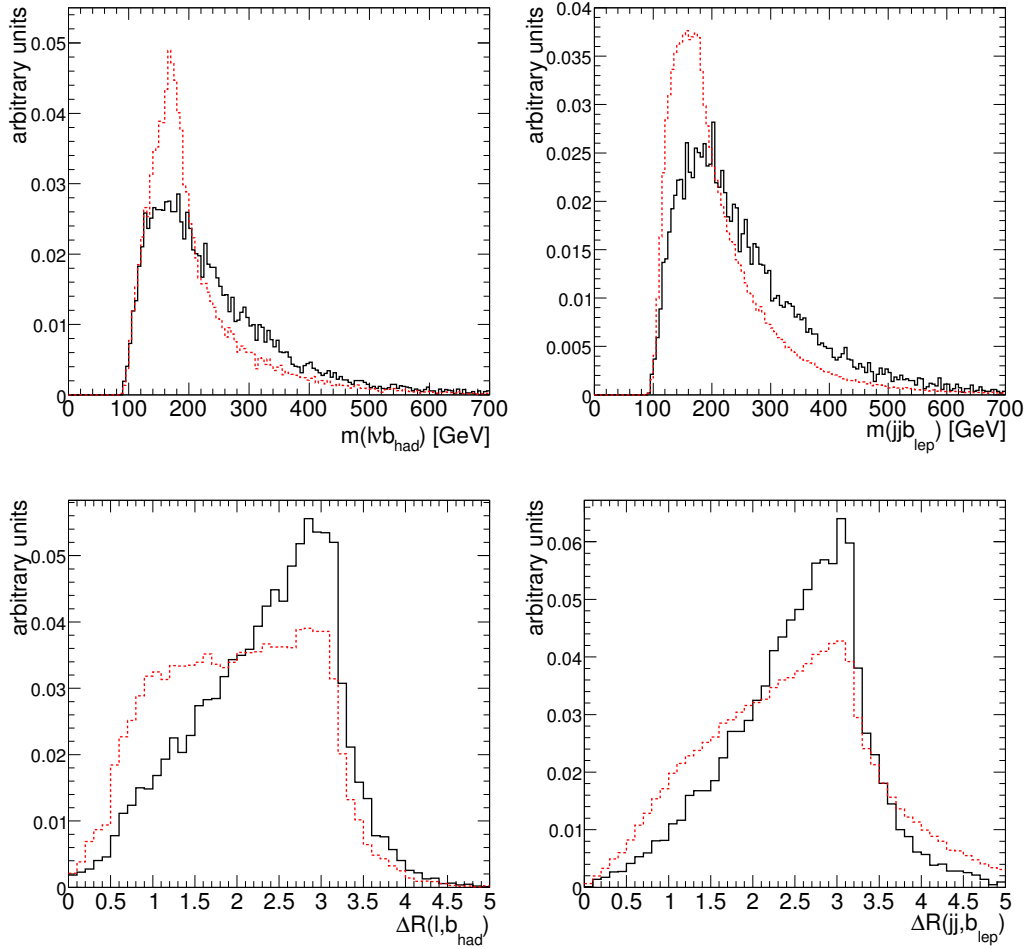
125

Figure 4.27: Additional kinematic variables used as inputs for the BDT classifier.

- $m(jjb_{lep})$: invariant mass of the hadronic W and the b-jets used for the leptonic top reconstruction;

- $\Delta R(\ell, b_{had})$: ΔR between the lepton and the b-jets from the hadronic top;

- $\Delta R(jj, b_{lep})$: ΔR between the hadronic W and the b-jets from the leptonic top.

When training a classifier, the signal and combinatorial background are treated as totally independent. The correlation between combinations in the same event are not taken into account i.e. for a given combination, the classifier is not aware of the properties of the other combinations, however during the reconstruction the combinations are compared and only one is chosen. To be able to partially take this effect into account, the four new variables listed above are used.
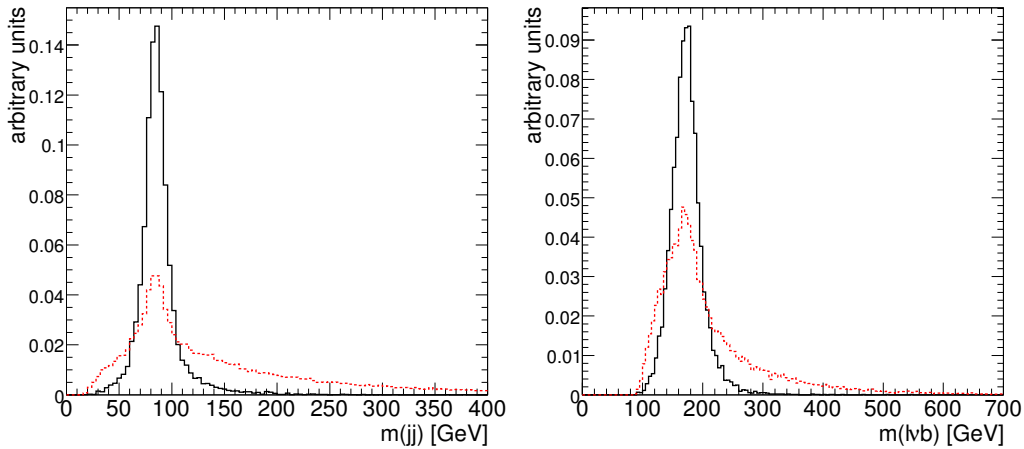
Figure 4.28: Correct and wrong combinations, for two variables, used as inputs for the BDT classifier. The contamination of signal-like combinations, due to the way the correct combination is defined, is clear for both variables. This is to be compared to the same distributions used for the likelihood classifier in figure 4.25.

For the BDT, correct combination means that all the components of the $t\bar{t}$ system are correctly chosen in the event. Treating variables separately is not possible since the BDT takes into account the correlations. This will imply a contamination of the background distributions for each variable by signal-like combinations e.g. if only one of the jets used for the hadronic W reconstruction is not correctly assigned while the b-jet used for the leptonic top is, $m(\ell\nu b)$ will be called a bad combination even if it is correct. This decreases the separation power of each individual variable. This is shown in figure 4.28 for the invariant mass of the hadronic W and the leptonic top[5].

As for the likelihood, the true labelling is used to determine the flavor of a jet. However the statistics is still low, especially for correct combinations that requires the presence of a correctly identified lepton and four jets from the $t\bar{t}$ system. This latter requirement has a low efficiency after the identification and the acceptance cuts at the preselection level. Events with no correct combination are discarded.

The TMVA [63] implementation of the BDT is used. Most of the parameters corresponds to the TMVA default. However, some parameters were tuned to suppress any over-training which is common for BDTs. The over-training is controlled by comparing the BDT output for the trained sample with an independent test sample as shown in figure 4.29. Both samples are compatible with only a small over-training in the tails of the combinatorial background distribution.

---

[5]Note that an attempt to weight the combinations by their "correctness" did not improve the results.

Variable	Relative importance
m_{jj}	2.3×10^{-1}
m_{jjb}	2.1×10^{-1}
$m(jjb_{lep})$	1.2×10^{-1}
$m_{\ell\nu b}$	1.1×10^{-1}
$\Delta R(jj, b)$	6.7×10^{-2}
$m(\ell\nu b_{had})$	5.7×10^{-2}
$\angle(j, j)$	3.8×10^{-2}
$Q_{b_{lep}} + Q_\ell$	3.7×10^{-2}
$Q_{j1} + Q_{j2} + Q_\ell$	3.1×10^{-2}
$Q_{b_{had}} + Q_\ell$	2.9×10^{-2}
$\Delta R(\ell, b)$	2.4×10^{-2}
$\Delta R(jj, b_{lep})$	2.3×10^{-2}
$\Delta R(\ell, b_{had})$	2.1×10^{-2}

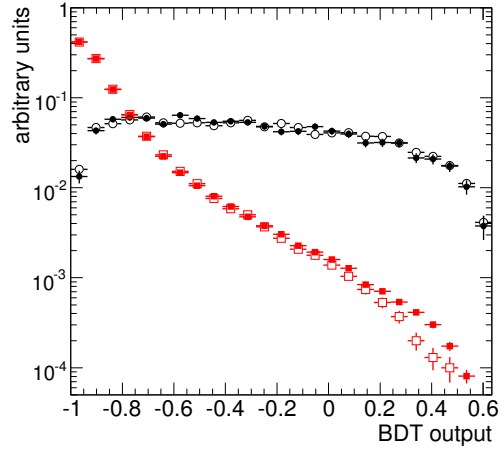Table 4.8: BDT variables ranking, ordered by decreasing discrimination power.

Figure 4.29: BDT output for the signal (black circles) and for the combinatorial background (red squares). The sample used for training the BDT (solid markers) is compared with a separated test sample (open markers)

TMVA provides a ranking of the input variables. This ranking is based on the number of leafs using a given variable, weighted by the separation power of this variable at the corresponding leaf [64]. Table 4.8 shows the ranking for each of the variables used in the BDT.

Results The output of the pairing likelihood and of the BDT for the correct and wrong top quark combinations are shown in figure 4.30. The likelihood has a good separation power: the signal has a large peak at one and the background at zero. However, the large number of wrong combinations compensate the low probability of selecting these combinations. This is also true for the BDT output distribution.

For each event we only use the combination which maximises the corresponding classifier output. An additional cut on the classifier output is applied to insure the selection of well-reconstructed events. This cut is optimised using a simple estimation of the significance, computed as $S/\sqrt{B}$, while keeping S/B and the number of signal events at reasonable values. S and B are computed after requiring that the reconstructed Higgs boson mass is in a range of ± 30 GeV around the generated Higgs boson mass of 120 GeV and for 30 fb^{-1} of data. The significance and the signal to background ratio versus the number of signal events, computed by varying the cut on the corresponding classifier output, is represented in figure
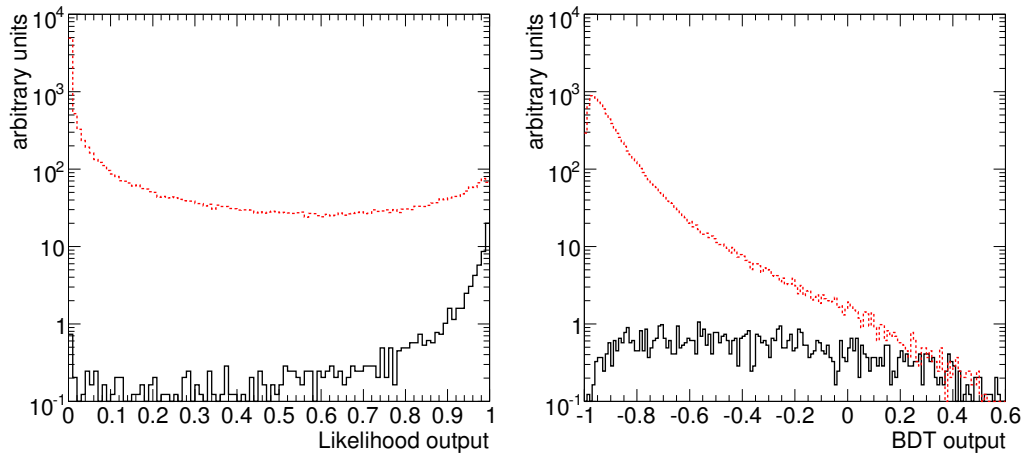
Figure 4.30: Combinatorial likelihood and BDT output for $t\bar{t}H$ events. Black solid (red dotted) histogram indicates the correct (wrong) combinations.
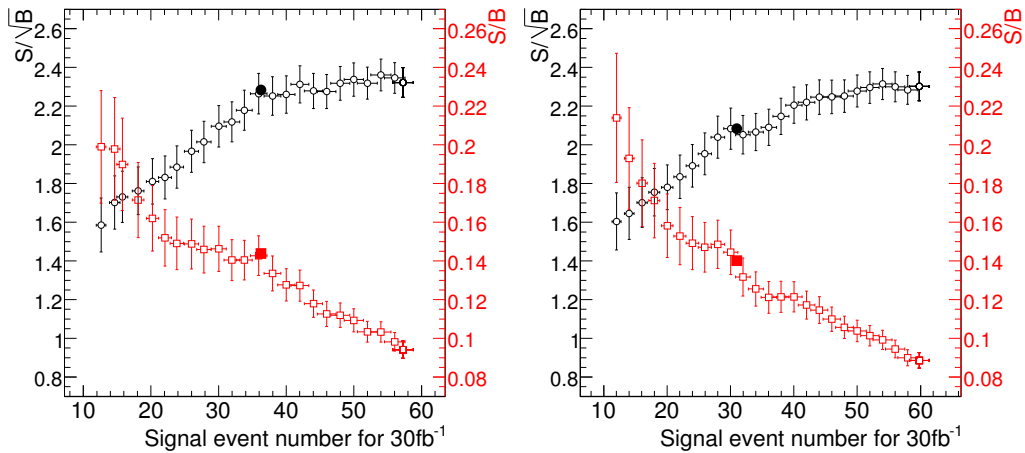

Figure 4.31: $S/\sqrt{B}$ and S/B vs the number of signal events for 30 fb^{-1} after all selection cuts. Solid markers indicates the chosen cut (Likelihood>0.95, BDT>-0.4).

4.31 for both the likelihood and BDT analyses. The values corresponding to the chosen cuts of 0.95, for the likelihood, and -0.4, for the BDT, are also represented.
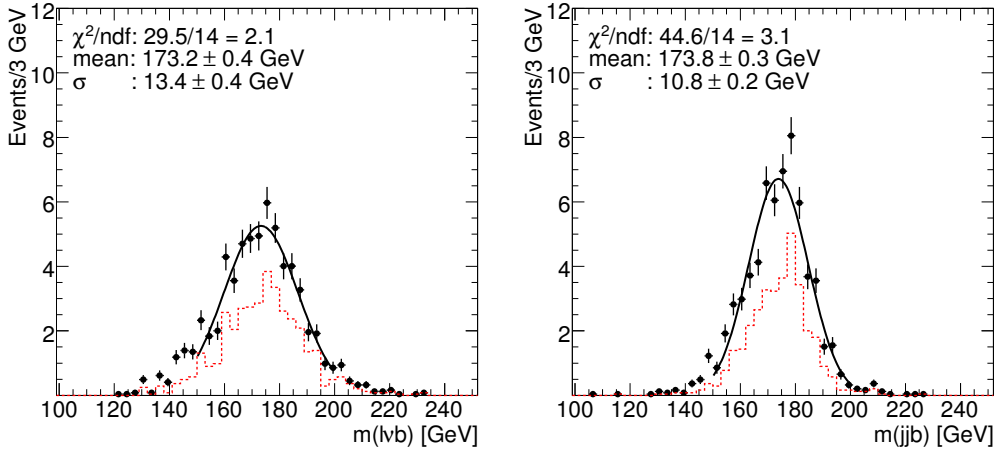

Figure 4.32: On the left-hand (right-hand) side is shown the reconstructed invariant mass for the leptonic (hadronic) top quark candidates, using the maximum-likelihood configuration, after applying a cut on the likelihood output. The dotted histogram indicates the correct combinations.

The reconstructed top quark masses, after the likelihood (BDT) cut, are shown in Figure 4.32 (4.33). The purity of the b-jets, used for the top quark reconstruction, vs the signal efficiency is compared for the three reconstruction methods in figure 4.34. The purity improvement brought by the likelihood and the BDT is clear, compared to the cut based-analysis. The BDT performs much better than the likelihood for the leptonic top while for the hadronic top both multivariate techniques are comparable. Thanks to the better purity, the reconstructed mass resolutions also agree better with the distributions for the true good combinations.

4.12 Higgs boson reconstruction

The Higgs boson is reconstructed using the two b-jets that are left after the two top quark reconstruction. The Higgs boson purity vs the signal efficiency, for all three methods, is represented on figure 4.35. Both multivariate techniques perform better than the cut-based analysis with a slight improvement for the BDT compared to the likelihood.

The reconstructed Higgs boson masses for the signal sample, using all three methods, are shown in figures 4.36. As expected, the core resolution is improving with the purity. However the purity is still very low and the signal $b\bar{b}$ mass
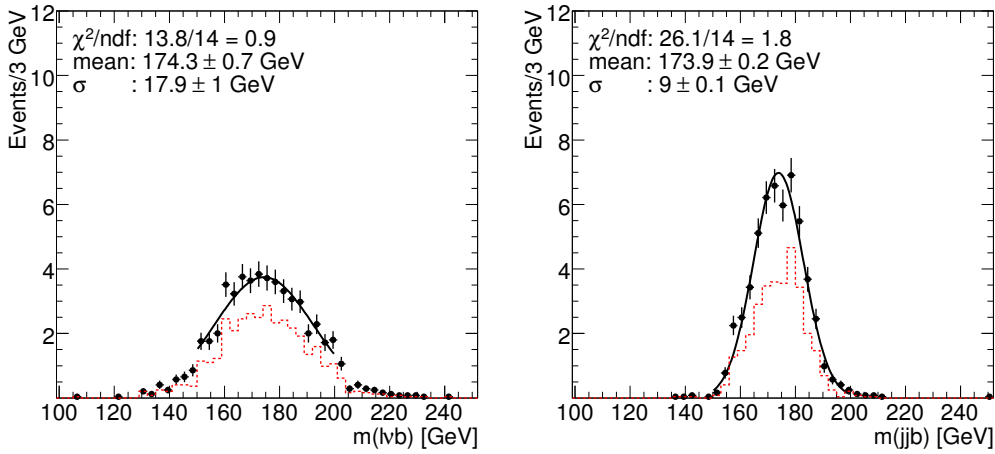
Figure 4.33: On the left-hand (right-hand) side is shown the reconstructed invariant mass for the leptonic (hadronic) top quark candidates, using the BDT configuration, after applying a cut on the BDT output. The dotted histogram indicates the correct combinations.
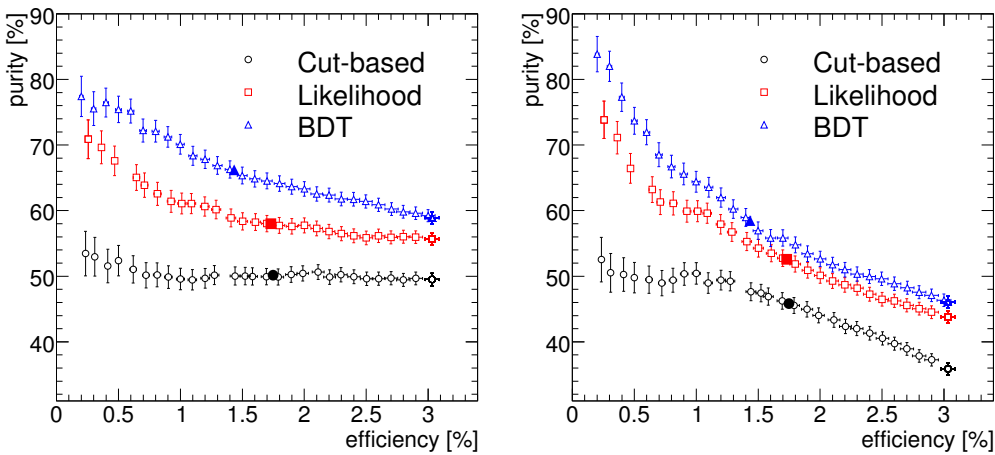

Figure 4.34: Purity of the b-jet used for the reconstruction of the leptonic/hadronic top (left/right) vs the signal selection efficiency. The chosen working points are shown as solid markers.
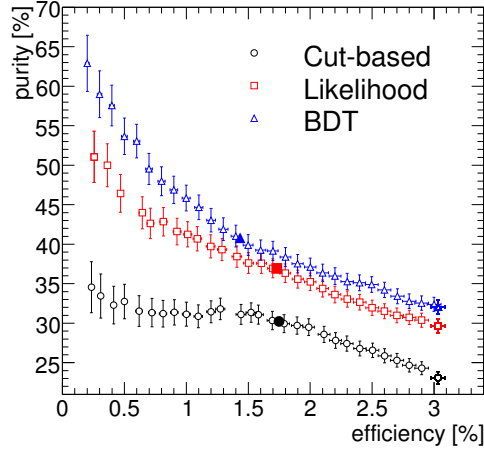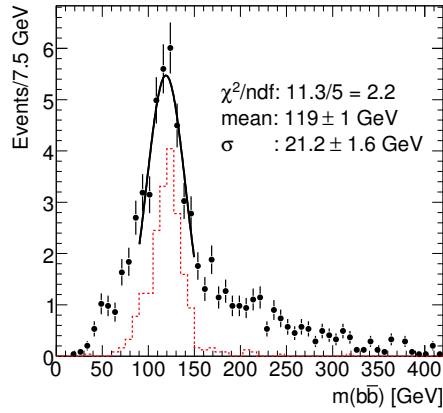
Figure 4.35: Purity of the reconstructed Higgs boson vs the signal selection efficiency. The chosen working points are shown as solid markers.

cut	$t\bar{t}H$	$t\bar{t}bb$ (QCD)	$t\bar{t}bb$ (EW)	$t\bar{t}$+jets	$t\bar{t}$+jets AF-II
Cut-based					
$55 < m_{jj} < 105$ GeV	80 ± 2	800 ± 32	122 ± 8	336 ± 40	341 ± 11
$+150 < m_t < 200$ GeV	66 ± 2	653 ± 29	93 ± 7	210 ± 31	247 ± 10
$+90 < m_{b\bar{b}} < 150$ GeV	33 ± 1	158 ± 14	25 ± 4	70^{+23}_{-18}	79 ± 5
Likelihood					
best output > 0.9	65 ± 2	589 ± 27	95 ± 7	187 ± 30	209 ± 9
$+90 < m_{b\bar{b}} < 150$ GeV	36 ± 1	163 ± 15	26 ± 4	70^{+23}_{-18}	63 ± 5
BDT					
best output > -0.4	54 ± 1	507 ± 26	83 ± 7	154 ± 27	167 ± 8
$+90 < m_{b\bar{b}} < 150$ GeV	31 ± 1	152 ± 14	22 ± 4	14^{+14}_{-8}	45 ± 4

Table 4.9: Number of events after each selection cut for signal and backgrounds for 30 fb^{-1} . Errors are statistical only.

	Cut-based	Likelihood	BDT
b-jet from Leptonic top is correct	50.2 ± 0.1 %	57.9 ± 0.1 %	66.3 ± 0.1 %
b-jet from Hadronic top is correct	45.9 ± 0.1 %	52.7 ± 0.1 %	58.5 ± 0.1 %
Both b-jets from Higgs are correct	30.2 ± 0.1 %	36.9 ± 0.1 %	40.8 ± 0.1 %
$m_{b\bar{b}}$ peak resolution, GeV	21.2 ± 1.6	18.0 ± 0.9	17.9 ± 1.0
Fraction $\mid m_{b\bar{b}} - m_H \mid < 30$ GeV	50.3 ± 1.2 %	55.5 ± 1.2 %	57.0 ± 1.4 %
Signal to background ratio	12.6 ± 0.9 %	14.3 ± 0.9 %	14.0 ± 1 %
s/$\sqrt{b}$	2.1	2.3	2.1

Table 4.10: Summary of the signal reconstruction properties and the significance estimate for all three reconstruction methods.

(a) Cut-based analysis
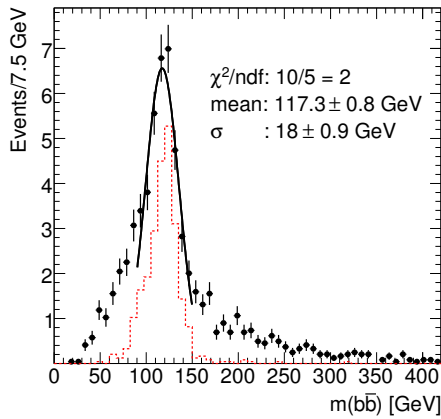
(b) Likelihood analysis
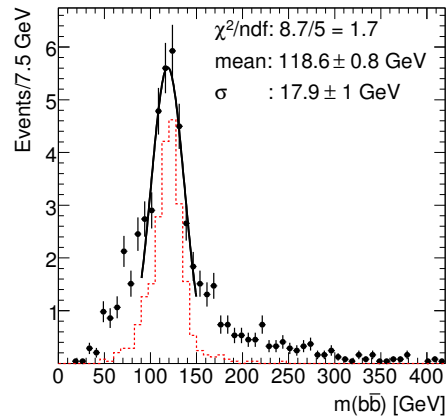
(c) BDT analysis

Figure 4.36: The reconstructed Higgs boson mass for the signal sample normalised to 30fb^{-1} . The correctly reconstructed Higgs bosons are shown in red dashed lines.
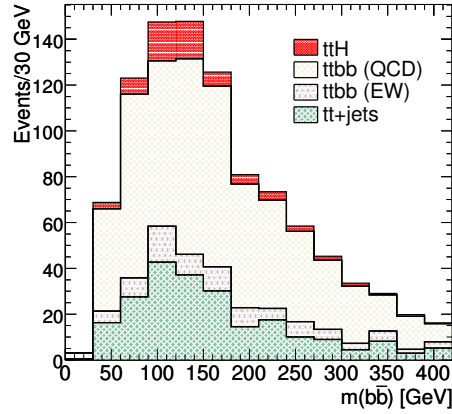
(a) Cut-based analysis
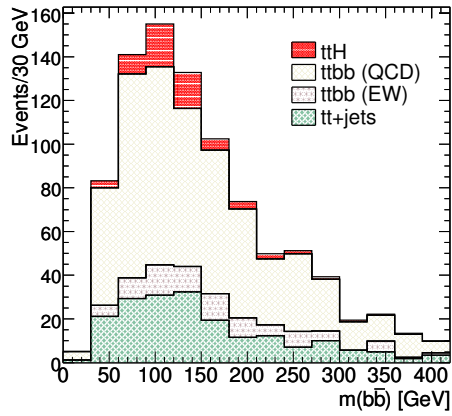
(b) Likelihood analysis
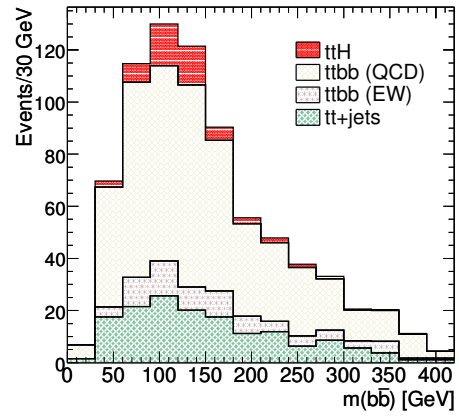
(c) BDT analysis

Figure 4.37: The combined $b\bar{b}$ mass for the signal and background samples normalised to 30fb^{-1}.

spectrum presents very large tails. These tails decrease slightly for the multivariate techniques that have a better purity. This can be seen in table 4.10 in which the resolution and the fraction of events, in a mass range of ±30 GeV around the generated Higgs boson mass, are listed.

The number of events, for 30 fb^{-1}, after each selection cut is represented in table 4.9 for all reconstruction methods. The $t\bar{t}$+jets sample suffers from very large statistical errors. However the larger $t\bar{t}$+jets AF-II sample perfectly match, within errors, with the $t\bar{t}$+jets sample and thus it is used for the combined m$_{b\bar{b}}$ spectrum presented in figure 4.37. We compute the significance in a mass range of ±30 GeV around the generated Higgs boson mass. This results in the signal to background (S/B) and a significance (S/$\sqrt{B}$) listed in table 4.10.

It is clear that the extraction of a signal peak on top of the background distribution is very difficult. One may need a precise knowledge of the background shape and normalisation which are not necessarily trustworthy in the Monte Carlo simulation. A method to extract the background from data is mandatory to be able to extract the $t\bar{t}H(H \rightarrow b\bar{b})$ signal.

4.13   Signal purity

The signal purity is of major importance in this analysis. The reconstructed Higgs mass distribution has very large tails and a wide core resolution as seen before. Only 50% of the signal events are present in the mass range of ±30 GeV used to compute the significance. Improving the purity is a straightforward way to recover signal events from the tails and thus improve the significance. Higher purity would also lead to a clearer signal peak on top of the physical background, leading to an easier extraction of signal with sideband subtraction. Furthermore, the large combinatorial background in the signal, for both top quarks and the Higgs boson, dilute kinematics differences between the $t\bar{t}$+jets background and the $t\bar{t}H(H \rightarrow b\bar{b})$ signal. Consequently, an optional selection likelihood aimed at reducing the background, especially the irreducible $t\bar{t}b\bar{b}$ background, will not bring a significant improvement.

There is no large difference in purity for the three different reconstruction methods described before. The likelihood method will be considered in the following to study in details the origin of the low purity on the signal reconstruction.

4.13.1   Maximal achievable purity after preselection

The origin of the wrong association of jets can be separated into two categories:

- the correct combination does not exist and therefore can not be found by the likelihood. This happens for events where some jets originating from the

135

truth match found for	Identified & selected	correctly tagged	correct combination chosen
2 b-quarks from Higgs	90%	80%	30%
2 b-quarks from $t\bar{t}$	92%	83%	28%
4 b-quarks from $t\bar{t}H$	83%	65%	24%
2 partons from W	56%	39%	31%
All partons from $t\bar{t}H$	45%	34%	13%

Table 4.11: Fraction of events, that pass the preselection cuts, with the corresponding truth information. The first column corresponds to the maximum achievable purity assuming perfect identification, selection and perfect b-tagging. The second corresponds to the maximum achievable purity with the current b-tagging performance. The last column shows the purity achieved by the likelihood analysis before any cut on the likelihood output.

considered true partons are not identified or are removed by the different selection cuts. It is clear that the maximum purity is limited by the fraction of events of this type;

- the wrong association is due to the likelihood. This happens for events where jets stemming from the considered true partons are identified, selected and correctly b-tagged. We will call "event with perfect preselection" an event where all jets originating from the six quarks in the $t\bar{t}H$ system are identified, selected and correctly b-tagged.

Table 4.11 shows the fraction of events, with respect to the number of preselected events, with different truth matching configurations. The lepton purity is not considered as the lepton is correctly selected in 99% of the cases and does not have any significant effect for this analysis.
The b-jets from $H{\rightarrow}b\bar{b}$ and from the top quarks are present in the preselected jet collection in about 83% of the events, and are b-tagged in 65% of the events. The two jets corresponding to the partons from the W boson are present in 56% of the events. For 70% of these events, the correct flavor of the W boson jets is chosen by the b-tagging procedure. The other 30% are mainly due to the presence of c-jets from the hadronic W decay in half of the events. Finally, in 45% of the events all jets from the quarks in the $t\bar{t}H$ system are selected, the b-tagging is correct in 34% of the cases. However the likelihood correctly assigns all the 6 jets in only about a third of these events. All of this points to a large problem in solving the combinatorics of the four b-jets. The situation is slightly better for solving the hadronic W combinatorics. However the preselection is cutting a large number of jets coming from the W boson decay. In about 10% of the preselected events, a light jet mistagged as a b-jet replaces one of the jets from the Higgs boson decay

in the list of 4 b-jets. We will try in the following to decouple different factors that leads to such a low purity.
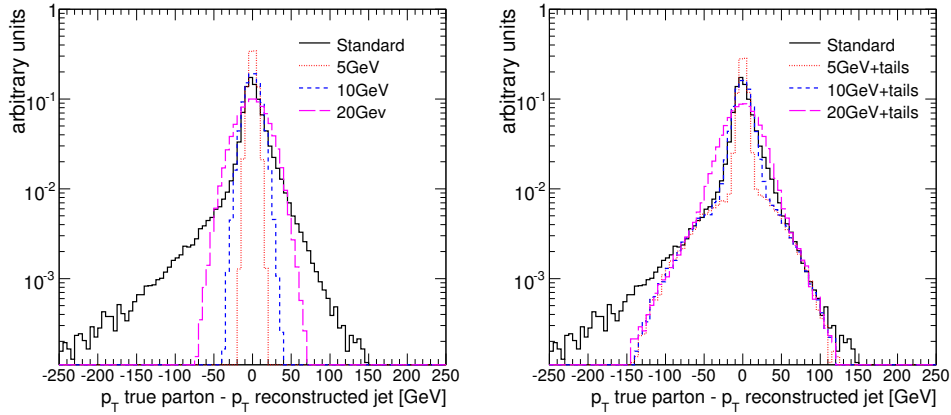
4.13.2 Jet resolution effects

All three methods of reconstruction rely mainly on the hadronic W boson and the top quarks masses to determine the best combination. The resolution on the jet momentum is important for a better separation between right and wrong combinations. To quantify the effect of the jet resolution on the purity, the jet four-momenta were replaced by the original quark momenta. The momentum was then smeared to simulate three different scenarios with a jet p_T resolution corresponding to 5, 10 and 20 GeV. The middle choice correspond to the actual jet p_T resolution as seen in table 4.5. The other two choices correspond to the extreme scenarios where the jet p_T resolution is twice better or twice worse. These three scenarios were duplicated adding a resolution of 50 GeV for 20% of the jets for a rough simulation of the effects from tails. The three scenarios, without and with the tails, are represented respectively in figures 4.38(a) and 4.38(b). The resolution from the actual jet reconstruction is also plotted on both figures for comparison. The scenario with 10 GeV resolution with the additional tails represents better the true reconstructed jet resolution.

The likelihood templates and the full reconstruction were redone for all these scenarios. The effect on the purity is shown in figure 4.38(c). The hadronic top has the highest sensitivity to the resolution as it is reconstructed using three jets. However the purity difference for the best scenario (5 GeV) and the worst scenario (20 GeV+tails) is less than 10%. The effect is smaller for the Higgs boson and negligible for the leptonic top. In order to isolate the resolution effect, the purity considering only events with a perfect preselection is also shown. Considering the hadronic top, the effect is much larger for these events with an absolute change of purity of at most $\pm14\%$ with respect to the actual standard jet reconstruction. The effect is of about $\pm10\%$ for the Higgs boson and about $\pm4\%$ for the leptonic top. Therefore all the relative changes of purity are not very large, even considering these extreme scenarios.

A similar study was performed for the resolution on the missing transverse energy. The effect is very small (4%) on the leptonic top purity and negligible for the hadronic top and the Higgs boson purity.

We conclude that the jet (and the transverse missing energy) resolution is not a significant source of problems impacting the reconstruction purity.

(a) Jet resolution

(b) Jet resolution with tails
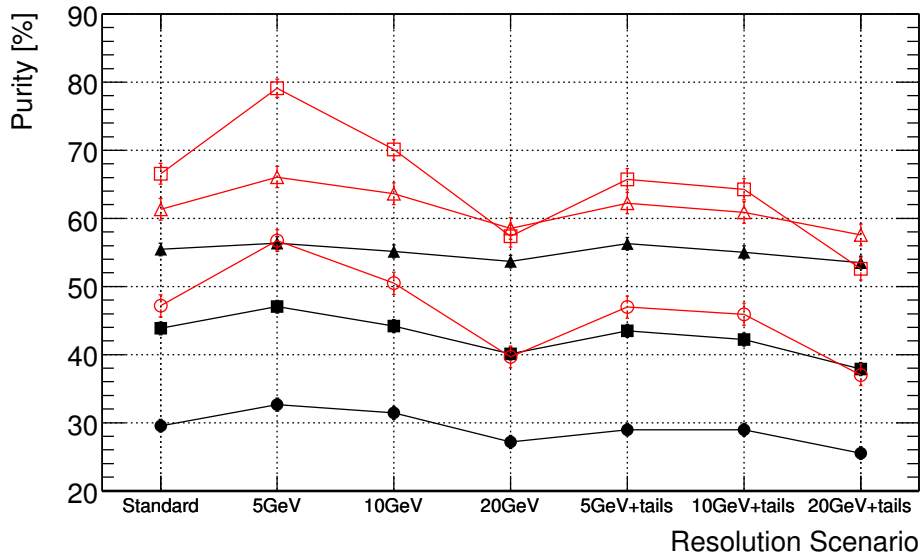
(c) Effect of the jet resolution on purity

Figure 4.38: (a,b) Jet resolution for various scenarios (cf. text) compared with the actual resolution from reconstructed jets. (c) Impact of the different scenarios on the Higgs boson purity (circles), the leptonic top purity (triangles) and the hadronic top purity (squares). The purity computed using all events is shown with solid markers while the purity using only events with perfect selection and *b*-tagging is represented with open markers.

Figure 4.39: Higgs boson purity as a function of the number of jets per event for all events (black solid lines) and for events with perfect preselection (red dashed lines).

4.13.3 Closer look at jet combinatorics

The Higgs boson purity as a function of the jet multiplicity is shown in figure 4.39 for the likelihood reconstruction. The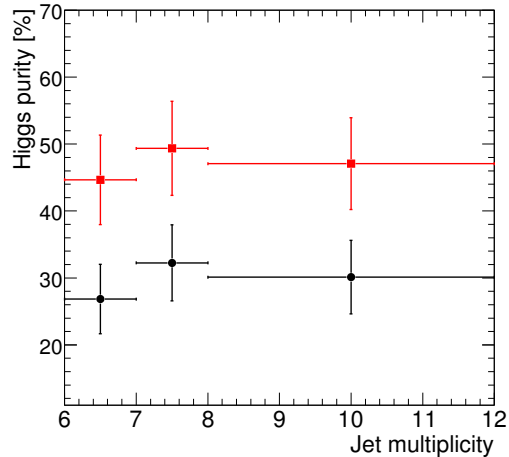 distribution looks flat, showing no significant effect of the extra radiation jets in the event on the Higgs purity. The same conclusion is made looking only at events with a perfect preselection.

To be able to quantify the relative importance of the different sources of wrong combinations, the true origin of the jets versus the assignment chosen by the likelihood is plotted in figure 4.40. One can clearly see that a large fraction of the *b*-jets originally from the Higgs boson decay are eventually used to reconstruct one of the top quarks: about 55% of the Higgs boson chosen candidates are built from one *b*-jet actually coming from the Higgs boson while the second *b*-jet is mostly coming from one of the top quarks. As seen before, a large number of jets used for the *W* boson reconstruction have no truth match and thus correspond to extra radiation jets in the event.

To decouple the jet combinatoric effect and the selection or *b*-tagging problems, we considered also only perfectly selected events as shown in figure 4.41. Since in this case all actual b-jets are properly tagged and there is no light/c-jet mistag, there is no exchange of *b*-jets with the *W* boson. In 10% of the cases, the likelihood is choosing an extra jet rather than one originated by a *W* boson to reconstruct the hadronic *W*. But the biggest problem lies in the combinatorics amongst *b*-jets. The exchange of *b*-jets between the top quarks and the Higgs boson leads to a Higgs purity of about 50% even with a perfect preselection. In the
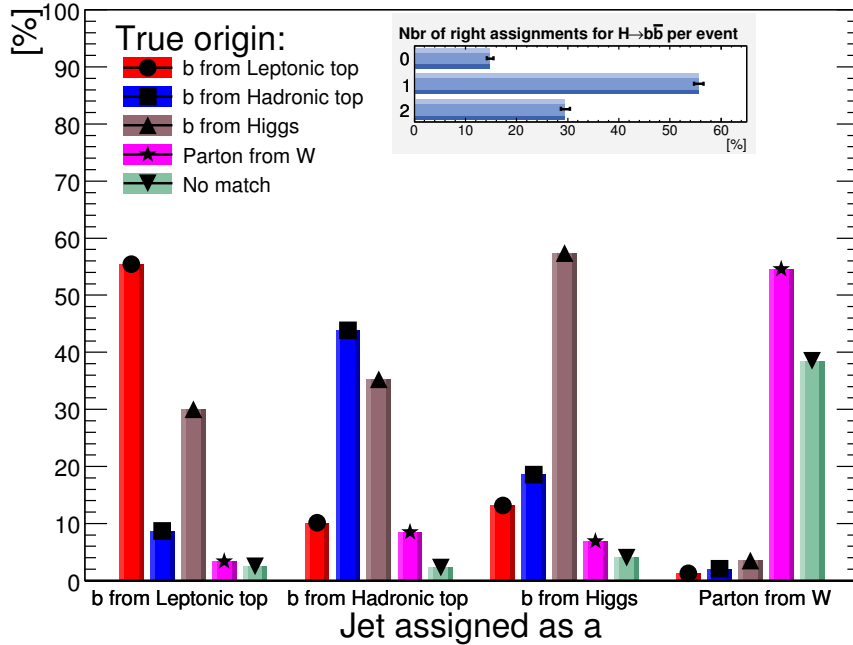
Figure 4.40: Truth origin for jets as assigned by the likelihood reconstruction method.

other half of the events, one of the *b*-jets from the Higgs is exchanged with one of the *b*-jets from the top quarks.

It is clear that a better preselection and better *b*-tagging performance as well as a better jet resolution can help to increase the purity. However, the major problem is the *b*-jet exchange between the Higgs and the top quarks. This is the case even when using powerful multivariate techniques such as the likelihood or the BDT.

4.14 Background extraction from data

Since no clear signal peak can be extracted on top of the background distribution, the background shape and normalisation should be known with very high precision to be able to extract the $t\bar{t}H(H \rightarrow b\bar{b})$ signal. A method to extract the background shape and normalisation from data is mandatory for this analysis. The method proposed in [1] is investigated in this section. This method relies on the hypothesis that the $m_{b\bar{b}}$ spectrum for background events does not change significantly for a loose and a tight *b*-tagging cut. With a loose cut, the signal is negligible and one can use this to extract the background shape. The shape is
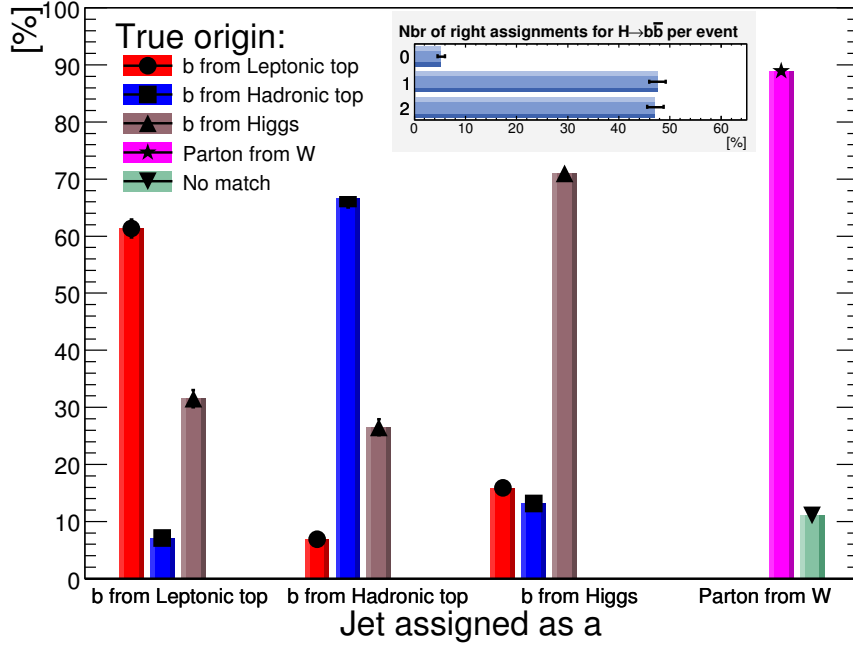
Figure 4.41: Truth origin for jets as assigned by the likelihood reconstruction method. Only event with a perfect preselection are kept.

then scaled to fit the distribution for a tight b-tagging cut. The normalisation is extracted away from the mass range where the signal is expected to be significant. Therefore one can compute the number of background events in this range with minimal signal contamination. This method was not previously completed due to the lack of Monte Carlo statistics for the $t\bar{t}$+jets sample. We will use the $t\bar{t}$+jets AF-II sample to check the feasibility of this method.

b-tagging cut	$t\bar{t}H$	$t\bar{t}b\bar{b}$	$t\bar{t}$+jets	Estimation error
$W_b>0$	2.1 ± 0.2 %	18.5 ± 0.5 %	79.4 ± 0.5 %	+19.9%
$W_b>1$	3.2 ± 0.3 %	26.6 ± 0.8 %	70.2 ± 0.8 %	+19.8%
$W_b>2$	4.7 ± 0.5 %	35.8 ± 1.1 %	59.6 ± 1.2 %	+17.1%
$W_b>3$	6.8 ± 0.7 %	45.1 ± 1.5 %	48.6 ± 1.5 %	+18.4%

Table 4.12: Fraction of events after the final mass range cut for different cuts on the b-tagging weight. The error on the estimated number of background events using the method described in this section is also given in the last column.

We consider the tight b-tagging cut used for the analysis ($W_b>6$), while different loose cuts are investigated. The analysis is performed for the $m_{b\bar{b}}$ spectrum

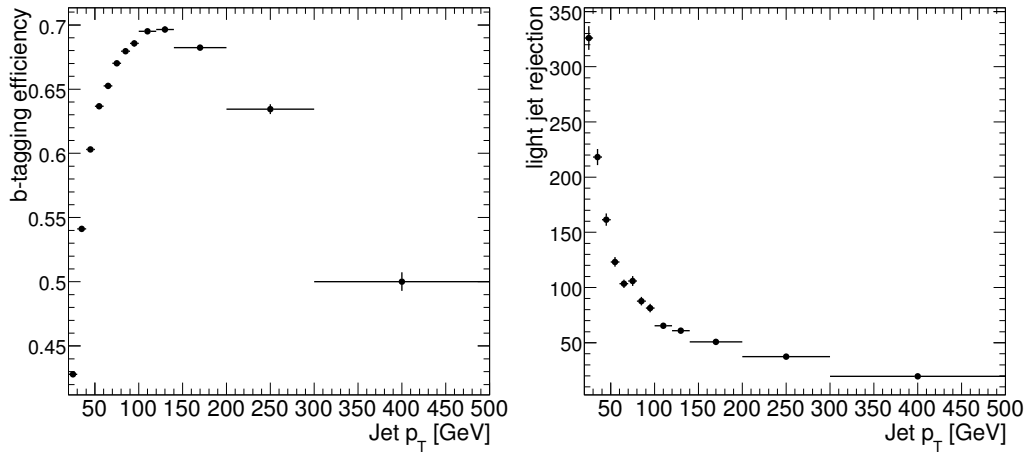Figure 4.42: *B*-tagging efficiency and light-jet rejection as a function of the jet p_T for $W_b > 6$ and for the $t\bar{t}$+jets sample.

obtained with the likelihood analysis. One should not that the choice of the reconstruction method does not have a significant impact on the final conclusion. The *b*-tagging efficiency and light-jet rejection both depend primarily and strongly of the jet p_T as shown in figures 4.42. As a consequence, tightening the *b*-tagging cut is biasing the $m_{b\bar{b}}$ distribution towards higher values for the $t\bar{t}$+jets background. This happens exactly in the signal region. This shift was not seen before with the fully simulated $t\bar{t}$+jets sample due to statistical fluctuations. Figure 4.43 represents the estimated background $m_{b\bar{b}}$ spectrum compared to the actual background and signal plus background $m_{b\bar{b}}$ spectra. The background shape was estimated using a loose *b*-tagging cut of $W_b > 2$ where the signal contamination is about 5% in the ± 30 GeV mass range. The shape was then normalised using the tails ($m_{b\bar{b}} < 60$ GeV and $m_{b\bar{b}} > 180$ GeV) of the $b\bar{b}$ mass spectrum with the tight *b*-tagging cut. Due to the shift of the peak of the $t\bar{t}$+jets $m_{b\bar{b}}$ spectrum, the extracted background mimics the signal plus background distribution and thus hide the $t\bar{t}H(H \rightarrow b\bar{b})$ signal.

The fraction of the signal and of both $t\bar{t}b\bar{b}$ and $t\bar{t}$+jets backgrounds are shown in table 4.12 for various loose *b*-tagging cut. The relative uncertainty on the number of the background events as extracted with this method, and in the mass range used to compute the significance, is also shown. This uncertainty is comparable to the overall systematic errors (without extracting the background from data) computed in the following section (4.15).

One could investigate the correction of the *b*-tagging bias for the $t\bar{t}$+jets shape using tagging rate functions. However, it is not clear if this can lead to significant decrease of the background uncertainties. With the present signal to background
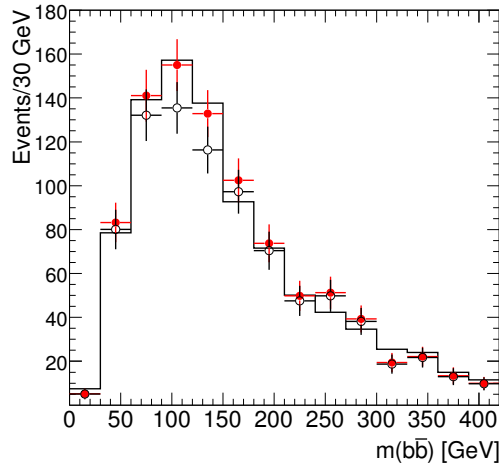
142

Figure 4.43: $m_{b\bar{b}}$ invariant mass distributions. The solid line histogram represents the background distribution obtained using a loose *b*-tagging cut of 2. The actual background distribution for the analysis (*i.e.* tight *b*-tagging cut of 6) is shown as open black symbols. The 'data-like' distribution (signal plus background) is shown with solid red markers. The extracted background spectrum seems more compatible with the signal plus background distribution than with the background only one. All distributions are normalised to 30 fb^{-1} .

ratio of 14%, an error of 7% or lower on the background is needed to achieve a systematic error comparable to the statistical one, leading to a significance of 2. If a significance of 5 were possible, this systematic uncertainty on the background extraction would have to be smaller than 3% (assuming the same S/B ratio).

4.15 Systematic errors

Since no reliable method to extract the background from data is currently available, one has to rely on the Monte Carlo to estimate this background. The cross-section of the $t\bar{t}$+jets and especially $t\bar{t}b\bar{b}$ backgrounds is subject to large theoretical errors, principally due to the scale choice (cf. 4.4). However it is expected that the $t\bar{t}$ cross-section will be known with an error of about 5% after a few fb^{-1} of data [1].

For a simple counting experiment, one should estimate the number of background events, in the considered mass range, with the different uncertainties due to the limited knowledge of the different resolutions and selection cut efficiencies. To be able to estimate these uncertainties, the analysis was redone while varying some parameters as listed in table 4.13. The resulting uncertainties on the signal

Source of uncertainty		Value	
Electron	energy scale	0.5%	
	resolution	$0.0073\times E_e$	
	efficiency	0.2%	
Muon	energy scale	1%	
	resolution	$\frac{0.011}{p_{T\,\mu}}\oplus 0.00017\ (GeV^{-1})$	
	efficiency	1%	
		$\mid\eta\mid<3.2$	$\mid\eta\mid>3.2$
Jet	energy scale	7%	15%
	resolution	$0.45\times\sqrt{E}(GeV^{\frac{1}{2}})$	$0.63\times\sqrt{E}(GeV^{\frac{1}{2}})$
b-tagging	efficiency	4%	
	light rejection	10%	

Table 4.13: The different parameters, and their corresponding variations, used to compute the systematic uncertainties. The variations correspond to the expected knowledge of the ATLAS detector performance with 100 pb^{-1} of data.

and background events are listed in table 4.14. The main uncertainties come from the b-tagging efficiency and the jet energy scale. The uncertainties concerning the leptons are negligible. The total uncertainty on the background sample is around 20% for the cut-based and the likelihood analysis and around 14% for the BDT analysis. Note that these uncertainties are subject to statistical fluctuations up to a relative value of 20% due to the limited number of generated events.

4.15.1 Final significance estimate

The systematic uncertainties are combined with the statistical errors and the resulting significance is given by:

$$Significance = \frac{S}{\sqrt{B+(\Delta B)^2}}$$

where ΔB represents the systematic uncertainties on the background samples. The significance as function of ΔB is represented in figure 4.44. The significance drops to 0.6 for the cut-based analysis, to 0.7 for the likelihood analysis and to 0.9 for the BDT analysis. A signal extraction using a simple counting method is impossible with these large systematic uncertainties.

Source of uncertainty		Cut-based		Likelihood		BDT	
		S(%)	B(%)	S(%)	B(%)	S(%)	B(%)
Electron	energy scale	±0.4	±1.3	±0.5	±0.5	±0.1	±0.1
	resolution	±0.2	±1.2	±0.1	±0.7	±0.1	±0.4
	efficiency	±0.2	±0.1	±0.2	± 0.	±0.1	±0.2
Muon	energy scale	±0.5	±1.3	±0.2	±1	±0.3	±0.6
	resolution	±0.4	±0.8	±0.3	±0.1	±0.1	±0.6
	efficiency	±0.4	±0.1	±1	±0.4	±0.8	±0.4
Jet	energy scale	±10	±10	±11	±12	±16	±4.5
	resolution	±3.8	±1.8	±3.5	±6	±4.2	±6.5
b-tagging	efficiency	±17	±18	±16	±14	±16	±11
	light rejection	±2.5	±3.3	±0.4	±3.3	±0.4	±2.7
Total (in quadrature)		±20	±21	±20	±20	±23	±14

Table 4.14: Relative effect of the various systematic uncertainties on the signal and background efficiencies.

4.16   Conclusion

The Higgs mechanism is presumably the one responsible of the electroweak symmetry breaking and the generation of masses for bosons and fermions in the Standard Model. The electroweak data gathered mostly at the LEP and the Tevatron point towards a light Higgs boson scenario. This scenario is the most difficult for the Higgs boson discovery at the LHC. Several channels will have to be combined for a discovery of a Higgs boson with $m_H <$130 GeV with a few tens of inverse femtobarns. In this mass range, the $t\bar{t}H(H \rightarrow b\bar{b})$ channel could be one of the interesting channels to discover a light SM Higgs boson with about 30 fb^{-1} of data at the LHC. This channel is also important to measure the Yukawa coupling of the third quark family.

   A detailed analysis with a full simulation of the ATLAS detector was presented in this chapter. NLO cross-sections were used after the recent calculation of the K-factor for the $t\bar{t}b\bar{b}$ process, the main background for the $t\bar{t}H(H \rightarrow b\bar{b})$ channel. A significance around 2 was found using three different reconstruction methods: cut-based, likelihood and boosted decision-tree methods. All methods suffer from a very low purity of the Higgs boson reconstruction. This is mainly due to the exchange of b-jets between a top quark and the Higgs boson. In the absence of a reliable method to extract the background from data, the systematic uncertainty on the number of background events is around 15%-20% while the signal to background ratio is about 14%. This is leading to a significance less than 1 after including the systematic uncertainties.
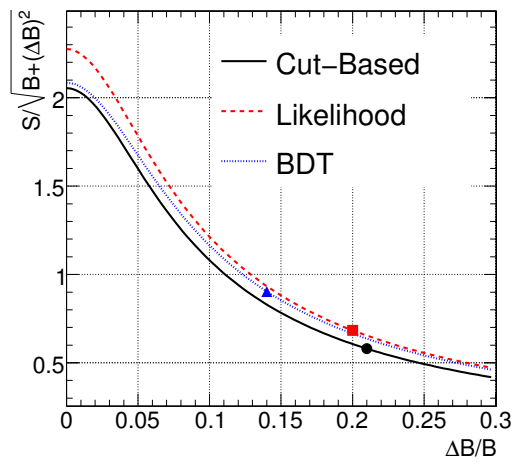
Figure 4.44: Significance as a function of the systematic uncertainties on the number of background events.

Conclusion

The first proton-proton collisions in the LHC will occur in a few months. A first commissioning period of the ATLAS detector with cosmic rays took place during the fall of 2008. Further cosmic muon data are being accumulated this year and currently the detector commissioning is well-advanced.

As part of the commissioning work of the ATLAS pixel detector, we discussed in this thesis two studies concerning some of the most important properties of the pixel detector: the low-noise occupancy and the high-detection efficiency. We found that a noise occupancy of 10^{-10} hit per pixel per bunch crossing can be achieved after masking 0.2‰, at most, of the channels. We also found that, for a stable detector operation, the noise occupancy fluctuations are limited and therefore a noise mask once determined is valid for a few weeks.

A detailed study of the pixel efficiency, using cosmic ray tracks, was also presented. The overall efficiency to have a pixel cluster on a track fulfilling the usual requirements for physics analysis was found to be 99.86% ± 0.01. Inefficiencies in the tracking algorithm for cluster-track association is the main source for the inefficiency. An intrinsic cluster detection efficiency of 99.993% $\pm$ 0.003 (stat.) $^{+0.000}_{-0.001}$ (syst.) was measured, after excluding about 4.2% of the channels which had problems during the 2008 commissioning period. Some of these channels are now recovered and currently about 98% of the pixel detector can be operated. An overview of the technical work concerning pixel calibrations and slow-control databases was also reported.

We investigated the observability of a light Higgs boson in the $t\bar{t}H(H \to b\bar{b})$ channel with 30 fb^{-1} of data. This channel presented a good potential in the first studies done with ATLAS. We presented in this thesis an updated study of the $t\bar{t}H$ channel using for the first time NLO cross-sections that were recently computed for the $t\bar{t}b\bar{b}$ process. This analysis also used a matrix-element generator for the $t\bar{t}b\bar{b}$ sample which represents the main background for the $t\bar{t}H(H \to b\bar{b})$ channel. For all samples, we used a full simulation of the ATLAS detector with realistic performance also including a trigger simulation. We find a statistical significance around 2 using three different techniques to reconstruct the Higgs

bosons. Multivariate techniques, as the likelihood technique and the use of a boosted decision-tree, slightly increase the signal reconstruction purity. However, none of these techniques is powerful enough to be able to efficiently solve the combinatorics of the four b-jets present in the event.

With no reliable method to extract the background from data so far, the systematic uncertainties are around 20% while the signal to background ratio is about 14%. The channel is not feasible with these large systematics uncertainties. Better methods to reconstruct the $t\bar{t}H$ signal and also to extract the background from data, in order to reduce the systematic uncertainties, are mandatory for this channel. For the reasons listed above, the $t\bar{t}H$ channel was removed from the combined ATLAS significance for a Higgs boson discovery with 10fb^{-1}. Other channels, like the $\gamma\gamma$ channel and the VBF channel, exhibit a higher potential to discover a light Higgs boson [1], though it is not easy either with these channels. Nevertheless, the $t\bar{t}H$ channel is still interesting for studying the couplings of the Higgs boson with the third family of quarks, which is important for the understanding of the Standard Model. Much more LHC data are required to perform those coupling studies.

Conclusion

Les premières collisions proton-proton au LHC vont arriver dans quelques mois. En automne 2008, une première période de mise en service du détecteur ATLAS avec des muons cosmiques a été effectuée. Actuellement, une nouvelle période de prise de données cosmiques est en cours.

Dans le cadre de la mise en marche du détecteur à pixels d'ATLAS, nous avons présenté dans cette thèse deux études portant sur deux des plus importantes propriétés du détecteur à pixels : le faible bruit et la grande efficacité de détection. Nous avons trouvé un niveau d'occupation du bruit de 10^{-10} coups par pixel par 25 ns après avoir masqué moins de 0.2‰o des canaux qui correspondent à des pixels bruyants. Nous avons trouvé aussi que les fluctuations du bruit sont faibles et les masques de pixels bruyants sont valides pendant quelques semaines pour une opération stable du détecteur à pixels.

Nous avons aussi présenté une étude détaillée de l'efficacité de détection des pixels menée avec les muons cosmiques. L'efficacité globale d'avoir un amas de pixels rattaché à une trace est de 99.86% ±0.01. Cette efficacité est obtenue pour un lot de traces avec des coupures de sélection motivées par celles habituellement utilisées dans les différentes analyses de physique. L'inefficacité provient principalement de la mauvaise association des amas de pixels aux traces reconstruites. L'efficacité intrinsèque des pixels a été également mesurée, sa valeur étant de 99.993% $\pm$ 0.003 (stat.) $^{+0.000}_{-0.001}$ (syst.). Les canaux présentant des problèmes, qui représentent 4.2% du détecteur, ont été exclus. Une partie de ces canaux a été réparée et actuellement 98% des canaux sont opperationnels. Un aperçu du travail technique, concernant les calibrations et les bases de données de contrôle du détecteur à pixels, mené pendant cette thèse a également été décrit.

Nous avons étudié le potentiel de découverte d'un boson de Higgs de faible masse dans le canal $t\bar{t}H(H \to b\bar{b})$ avec 30 fb^{-1} de données. Ce canal était prometteur dans les premières études menées avec ATLAS. Cette thèse présente une nouvelle analyse en utilisant pour la première fois les sections efficaces à l'ordre NLO qui ont été calculées récemment pour le processus $t\bar{t}b\bar{b}$. L'analyse utilise un générateur utilisant les éléments de matrice pour le bruit $t\bar{t}b\bar{b}$ qui est le bruit prin-

cipal pour le canal $t\bar{t}H(H \rightarrow b\bar{b})$. Une simulation détaillée du détecteur ATLAS, incluant une simulation du système de déclenchement, est utilisée pour tous les processus. Nous trouvons une significance statistique de 2 en utilisant 3 différentes techniques pour reconstruire le boson de Higgs. Des techniques avancées, comme les fonctions de vraisemblance et le "boosted decision tree" améliorent légèrement la pureté de reconstruction du signal. Cependant ces techniques ne sont pas assez puissantes pour résoudre, avec une grande pureté, la combinatoire des quatre jets b présents dans l'événement.

Les erreurs systématiques ont été evaluées à 20% en l'absence de méthode fiable pour extraire le bruit de fond des données, la fraction signal sur bruit étant de 14%. Une découverte du Higgs dans le canal $t\bar{t}H(H \rightarrow b\bar{b})$ est impossible à cause de cette large erreur systématique. Des méthodes plus puissantes pour la reconstruction du signal, ainsi que pour réduire les erreurs systématiques et extraire le bruit de fond des données sont indispensables pour ce canal. Pour ces raisons le canal $t\bar{t}H(H \rightarrow b\bar{b})$ n'est plus considéré comme un canal de découverte dans la combinaison de canaux faite par ATLAS pour 10fb^{-1} . Les autres canaux comme $\gamma\gamma$ et VBF présentent un potentiel plus élevé pour une découverte d'un boson de Higgs de faible masse [1]. Toutefois la découverte du boson de Higgs de faible masse reste toujours difficile au LHC. Néanmoins le canal $t\bar{t}H(H \rightarrow b\bar{b})$ reste intéressant pour l'étude du couplage de Yukawa des quarks de troisième génération, qui est une étude importante pour le Modèle Standard. Cette étude nécessite une plus grande quantité de données LHC.

Bibliography

[1] ATLAS, G. Aad *et al.*, Expected Performance of the ATLAS Experiment - Detector, Trigger and Physics, (2009), 0901.0512.

[2] P. A. M. Dirac, The Quantum theory of electron, Proc. Roy. Soc. Lond. **A117**, 610 (1928).

[3] E. Fermi, Trends to a Theory of beta Radiation, Nuovo Cim. **11**, 1 (1934).

[4] D. J. Gross and F. Wilczek, Ultraviolet behavior of non-abelian gauge theories, Phys. Rev. Lett. **30**, 1343 (1973).

[5] D. J. Gross and F. Wilczek, Asymptotically Free Gauge Theories. 1, Phys. Rev. **D8**, 3633 (1973).

[6] H. D. Politzer, Reliable perturbative results for strong interactions?, Phys. Rev. Lett. **30**, 1346 (1973).

[7] M. Gell-Mann, A Schematic Model of Baryons and Mesons, Phys. Lett. **8**, 214 (1964).

[8] G. Zweig, An SU(3) model for strong interaction symmetry and its breaking, CERN-TH-401.

[9] M. Y. Han and Y. Nambu, Three-triplet model with double SU(3) symmetry, Phys. Rev. **139**, B1006 (1965).

[10] S. L. Glashow, Partial Symmetries of Weak Interactions, Nucl. Phys. **22**, 579 (1961).

[11] S. Weinberg, A Model of Leptons, Phys. Rev. Lett. **19**, 1264 (1967).

[12] A. Salam, Elementary Particle Theory, (1969).

[13] K. G. Wilson, Confinement of Quarks, Phys. Rev. **D10**, 2445 (1974).

[14] P. W. Higgs, Broken Symmetries and the Masses of Gauge Bosons, Phys. Rev. Lett. **13**, 508 (1964).

[15] F. Englert and R. Brout, Broken Symmetry and the Mass of Gauge Vector Mesons, Phys. Rev. Lett. **13**, 321 (1964).

[16] G. S. Guralnik, C. R. Hagen, and T. W. B. Kibble, Global Conservation Laws and Massless Particles, Phys. Rev. Lett. **13**, 585 (1964).

[17] J. Goldstone, A. Salam, and S. Weinberg, Broken Symmetries, Phys. Rev. **127**, 965 (1962).

[18] N. Cabibbo, Unitary Symmetry and Leptonic Decays, Phys. Rev. Lett. **10**, 531 (1963).

[19] M. Kobayashi and T. Maskawa, CP Violation in the Renormalizable Theory of Weak Interaction, Prog. Theor. Phys. **49**, 652 (1973).

[20] B. Pontecorvo, Neutrino experiments and the question of leptonic-charge conservation, Sov. Phys. JETP **26**, 984 (1968).

[21] Z. Maki, M. Nakagawa, and S. Sakata, Remarks on the unified model of elementary particles, Prog. Theor. Phys. **28**, 870 (1962).

[22] J. F. Gunion, H. E. Haber, G. L. Kane, and S. Dawson, THE HIGGS HUNTER'S GUIDE, SCIPP-89/13.

[23] N. Cabibbo, L. Maiani, G. Parisi, and R. Petronzio, Bounds on the Fermions and Higgs Boson Masses in Grand Unified Theories, Nucl. Phys. **B158**, 295 (1979).

[24] T. Hambye and K. Riesselmann, Matching conditions and Higgs mass upper bounds revisited, Phys. Rev. **D55**, 7255 (1997), hep-ph/9610272.

[25] J. Kuti, L. Lin, and Y. Shen, Upper Bound on the Higgs Mass in the Standard Model, Phys. Rev. Lett. **61**, 678 (1988).

[26] ALEPH, A. Heister *et al.*, Final results of the searches for neutral Higgs bosons in e+ e- collisions at $\sqrt{s}$ up to 209 GeV, Phys. Lett. **B526**, 191 (2002), hep-ex/0201014.

[27] LEP Working Group for Higgs boson searches, R. Barate *et al.*, Search for the standard model Higgs boson at LEP, Phys. Lett. **B565**, 61 (2003), hep-ex/0306033.

[28] CDF and D0 Collaborations, Combined CDF and DZero Upper Limits on Standard Model Higgs-Boson Production with up to 4.2 fb-1 of Data, Rencontres de Moriond EW 2009 (2009), arXiv:0903.4001.

[29] LEP ElectroWeak Working Group, Results March 16 2009, http://lepewwg.web.cern.ch/LEPEWWG/.

[30] ALEPH Collaboration and CDF Collaboration and D0 Collaboration and DELPHI Collaboration and L3 Collaboration and OPAL Collaboration and SLD Collaboration and LEP Electroweak Working Group and Tevatron Electroweak Working Group and SLD Electroweak Working Group and Heavy Flavour Group, Precision Electroweak Measurements and Constraints on the Standard Model, (2008), 0811.4682.

[31] e. . Evans, Lyndon and e. . Bryant, Philip, LHC Machine, JINST **3**, S08001 (2008).

[32] ATLAS, G. Aad *et al.*, The ATLAS Experiment at the CERN Large Hadron Collider, JINST **3**, S08003 (2008).

[33] The ATLAS Pixel collaboration, The ATLAS pixel detector mechanics and services, To appear.

[34] G. Aad *et al.*, ATLAS pixel detector electronics and sensors, JINST **3**, P07007 (2008).

[35] J. Cook, Conditions Database for PVSS, Installation and Users Guide, https://edms.cern.ch/file/684959/1.8/PVSS-COOL.pdf.

[36] LCG Conditions Database Project, http://lcgapp.cern.ch/project/CondDB/.

[37] R. Hawkings, ATLAS conditions database user guide, http://atlas.web.cern.ch/Atlas/GROUPS/DATABASE/project/online/doc.

[38] T. Lari, Lorentz angle variation with electric field for ATLAS silicon detectors, (2001), ATL-INDET-2001-004.

[39] Atlas public results concerning the analysis of the cosmic rays data, https://twiki.cern.ch/twiki/bin/view/Atlas/ApprovedPlotsID, To appear in an ATLAS public note.

[40] Particle Data Group, C. Amsler *et al.*, Review of particle physics, Phys. Lett. **B667**, 1 (2008).

[41] J. M. Butterworth *et al.*, ATLAS Sensitivity to the Standard Model Higgs in the HW and HZ Channels at High Transverse Momenta, ATL-COM-PHYS-2009-345.

[42] E. Richter-Was and M. Sapinski, Search for the SM and MSSM Higgs boson in the $t\bar{t}H$, $H \rightarrow b\bar{b}$ channel, ATL-PHYS-98-132.

[43] A. Bredenstein, A. Denner, S. Dittmaier, and S. Pozzorini, NLO QCD corrections to top anti-top bottom anti-bottom production at the LHC: 1. quark-antiquark annihilation, JHEP **08**, 108 (2008), 0807.1248.

[44] A. Bredenstein, A. Denner, S. Dittmaier, and S. Pozzorini, NLO QCD corrections to pp -¿ t anti-t b anti-b + X at the LHC, (2009), 0905.0110.

[45] T. Sjostrand *et al.*, High-energy-physics event generation with PYTHIA 6.1, Comput. Phys. Commun. **135**, 238 (2001), hep-ph/0010017.

[46] M. Spira, HIGLU: A Program for the Calculation of the Total Higgs Production Cross Section at Hadron Colliders via Gluon Fusion including QCD Corrections, (1995), hep-ph/9510347.

[47] S. Dawson, C. Jackson, L. H. Orr, L. Reina, and D. Wackeroth, Associated Higgs production with top quarks at the Large Hadron Collider: NLO QCD corrections, Phys. Rev. **D68**, 034022 (2003), hep-ph/0305087.

[48] W. Beenakker *et al.*, NLO QCD corrections to t anti-t H production in hadron collisions., Nucl. Phys. **B653**, 151 (2003), hep-ph/0211352.

[49] B. P. Kersevan and E. Richter-Was, The Monte Carlo event generator AcerMC version 1.0 with interfaces to PYTHIA 6.2 and HERWIG 6.3, Comput. Phys. Commun. **149**, 142 (2003), hep-ph/0201302,hep-ph/0405247.

[50] S. Frixione and B. R. Webber, The MC@NLO event generator, (2002), hep-ph/0207182.

[51] G. Marchesini *et al.*, HERWIG: A Monte Carlo event generator for simulating hadron emission reactions with interfering gluons. Version 5.1 - April 1991, Comput. Phys. Commun. **67**, 465 (1992).

[52] G. Corcella *et al.*, HERWIG 6.5: an event generator for Hadron Emission Reactions With Interfering Gluons (including supersymmetric processes), JHEP **01**, 010 (2001), hep-ph/0011363.

[53] J. M. Butterworth, J. R. Forshaw, and M. H. Seymour, Multiparton interactions in photoproduction at HERA, Z. Phys. **C72**, 637 (1996), hep-ph/9601371.

[54] R. Bonciani, S. Catani, M. L. Mangano, and P. Nason, NLL resummation of the heavy-quark hadroproduction cross- section, Nucl. Phys. **B529**, 424 (1998), hep-ph/9801375.

[55] A. Djouadi, J. Kalinowski, and M. Spira, HDECAY: A program for Higgs boson decays in the standard model and its supersymmetric extension, Comput. Phys. Commun. **108**, 56 (1998), hep-ph/9704448.

[56] ATLAS, ATLAS Detector and Physics Performance Technical Design Report, (1999), CERN/LHCC/99-14,CERN/LHCC/99-15.

[57] J. Cammin and M. Schumacher, The ATLAS discovery potential for the channel $t\bar{t}H$, $H \rightarrow b\bar{b}$, ATL-PHYS-2003-024.

[58] S. Corréard, Calibration de l'étiquetage des jets b et recherche du boson de Higgs dans le canal $t\bar{t}H$, $H \rightarrow b\bar{b}$ dans l'expérience ATLAS, Ph.D. thesis, Univ. Méditerranée Aix-Marseille II (2006), CPPM-T-2006-01.

[59] D. Benedetti *et al.*, Observability of Higgs produced with top quarks and decaying to bottom quarks, J. Phys. **G34**, N221 (2007).

[60] ATLAS and CMS, G. Aad and J. Steggemann, The t anti-t H analysis at the LHC, Nuovo Cim. **123B**, 1255 (2008).

[61] S. Hassani *et al.*, A muon identification and combined reconstruction procedure for the ATLAS detector at the LHC using the (MUONBOY, STACO, MuTag) reconstruction packages, Nucl. Instrum. Meth. **A572**, 77 (2007).

[62] E. Richter-Was, D. Froidevaux, and L. Poggioli, ATLFAST, a package for particle-level analysis, (1998), ATL-PHYS-98-131.

[63] A. Hocker *et al.*, TMVA: Toolkit for multivariate data analysis, PoS **ACAT**, 040 (2007), physics/0703039.

[64] L. Breiman, J. Friedman, R. Olshen, and C. Stone, *Classification and Regression Trees* (Wadsworth and Brooks, Monterey, CA, 1984).

Résumé

L'ajustement des différentes mesures électrofaibles dans le cadre du Modèle Standard privilégie un boson de Higgs de faible masse égale à $m_H = 90^{+36}_{-27}$ GeV, proche de la limite d'exclusion obtenue au LEP. La découverte du boson de Higgs à faible masse au LHC est difficile et nécessite la combinaison de plusieurs canaux. La production associée du boson de Higgs avec une paire de quarks top, le boson de Higgs se désintegrant en une paire de quarks b (dominants pour m_H <135 GeV), est l'une des signatures considérées. Ce canal permet d'accéder au couplage du Yukawa du top et du quark beau. Le potentiel de découverte du boson de Higgs dans ce canal est étudié avec l'expérience ATLAS. Plusieurs ingrédients sont cruciaux pour cette analyse: la reconstruction du système top anti-top avec une grande pureté, un excellent étiquetage des jets b et la connaissance du bruit de fond $t\bar{t}$+jets.

Le détecteur à pixels est le sous-détecteur le plus important d'ATLAS pour l'étiquetage des jets b. En automne 2008, le détecteur ATLAS a été mis en service et étudié avec des muons cosmiques. La détermination des canaux morts, des constantes de calibrations et la prise en compte des données de contrôle du détecteur à pixels sont détaillées pour cette periode. Une étude pour déterminer puis masquer les pixels bruyants est également présentée. Finalement, l'efficacité de détection des pixels a été mesurée avec les muons cosmiques.

Mots Clés: LHC, ATLAS, boson de Higgs, ttH, quark top, détecteur à pixels.

Abstract

English Title: Commissioning of the ATLAS pixel detector and search of the Higgs boson in the $t\bar{t}H$, $H \to b\bar{b}$ channel with the ATLAS experiment at the LHC.

The global fit of Higgs boson quantum contributions to the electroweak experimental observables, computed within the Standard Model, favors a light Higgs boson with a mass of $m_H = 90^{+36}_{-27}$ GeV, on the edge of the 95% Confidence Level region excluded by LEP. Finding a light Higgs boson at LHC is experimentally difficult and several channels with various signatures will be sought for. The associated production of the Higgs boson with a pair of top quarks, with the subsequent decay of the Higgs boson into b-quark pairs (dominant for m_H <135 GeV) , is one of the channels considered. This channel opens the possibility of measuring the top and b-quark Yukawa couplings. The potential of the ATLAS detector to observe this channel is described. Several ingredients are crucial: the reconstruction of the top-antitop system with a high-purity, excellent b-tagging capabilities and good knowledge of the $t\bar{t}$+jets background.

The pixel detector is the most important ATLAS sub-detectors for tagging b-jets. The ATLAS detector was commissioned with cosmic muon rays in autumn 2008. The pixel detector dead channels, calibration constants and slow control informations are described for this period. A detailed study about pixel noise determination and suppression is presented. Finally, the pixel detection efficiency is measured using cosmic muon rays.

Key Words: LHC, ATLAS, Higgs boson, ttH, top quark, pixel detector.